The Influence of Electric Field on the Ordering of Lipid Monolayer

and Lipid-Protein Binding

BY

HAO YU
B.S., University of Science and Technology of China, 2005
M.S., University of Illinois at Chicago, Chicago, 2008

THESIS

Submitted as partial fulfillment of the requirements
for the degree of Doctor of Philosophy in Physics
in the Graduate College of the
University of Illinois at Chicago, 2014

Chicago, Illinois

Defense Committee:

Mark Schlossman, Chair and Advisor

Anjum Ansari

Robert F. Klie

Ursula Perez-Salas

Petr Vanýsek, Northern Illinois University

To my wife, Jin Zhang, my parents,

my parents-in-law and my sister.

Without them, this thesis would never have been accomplished.

ACKNOWLEDGMENTS

In the beginning, I wish to express my sincere gratitude to my family for their support, patience and encouragement. They are always the most important part of my life.

I would like to thank Professor Mark Schlossman for his patient guidance, solid support, and enthusiastic encouragement throughout graduate school. He opened my eyes to the wonders of X-ray reflectivity. My grateful thanks are also extended to Professor Petr Vanysek. His valuable suggestions on electrochemical aspects of my experiment contributed a lot to the research results demonstrated in this thesis.

My research was done in collaboration with three great researchers – Shan Tao, Zenmei Ohkubo and Irena Yzeiri. Special thanks to Shan Tao from Professor Wonhwa Cho's group for coaching me on protein preparation step by step. I am indebted to my other two collaborators, Zenmei Ohkubo and Irena Yzeiri for their strong support on molecular dynamics simulation. The contributions from them complemented the experimental results and helped me understand them.

I acknowledge contributions from our collaborators at the ChemMatCARS sector of the Advanced Photon Source at Argonne National Laboratory, Drs. Binhua Lin and Mati Meron.

I wish to thank my colleagues and friends at UIC for close involvement in every step of the experiments, especially taking data at Argonne National Laboratory. Without their help, I would have never finished my projects on time. Their friendship is also one of the most important things to accompany me through graduate school. It is not possible to thank everyone who has helped me with all aspects of my life and work, but I assure you that my gratitude towards you is not any less than others who have been listed here.

CONTRIBUTION OF AUTHORS

In Chapter 1, I introduced the main focus of my research, the influence of the membrane potential on cell membranes, and the significance of my research on understanding the mechanism of some biological fuctions. Chapter 2 is the theoretical background of X-ray reflectivity, the technique that was used to study the microscale structure of the biological system. In Chapter3, I reviewed the techniques that were used in my research. This chapter also contains unpublished experiement and MD simulation results on the effects of external electrical potential on the ordering of lipid membrane. My work was critical to use the electrical chemistry and X-ray reflectivity methods to probe the lipid membrane under different potential difference; while Irena Yzeiri performed the MD simulation, and generated Figure 17, Figure 19 and Table 4. In Chapter 4, I also included a series of unpublished experiments on the influence of external electrical potential on the binding and rotation of protein, cPLA2α-C2, on the lipid membrane. My work was to carry out the electric chemistry measurements and X-ray reflectivity measurements on the protein bound to the lipid after Dr. Shan Tao provided cPLA2α-C2. Later, Dr. Zenmei Ohkubo performed the MD simulation on the characteristics of the protein bound to the lipid membrane and generated Figure 36. Two manuscripes are under preparation for which I will be the first author. In this thesis, I used some materials from my published paper, for which I was the third author. All these materials are "Reproduced (or 'Reproduced in part') with permission from [Hou, B.; Laanait, N.; Yu, H.; Bu, W.; Yoon, J.; Lin, B.; Meron, M.; Luo, G.; Vanysek, P.; Schlossman, M. L., Ion Distributions at the Water/1,2-Dichloroethane Interface: Potential of Mean Force Approach to Analyzing Xray Reflectivity and Interfacial Tension Measurements Journal of Physical Chemistry B 2013, 117, 5365] Copyright 2013 American Chemical Society."

TABLE OF CONTENTS

LIST OF TABLES

LIST OF FIGURES

LIST OF ABBREVIATIONS

TDATPBCl	Tetradodecylammonium Tetrakis(4-chlorophenyl)borate
DCE	1,2-dichloroethane
ITIES	Interface between Two Immiscible Electrolyte Solutions
CV	Cyclic Voltammogram
ZCP	Potential of Zero Charge
RE	Reference Electrode
R/R_f	X-ray Reflectivity Normalized to Fresnel Reflectivity
SOPC	1-stearoyl-2-oleoyl-sn-glycero-3-phosphocholine
CBL	Calcium binding loop
cPLA2α-C2	C2 domain of cytosolic phospholipase A2
EPR	Electron paramagnetic resonance
NMR	Nuclear magnetic resonance
MD	Molecular Dynamics
XR	X-ray Reflectivity

SUMMARY

This thesis is devoted to studies of the influence of an externally controlled electric potential difference on Gibbs monolayers of 1-stearoyl-2-oleoyl-sn-glycero-3-phosphocholine (SOPC), as well as its influence on the binding of the C2 domain of cytosolic phospholipase-A2 (cPLA2α-C2) protein to the SOPC monolayer. X-ray reflectivity, molecular dynamics (MD) simulations and electrochemical methods are used to gather microscopic and macroscopic information about the ordering, orientation, and binding configuration of the molecules on the electric potential difference or membrane potential.

Gibbs monolayers of SOPC assemble at the interface between a bulk aqueous electrolyte solution and a bulk organic electrolyte solution with 1,2-dichloroethane (DCE) as the solvent. The interfacial area per lipid for different values of electric potential difference between the aqueous and organic phases is determined from interfacial tension measurements. The area per lipid increases when the electric potential difference is greater than 0.18 V. Cyclic voltammetry confirms the result and provides evidence that the interfacial behavior of SOPC monolayers is reversible. X-ray reflectivity measurements are analyzed to determine the interfacial electron density profile, including the thicknesses of the phosphocholine (PC) head group region and the SOPC hydrocarbon chain regions of the monolayer. An increase of electron density in the layer of hydrocarbon chains with increasing electric potential difference is consistent with the penetration of DCE molecules into the hydrocarbon layer, as a result of the increase of area per lipid. The projected total length of SOPC molecules decreases with increasing electric potential difference, where the length is projected onto the direction of the electric field (*i.e.*, the z direction perpendicular to the interface). MD simulations at fixed area per lipid show small differences in the rotation of SOPC molecules when the imposed electric field is varied. This indicates that the primary effect in the experiments is due to the changing area per lipid as a function of electric potential difference, and the subsequent re-orientation of the lipid to accommodate the change in interfacial density.

The analysis of X-ray reflectivity on cPLA2α-C2 domains bound to the SOPC monolayer on the water|DCE interface provides information on the angular orientation and penetration depth of the domains under external electric field. The best-fit orientations for the X-ray reflectivity curves for potential difference $\Delta\phi^{w-o}=$-0.07 V, 0.03 V, 0.13V, 0.18V are very similar. The best-fit configuration at an electric potential difference of 0.03

V is given by orientation angles $\theta = 84°, \varphi = 70°$, and a penetration of 11.5 ± 1.7 Å. Under this orientation, the calcium binding loop CBL3 penetrates into the hydrocarbon chains of the SOPC monolayer, and the hydrophobic interaction between the chains and the hydrophobic residues is believed to be important for binding. In addition, the Ca^{2+} ions on the CBLs are located within 1 Å of the lipid phosphate group, which provides a favorable electrostatic attraction between cPLA2α-C2 and lipids. This configuration generally agrees with MD simulations and EPR measurements carried out by other groups.

Under low electric potential differences (-0.07 V to 0.18 V), the electron density profile shows an increase of electron density in the lipid tail group region after protein binding. This increase is due to both protein and DCE penetration into this region. When the electric potential difference is increased to 0.38 V, the reflectivity curves change significantly. Our study of SOPC monolayers shows that the lipid density will decrease at these high potentials, thus reducing the number of binding sites for proteins. It is also likely that the highly negative charged (-7.6 at pH=7) cPLA2α-C2 domains are removed from the interface by the large positive electric potential difference. Future research is required to distinguish between these two possibilities.

Chapter 1

INTRODUCTION

1.1   Biological Membranes

1.1.1   Cellular membranes

The membrane is an important part of the cell, and most cellular membranes have the same basic phospholipid bilayer structure. The basic function of the membranes is to act as a selective barrier that encloses the cell to prevent the random mixing of the contents of one cell with those of another and the outer environment. Besides lipids, the cellular membrane is very complex. It contains many other components, including proteins, enzymes, cholesterol, though lipids and proteins are the two major components of all biological membranes on earth. The ratio of lipids to proteins varies dramatically in different membranes, and the types of lipids and proteins are also quite different. Different membrane components provide the cell with different biological functions.

1.1.2   Introduction to Membrane Lipids

Four major lipid classes are found in the membranes of most eukaryotic organisms: glycerophospholipids, glyceroglycolipids, sphingolipids, and sterols. Phospholipids formed the largest group among these lipid classes. For mammalian membranes, more than 40% of the mess is phospholipids; while up to 40% by mass for plant membranes. There are two major groups of phospholipids are found in eukaryotic cell membranes, which constitute more than 80% of the total membrane phospholipids. One of the major groups is choline phospholipids (phosphatidylcholine, PC). Choline phospholipid is essential to maintain critical signal transduction cascades,[1] cell shape,[2] hemostasis,[3] and homeostasis.[4]

PC is composed of a head group containing choline, phosphate, and glycerol , as well as, typically, two fatty acyl chains to form the tail group. The lipid is referred to as saturated or unsaturated if the chains are, respectively, saturated (such as DSPC or DPPC) or unsaturated (SOPC, DOPC). PC is charge neutral, but it

carries an electric dipole moment of about 10 D, which is generated by the charged NH_4^+ and PO_4^- moieties in the head group.[5]

PCs are amphiphiles, they have a polar head group and an apolar tail group. This feature allows them to form micelles, bilayers or even monolayers at the water|oil interface. A micelle is an aggregate of amphiphiles whose hydrophobic tail groups form a hydrophobic core while the polar head groups form an external surface that interacts with the aqueous medium. PC monolayers can be formed at water|oil interfaces with hydrophobic tail groups in the oil phase and hydrophilic head groups in the water. The most common form of PC aggregation is the bilayer, which contains two back-to-back monolayers. The head groups of the PCs are in contact with the surrounding water, while the tail groups are enclosed between the two head group layers. PC head groups play a critical role in many biological activities, and their dipole moment can respond to the change in membrane potential, *i.e.*, the electric potential difference across the bilayer, and change the membrane ordering dramatically.[6,7] The hydrocarbon membrane core is also essential for many biological functions. It provides a very good solvent for the hydrophobic parts of proteins, which contributes to the assembly of integral membrane proteins. It enables the anchoring of peripheral membrane proteins through both hydrophobic and hydrophilic effects.

1.1.3   Introduction to Membrane Proteins

Protein molecules, including membrane proteins, are linear heteropolymers containing 20 different amino acids[8] linked end-to-end by peptide bonds. The complex 3-dimensional protein structure is described hierarchically. The primary structure refers to the amino acid sequence of the linear polymer. Local secondary structures, such as α helices or β strands, are formed by specific regions of the sequence.[9] The 3-dimensional packing of secondary structural elements into one or several compact globular units called domains is referred to as the tertiary structure. Additionally, a quaternary structure can be present in a protein that consists of several polypeptide chains. Formation of tertiary or quaternary structures can position amino acids, which may be far apart in the sequence, close together to form a functional region, referred to as an active site.

Membrane proteins are attached to or associated with the membrane of a cell. They perform a variety of important functions, including ion transportation across the membrane, protein trafficking, protein synthesis, etc.

They are divided into two groups: peripheral membrane proteins which interact with only one side or leaflet of the membrane and integral membrane proteins which are permanently attached to the membrane and typically span both leaflets of the membrane, though some integral membrane proteins are attached to the membrane from only one side, with one end of the protein protruding either inside or outside the cell. This thesis is concerned only with peripheral membrane proteins and integral membrane proteins will not be discussed further.

Peripheral membrane proteins adhere temporarily to the cell membrane or integral membrane protein. Most peripheral membrane proteins attach reversibly to cell membranes, which make them suitable for cell signaling or many other important cellular events[10]. There are many kinds of peripheral membranes, though there is a much smaller class of binding domains that act to bind a multi-domain protein to the cell membrane. The C2 binding domain is an important family of domains that is found in many different peripheral membrane proteins.[11] Many binding mechanisms have been proposed. One mechanism involves the electrostatic interaction of a charged protein domain with membranes containing acidic lipids with negatively charged head groups. Murray et al.[11] used finite-difference Poisson-Boltzmann calculations to demonstrate the importance of electrostatic interactions between C2 domains and phospholipids membranes. Chiu-hao Chen et al.[12] used X-ray reflectivity to determine the binding configuration of PKCα-C2 to mixed SOPC/SOPS Langmuir monolayers. The binding configuration describes the placement and orientation of the binding domain against a lipid monolayer. Indirect information about the role of electrostatic forces or other interactions can then be determined. Another binding mechanism consists of hydrophobic interactions between hydrophobic residues of the protein and the hydrocarbon chains of the lipid layers. For instance, biochemical studies have suggested that the binding of cPLA2α-C2 to zwitterionic phospholipids is primarily hydrophobic[13] and calculations by Murray et al.[11] demonstrated that electrostatic interactions alone were not enough to bind cPLA2α-C2 to model membranes. However, X-ray reflectivity studies by Malkova et al.[14] demonstrated that several effects contribute to the binding of cPLA2α-C2 to SOPC. These included both electrostatic and hydrophobic interactions, as well as entropic effects due to the release of lipid-hydrating water molecules upon protein binding.

1.1.4   Membrane Potential

Membrane potential is the electric potential difference between the interior and the exterior of a biological cell. It is a result of ion concentration gradients inside and outside the cell, as well as charges on the membrane. The cell membrane acts as a barrier to the movement of ions, though passage of ions through ion channels in the membrane can modify the membrane potential.

Membrane potential plays a very crucial role in many biological functions. For example, the electric potential difference can drive molecular membrane processes, including reversible binding of peripheral membrane proteins to the cell membrane. The membrane potential can also transmit signals within electrically excitable cells such as neurons and muscle cells. Potassium ion channel has been reported to response to local changes in membrane potential to open or close the ion channels and lead to modifications in ion concentration and membrane potential in more distant regions of the cell. Malfunction of potassium channels can cause the instability of membrane potential and disturb the ion distribution across the cell membrane, which can cause arrhythmias.

Electrochemical methods[15-17] have been developed to apply controlled electric potential differences across phospholipid monolayers self-assembled at the interface between two immiscible electrolyte solutions (ITIES). The external electric potential difference plays the same role as the membrane potential, thus one can study the stability of a lipid monolayer at an electrified ITIES, as well as the influence of membrane potential on protein membrane binding.

1.2   Organic Molecular Monolayers

Monolayers formed by surfactants at the interface between two immiscible phases have been noticed, utilized but little understood until the theory behind it was discovered. In 1774, Benjamin Franklin described his famous scientific experiments on the effect of oily films on water in his paper.[18] Young and Laplace clarified the capillary and surface tension effects in 1878. Finally, in 1917, Irving Langmuir developed experimental and theoretical concepts of the behavior of organic molecules in monolayers insoluble in their subphase. Later, Gibbs published his analysis of adsorption and surface tension effects,[19] which theoretically described the relationship between macroscopic characteristics of the monolayer and interfacial tension.

Based on properties of the surfactant, organic monolayers can be divided into two classes: Langmuir monolayers and Gibbs monolayers. The term Langmuir monolayer refers to monolayers consisting of surfactants that are insoluble in the bulk phases on either side of the interface. The term Gibbs monolayer refers to monolayers formed by surfactant soluble in both bulk phases. Monolayers can be formed on liquid-liquid, liquid-air, and liquid-solid interfaces. In this thesis, we studied self assembled Gibbs monolayers consisting of SOPC lipids on the liquid-liquid interface.

The liquid-liquid interface is attracting more attention nowadays. Blank and Feig mentioned that an interface between two immiscible liquids (ITIES) could be used as a good model for half of a biological membrane,[20] because it is a dynamic structure, and the ion distribution at the interface can be controlled. Compared with the liquid-air monolayer, one of the biggest advantages of liquid-liquid monolayer is that it is more convenient for electrochemical experiments. It has been shown that experimental electrochemistry on two immiscible liquids is successful and practical.[21]

Electrical phenomena at the surface of lipid membranes are fundamental to understand the mechanism of membrane transport of ions and molecules.[22] The use of polarized ITIES is probably one of the best ways to study the properties of adsorption of lipid layers, the binding between lipid and protein, and penetration of enzyme into lipid monolayer under the control of the potential across a lipid layer. The first studies of soluble phospholipid (lecithin) adsorption at electrified liquid-liquid interface were presented by Watanabe et al.[23,24] These authors measured electrocapillary curves for the electrified interface formed between methylisobutylketone and water and characterized the adsorption of phospholipids. They probed the interaction between lipids and cations in the aqueous phase, as well as the effect of pH on the electrocapillary curves. Subsequently, Girault and Schiffrin[16] and Kakiuchi,[25] introduced the study of lipid monolayers at the polarized liquid-liquid interface. Marecek and co-authors proposed a reaction mechanism to explain desorption of zwitterionic lecithin lipids from polarized liquid-liquid interfaces at high electric potential differences when the aqueous medium is acidic.[15] Briefly, the lecithin headgroups are charged by protonation at positive potentials and, subsequently re-dissolved into the organic phase.

In this thesis, a membrane potential is simulated by applying an externally controlled electric potential difference across a lipid monolayer. This allows us to carry out X-ray reflectivity and electrochemical studies

under certain potential differences. The micro scale information of the lipid ordering and protein-lipid binding can be extracted from the X-ray data. This research provides insight into the role of the membrane potential in biological systems.

Chapter 2

THEORETICAL BACKGROUND FOR X-RAY REFLECTIVITY

2.1   X-ray Reflectivity Introduction

After Roentgen discovered X-rays in 1895, X-ray technologies have been widely used in many aspects such as medical uses, scientific study, etc. People have gradually realized how powerful and useful X-ray techniques could be to study the microscale structure of the atoms, crystals, nanoparticles, etc.[14,26,27] X-ray reflectivity is the primary X-ray technique used for measurements described in this thesis. X-ray reflectivity, also known as X-ray specular reflectivity or XRR, is a surface/interface sensitive analytical technique. It is used to probe electron density profiles, averaged over the horizontal plane, as a function of interfacial depth. An early use of X-ray reflectivity to probe the electron density profile of a solid surface was reported by Parratt in 1954.[28] The wavelength of X-ray is generally taken to be from 10^{-12} m to 10^{-8} m (0.01 to 100 Å), though the X-rays used in this thesis have wavelengths of approximately 0.4 Å.

In this chapter, we will introduce the Born approximation to analyze X-ray reflectivity from a liquid-liquid interface roughened by thermal capillary waves.

2.2   X-ray Refractive Index

The refractive index $n = c / v$ of a medium is defined as the ratio of the phase velocity c of a wave in the vacuum to the phase velocity v in the medium itself. Theoretically, the refractive index of electromagnetic waves (EW) can be calculated as $n = \sqrt{\varepsilon\mu}$ where ε is the material's relative permittivity, and μ is its relative permeability. When the material is nonmagnetic ($\mu = 1$), the refractive index equals:

$$n(\vec{r}) = \sqrt{\varepsilon(\vec{r})} \qquad (2.1)$$

$$\varepsilon(\vec{r}) = 1 + \frac{P(\vec{r})}{\varepsilon_0 E(\vec{r})} \tag{2.2}$$

where $P(\vec{r})$ is the polarization which represents dipole moment per unit volume, and $E(\vec{r})$ is the electric field.

For a plane harmonic EW with frequency ω and wave vector k_0, a displacement $-\frac{e}{m\omega^2}E(\vec{r})$ for the free electrons can induced by the electric field $E(\vec{r})$, where m is the mass of the electron. The polarization can be calculated as follow:

$$P(\vec{r}) = -\frac{4\pi\varepsilon_0\rho(\vec{r})r_0}{k_0^2}E(\vec{r}) \tag{2.3}$$

where $k_0 = 2\pi/\lambda$ is the wavenumber of the X-ray, $r_0 = \frac{e^2}{4\pi\varepsilon_0 mc^2}$ is the classical radius of the electron, and $\rho(\vec{r})$ represents the electron density of the medium. Using Eq.(2.2),

$$n(\vec{r}) = \sqrt{1 - \frac{4\pi\rho(\vec{r})r_0}{k_0^2}} \simeq 1 - \frac{2\pi\rho(\vec{r})r_0}{k_0^2} \tag{2.4}$$

Suppose now that in addition to scattering, absorption also happens in the medium. After traveling a distance z within the medium, the X-ray intensity reduces by a factor of $e^{-\mu z}$, where μ is the linear absorption coefficient of X-ray in the medium. Assume that the incident of the X-ray beam on the surface of the medium and vacuum is normal, and then the wave vector changes from k_0 in the vacuum to nk_0 in the medium. The refractive index $n = 1 - \delta + i\beta$:

$$\delta = \frac{2\pi\rho(\vec{r})r_0}{k_0^2} \tag{2.5}$$

$$\beta = \frac{\mu}{2k_0} \tag{2.6}$$

where δ and β is wavelength related.

2.3   Critical Angle of Reflection

The refractive index of the X-ray is smaller than 1 when there is no absorption. Therefore, X-rays shines on the interface of material 1 (n_1, ρ_1) will be refracted by material 2 (n_2, ρ_2) towards ($n_1 > n_2$) or away from ($n_1 < n_2$) the surface depends on the magnitude of n_1, n_2, and when total reflection is reached, the critical angle of the X-ray can be derived by Snell's equation:

$$\cos \alpha_c = \frac{n_2}{n_1} = \frac{1-\delta_2}{1-\delta_1} \cong 1-(\delta_2 - \delta_1) \qquad (2.7)$$

Expanding $\cos \alpha_c$ for small angles yields:

$$\alpha_c = \sqrt{2(\delta_2 - \delta_1)} = \frac{\sqrt{4\pi(\rho_2 - \rho_1)r_0}}{k_0} \qquad (2.8)$$

2.4   Specular Reflectivity

When an X-ray beam moves between two kinds of media with different refraction index, it will be partially reflected and partially transmitted into the bottom media. As shown in Figure 1, the specular reflection is a kind of reflection with the angle of incident equals to the angle of reflection ($\alpha = \beta$, $\theta = 0$), which happens to X-ray when the incident angle is very small.
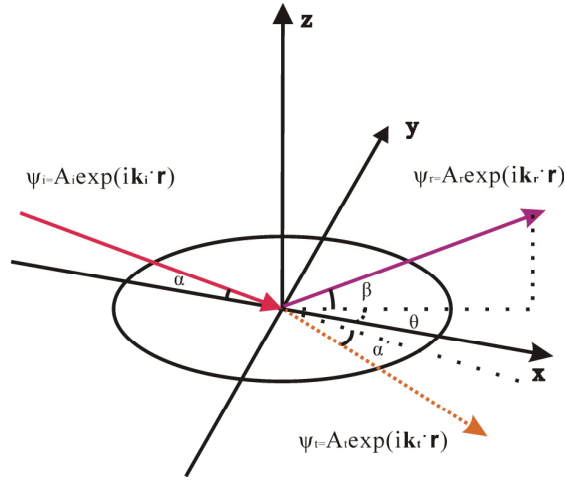
Figure 1. Kinematics of X-ray reflectivity

2.4.1   Ideal Surface : Fresnel Reflectivity

When specular reflectivity occurs on the ideally flat (zero roughness) interface, the reflectivity can be calculated by considering the usual boundary conditions for electromagnetic waves. This type of reflection is known as Fresnel Reflectivity. The amplitudes of the reflected and transmitted waves are the Fresnel reflectance r and Fresnel transmittance t, respectively. As shown in Figure 1, the incident wavevector is $\vec{k_i}$, and the amplitude is A_i. Similarly, the reflected and transmitted wavevectors are $\vec{k_r}$ and $\vec{k_t}$, and amplitudes are $A_r = rA_i$ and $A_t = tA_i$, respectively. By imposing the continuous boundary conditions of the wave and its first derivative at the interface $z = 0$, we have[29-31]:

$$r = \frac{Q_z - Q_s}{Q_z + Q_s} \tag{2.9}$$

$$t = \frac{2Q_z}{Q_z + Q_s} \tag{2.10}$$

where momentum transfer $Q_z = \left| \vec{k_r} - \vec{k_i} \right| = 2k_i \sin \alpha$ and $Q_s = \sqrt{Q_z^2 - 16\pi(\rho_2 - \rho_1)r_0}$ by assuming no absorption.

Since $Q_c = 2k_i \sin \alpha_c = 4\sqrt{\pi(\rho_2 - \rho_1)r_0}$, we can derive $Q_s = \sqrt{Q_z^2 - Q_c^2}$.

The squared-modulus of the reflectance r and transmittance t gives Fresnel reflectivity R and transmissivity T , respectively. Therefore Fresnel reflectivity is given by[31]

$$R_F(Q_z) = \left| \frac{Q_z - \sqrt{Q_z^2 - Q_c^2}}{Q_z + \sqrt{Q_z^2 - Q_c^2}} \right|^2 \tag{2.11}$$

For small values of $Q_z \leq Q_c, R_F(Q_z) = 1$, while for large values of Q_z , Fresnel reflectivity behaves asymptotically as

$$R_F(Q_z) \approx \left(\frac{Q_c}{2Q_z} \right)^4 \tag{2.12}$$

2.4.2   Parratt Formalism

In this thesis, all the X-ray reflectivity data sets are fitted with sliced Box-Slab model, and in this model, the medium is modeled as *N* homogeneous finite thickness layers sandwiched between two infinitely thick homogeneous bulk phases. This method to extend the reflectivity result from a single slab to a stratified medium was named after Parratt.[28] As shown in Figure 2, the total reflectivity is the sum of all the reflections from *N* slabs.

Now, just consider a slab shown in Figure 2, and slab 2 to *N* is infinitely thick substrate.

1. Reflection at interface 0 to 1, amplitude $r_{01} = \dfrac{Q_0 - Q_1}{Q_0 + Q_1}$, where Q_0, Q_1 are momentum transfer of incident

    wavevactor on the interface1.

2. Reflection at interface 1 to 2, followed by transmission at interface 1 to 0, amplitude is $t_{01}r_{12}t_{10}p^2$, where

$$t_{01} = \frac{2Q_0}{Q_0 + Q_1}, t_{10} = \frac{2Q_1}{Q_0 + Q_1}$$. Since the thickness of one slab is Δ, the phase factor $p^2 = e^{-iQ\Delta}$ having

$Q = 2|\vec{k}_{ti}|\sin\alpha$, where $\vec{k}_{ti}$ is the incident wavevector for interface 2.

3. Reflection at interface 1 to 0, then interface 1 to 2, followed by transmission at interface 1 to 0, amplitude

will be $t_{01}r_{12}r_{21}r_{12}t_{10}p^4$.
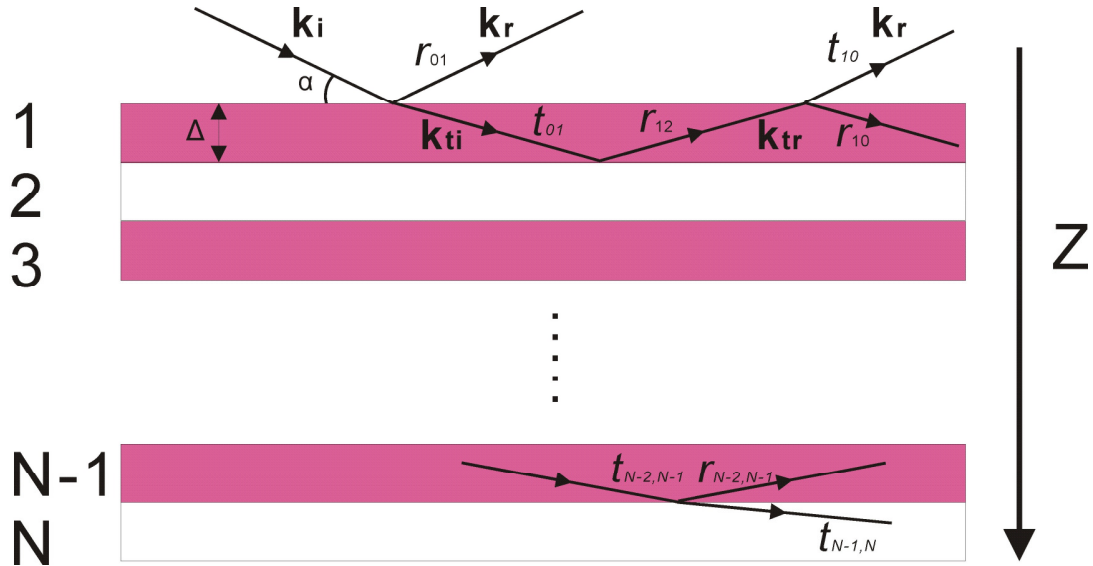
Figure 2. Reflection and transmission from N slabs of finite thickness (Δ). The total reflectivity is the sum of all the reflections from N slabs.

The total amplititude reflectivity is the sum of all the reflections:[28]

$$r_1 = \frac{r_{01} + r_{12}p^2}{1 + r_{01}r_{12}p^2} \tag{2.13}$$

From Eq.(2.13), the reflectivity from i'th slab can be evaluated as

$$r_i = \frac{r_{i-1,i} + r_{i,i+1}p_i^2}{1 + r_{i-1,i}r_{i,i+1}p_i^2} \tag{2.14}$$

where $p_i^2 = e^{-iQ_i\Delta_i}$. One should notice that $r_{N,N+1} = 0$, since there is no interface below the subphase, which

leads to $r_N = r_{N-1,N}$. Eq.(2.14) can be used to calculate r_0 that is the reflection coefficient of the entire system by

summing all the reflections from all the slabs. In this thesis, the reflectivity $|r_0|^2$ calculated from Eq.(2.14) is

referred to as the exact solution.

2.5   Capillary Wave Theory and Electron Density Profile

The investigation on the interface electron density profiles (ED) has started since about a century

ago,[32,33] and theoretical and experimental results made people realize that the change of electron density normal

to the liquid free surface is gradual and continuous. Several possible ED profiles such as, hyperbolic tangent

function associated with mean field theory developed by van der Waals and its modern externsions by Widom

and co-workers,[32] error function associated with capillary wave theory developed by Buff, Lovett,[33] have been

discussed to describe the interfacial structure. Nowadays, the hybrid capillary wave model proposed by Weeks[34]

is more and more popular on investigating the ED profiles. We have utilized the hybrid capillary wave model to

fit our reflectivity data in this thesis. A combination of long wavelength interface fluctuations caused by capillary

waves and short wavelength fluctuations determined by the bulk correlation length is modeled by the hybrid

capillary wave model.[29] This model assumes that these two length scales can be separated.

For a flat interface, in the absence of capillary waves, the intrinsic electron density profile is represented

as $\rho(z)$. When the capillary waves is present, the state of the interface is determined by the instantaneous

configuration of its capillary wave fluctuation, $h(x, y)$. The average of $\rho(z)$ over the interfacial plane x-y can be

written as:

$$\langle \rho(z) \rangle = \int \rho(z - H) \rho_H(H) dH \tag{2.15}$$

where $p_H(H)dH$ is the probability that $H \leq h(x, y) \leq H + dH$. The probability density $p_H(H)$ is independent

of in-plane position (x,y) and is a normal distribution with the mean of zero and variance of interfacial roughness.

Therefore, the intrinsic electron density of a flat interface can be convoluted with a Gaussian probability

distribution. Figure 3 shows a two-layer model ED profile with and without surface roughness. The real ED

profiles of the discrete layers are connected with error function as discussed above. Reflectivity from a graded

ED profile can be calculated by two models, the box model and sliced box model. In this thesis, we use a sliced

box model.
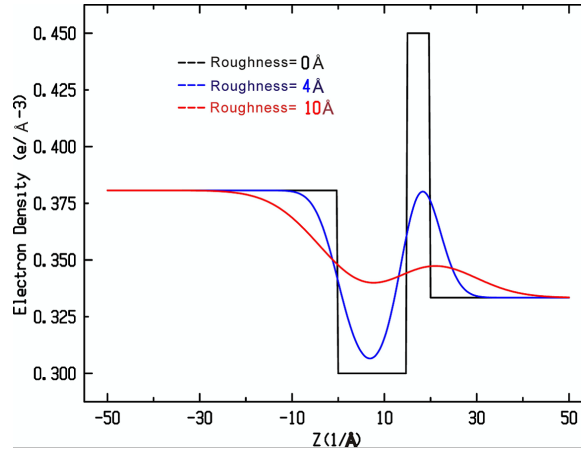
Figure 3. Two-layer model ED profiles with different surface roughness.

From this point forward the roughened electron density will be indicated by $\rho(z)$ without the braces $\langle \rho(z) \rangle$ shown earlier in Eq.(2.15). In the sliced box model, we first build the ED profile $\rho(z)$ by a sum of a few error functions, where each error function represents the interface between a layer and its neighboring layer, as follows:

$$\rho(z) = \frac{1}{2} \sum_{i=0}^{N} erf(\frac{z - z_i}{\sqrt{2}\sigma_i})(\rho_i - \rho_{i+1}) + \frac{(\rho_{N+1} + \rho_0)}{2} \tag{2.16}$$

where N is the number of discrete boxes (each representing a layer of homogeneous electron density) between the top liquid and the liquid subphase, ρ_0 and ρ_{N+1} are the ED of the top liquid and the liquid subphase, σ_i is the roughness at the interface between the ith and $i+1^{st}$ and layer. Then, $\rho(z)$ is sliced into typically several hundred thin slices, for which the ED of a single slice is essentially constant. One can further apply Eq.(2.14) to these hundreds of thin slices to calculate the reflectivity, $|r_0|^2$, which is the exact solution for a graded ED profile. The number of thin slices is considered large enough if adding more slabs does not show any visible change for $|r_0|^2$.

Chapter 3

LIPID MONOLAYER AT AN ELECTRIFIED INTERFACE

3.1   Introduction

It is well known that the membrane potential influences the organization and functionality of cell membranes. For instance, the release of ATPase inhibitor protein from mitochondrial membranes depends on membrane potentials over the range 100-135 mV, allowing ATP synthesis to proceed.[35,36] Other examples include the opening and closing of A-type voltage-gated K^+ channels which occurs at membrane potentials between -100 mV and 100 mV,[37] and the destabilization of cholesterol-phospholipid complexes.[38] Direct effects on the integrity of the biomembrane, such as reversible permeabilization,[39] and electroporation,[40] depend on electric potential differences across the membrane.

Lipid monolayers at the interface between two immiscible electrolyte solutions (ITIES) have been used as a model system for investigating electric field effects on membrane processes.[16,17,41-44] The lipids are dissolved in an organic electrolyte phase and self-assemble at the aqueous-organic liquid-liquid interface. The applied electric potential difference between aqueous and organic electrolyte solutions $\Delta\phi^{w-o} = \phi^{water} - \phi^{organic}$ expresses the difference between the Galvani electric potentials far from the interface in the bulk aqueous phase ϕ^{water} and in the bulk organic phase $\phi^{organic}$. Experiments on interfacial layers of phosphatidylcholine (PC) lipids have demonstrated low and nearly constant values of interfacial tension for a range of negative and slightly positive values of $\Delta\phi^{w-o}$, thus suggesting a nearly constant adsorption of lipids over this range of potentials.[17,44] Increasing $\Delta\phi^{w-o}$ to larger positive values led to an increase in interfacial tension. Mareček, Samec and co-authors suggested that interfacial lipids become positively charged by proton or cation binding at an appropriate value of $\Delta\phi^{w-o}$ and are consequently desorbed from the interface into the bulk organic phase at higher positive values of $\Delta\phi^{w-o}$.[43,44]

Molecular dynamics (MD) simulations have also been used to investigate the role of membrane potential on membrane ordering. Roux el al.[45] developed a computational strategy to impose a transmembrane potential by applying an electric field directed perpendicular to the plane of the biomembrane. With this strategy, the effects on lipid membranes of membrane potentials up to several hundred mV have been simulated. Simulations by Tieleman and co-authors of dioleoylphosphatidyl-choline (DOPC) bilayers demonstrated that the membrane potential reoriented DOPC headgroup dipole moments to induce electroporation.[6,7] Also, Tarek has shown that during electroporation in dimyristoylphosphatidylcholine (DMPC) bilayers, the effect of the transmembrane potential on the dipole moment of the PC headgroup contributes to the reorientation of DMPC.[46]

As part of a program to investigate the role of electrostatic interactions on biomembrane phenomena, we present X-ray reflectivity studies of PC lipid layers at the electrified liquid-liquid interface. X-ray reflectivity probes the electron density profile perpendicular to the interface, which can be interpreted in terms of molecular ordering on the sub-nanometer length scale.[29] This technique has been used numerous times to investigate the ordering of lipid monolayers[27] and lipid-protein interactions at the liquid-vapor interface.[12,14] More recently, X-ray reflectivity has been applied to the study of surfactant and lipid ordering at oil-water interfaces, though the role of electrostatic interactions was not explored. [47]

In the present work, X-ray reflectivity and electrochemical studies of 1-stearoyl-2-oleoyl-sn-glycero-3-phosphocholine (SOPC) lipid monolayers are carried out on the liquid-liquid interface between aqueous (*p*H 7.2) and organic electrolyte solutions. Unsaturated lipids were chosen for study because of their prevalence in natural biomembranes[48] and their relevance for our studies of electrostatic effects on lipid-protein interactions presented in the next chapter. In addition, it is known that these unsaturated lipids form homogeneous monolayers, in contrast to monolayers of saturated lipids that often exhibit domains.[49,50] The absence of domains simplifies the interpretation of X-ray reflectivity measurements which average over the in-plane footprint of the X-ray beam on the interface. The applied electric potential difference $\Delta\phi^{w-o}$ between the bulk electrolyte solutions was varied from -120 mV to 330 mV. Interfacial tension and X-ray reflectivity measurements demonstrate that stable and reproducible SOPC monolayers are formed with surface densities that can be varied from the high densities typical of unsaturated lipids in biomembranes[51] (~ 70 Å^2 per lipid molecule) to densities lower by about a factor of two. Importantly, the stable high density is observed over the range of ±100 mV that is most relevant to

physiological conditions and for planned studies of lipid-protein interactions. Electrochemical cyclic voltammetry and interfacial tension measurements are consistent with results of prior studies on DPPC, L-R-lecithin, and egg-yolk phosphatidylcholine lipids.[15,16,44] X-ray reflectivity measurements probe the variation in layer thickness and electron density profile with applied electric potential difference $\Delta\phi^{w-o}$. These variations agree well with the previously reported adsorption/desorption process of interfacial lipid molecules[15,16,44] and also compare favorably with the results of our molecular dynamics (MD) simulations. The simulations reveal that these variations are accompanied by rotation of the lipid polar headgroups.

3.2   Sample Preparation Procedures

3.2.1   Materials Purification

The unsaturated phospholipid 1-stearoyl-2-oleoyl-*sn*-glycero-3-phosphocholine (SOPC, $C_{44}H_{86}NO_8P$, CAS# 56421-10-4) was used as received from Avanti Lipids. The aqueous electrolytes, NaCl (Alfa Aesar Puratronic®, 99.999% , metals basis) and LiCl (certified ACS, crystal from Fisher Scientific Company) were roasted at 450 ℃ for 45 mins to remove organic contaminants and water. Water from a Nanopure UV Barnstead system was used to prepare aqueous alkali chloride solutions. HEPES buffer solution (1 M) was purchased from Fisher Scientific. 1,2-dichloroethane (DCE, CHROMASOLV, for HPLC, 99.8%) was purchased from Sigma Aldrich and purified by passing it six times through a column of water-saturated aluminum oxide (activated, basic alumina). DCE was further filtered through a 0.2 μm Millipore filter (OMNIPORE membrane filter, PTFE) using a stainless steel pressure filter holder from Sartorius-Stedim Biotech (16249), to remove residual alumina. The organic electrolytes tetradodecylammonium tetrakis(4-chlorophenyl)borate (TDATPBCl) and tetradodecylammonium chloride (TDACl, >97%) were used as received from Aldrich. 1-hexadecanethiol (99%) was purchased from Sigma Aldrich and used as received.

Figure 4. Glass tube for purifying salts by roasting. A slot was opened on the top of the tube.

The supporting electrolytes in the water solutions, alkali metal chlorides (LiCl and NaCl), are roasted in order to remove organic contaminants and moisture including a possibly uncertain amount of crystalline water before use. First, the salt is placed into the middle of a glass tube with the length of 40 cm and radius of 1 cm, shown in Figure 4, through a 24 cm long slot opening on one side. The glass tube was fully covered with aluminum foil leaving one end open and placed in a furnace. The furnace was slowly heated to about 500 ℃ in 10 minutes, and then maintained at that temperature for about half an hour. Because the ends of the glass tube are outside the furnace, we use aluminum foil to cover the open end of the glass tube to reduce the moisture and dust from flowing back into the tube. The furnace is turned off and cools until it reaches room temperature. The salts were collected and stored in clean Pyrex glass bottle and used as desired later.

1,2-dichloroethane, which was used for the organic phase, was purified by passing it 6 times through a column of water saturated aluminum oxide (basic alumina), see Figure 5. Prior to insertion into the column, the basic alumina is mixed with water in a ratio of 40:1 by volume, rocked for 30 mins with a mechanical rocker, then let to sit overnight at room temperature. Glass fiber is inserted into the column with an iron stick covered with clean Kimwipes. The height of the glass fiber in the column is 5 cm. The treated alumina was poured on top of the glass fiber. The glass fiber prevents the alumina from flowing out of the bottom opening of the column. DCE was poured into the column with the valve open. It took about 10 mins for DCE to pass through the column. On the bottom a small beaker was used initially to collect DCE to check for alumina powder or glass fiber that unintentionally passed out of the column. Usually, it is safe to collect DCE after disposing of the first 10 ml that comes out of the column. Subsequently, purified DCE is collected in its original brown glass bottle. DCE is

passed through the column a total of six times. The alumina was replaced with fresh alumina after passing the DCE through the column three times. Purified DCE was stored in the original bottle for further use.
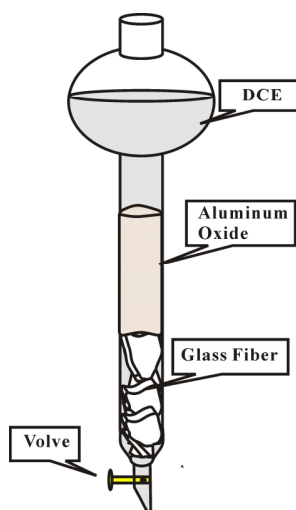
Figure 5. Apparatus for DCE purification.

3.2.2 Solution Preparation

A liter of purified DCE was filtered through a 0.2 μm Millipore filter (Omnipore membrane filter, PTFE) using a stainless steel pressure filter holder (Sartorius-Stedim Biotech model 16249) to remove excess alumina powder that may have passed through the purification column. Filtered DCE (250 ml) was used to dissolve approximately 25 mg SOPC (whose exact mass was measured as described below), 250 ml filtered DCE was used to dissolve TDATPBCl salt to make 10 mM TDATPBCl solution, and 500 ml filtered DCE was kept to make the organic phase solution. Since SOPC powder absorbs moisture and should not be exposed to the air for a long time, the bottle with SOPC powder was weighed directly before and after pouring SOPC into the 250 ml volumetric flask with filtered DCE. Subtracting the "before" and "after" weight provided the weight of SOPC dissolved into the DCE. The SOPC solution was placed in a Blue M Model MSB-1122A-1 Constant Temp

Magni Whirl rocker with slow back and forth rocking motion at room temperature for about 1 hour, then stored

at 5 °C in the refrigerator. The SOPC solution can be used for about one month, though it should be equilibrated

to room temperature before each use. The 10 mM TDATPBCl solution in DCE is saturated with pure water for

about 12 hours while rocking in a customized beaker with a tap at the bottom, shown in Figure 6 to drain the

solution to another clean flask from the bottom.
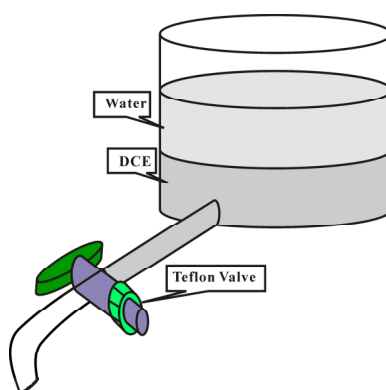
Figure 6. Beaker with tap used to saturate DCE solutions with water.

The NaCl and 1M HEPES buffer solution is dissolved in water to make 100 mM NaCl and 20 mM

HEPES solution (pH 7.2). The aqueous solutions (in 500 ml volumetric flask) were saturated by injecting a few

drops of purified pure DCE (2~3ml) into the solution and placing it in the rocker along with the DCE solution for

about 12 hours, and then both aqueous and DCE solutions were filtered by Millipore filter.

3.2.3   Liquid-Liquid Electrochemical Sample Cell

Figure 7 is a schematic of the four-electrode electrochemical cell used for all reported measurements.

The electric current and potential difference across the liquid-liquid interface can be measured and precisely

controlled, and the interfacial tension measured concurrently with X-ray reflectivity measurements.
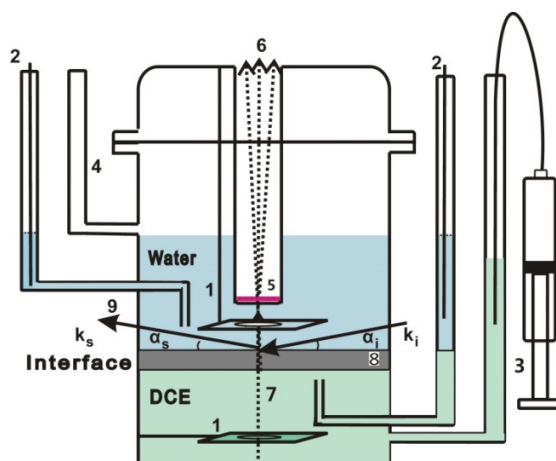
Figure 7. Design of 4-electrode electrochemistry sample cell and X-ray kinematics. The area of the interface between the DCE and water phases is about 38.5 cm^2. (1) Counter electrodes, which is consist of platinum wires attached to square platinum mesh (CE$_{1,2}$) with a hole to supply current. (2) Reference electrodes (RE$_{1,2}$) are AgCl coated Ag wires placed in Luggin capillaries that extend to within 2 to 3 mm of the liquid-liquid interface. Adjusting the volume of the lower DCE phase with a syringe (3) flattens the interface. (4) Pressure release to maintain atmospheric pressure within the cell. (5) Optical grating for quasi-elastic light scattering (QELS) measurements of interfacial tension. (6) Dashed lines indicate the diffracted laser beam used to measure interfacial tension with QELS. (7) Laser beam for QELS measurements of interfacial tension (enters from bottom of cell). As described by Binyang Hou,[52] "The liquid-liquid interface is pinned by the top edge of a strip of Mylar (8), coated as described in the text, which is pressed against the inside of the lower cylindrical part of the glass cell with a strip of stainless spring steel. (9) X-rays pass though the side walls of the cell and traverse the upper aqueous solution to reflect off the liquid-liquid interface".

The scheme of the sample cell is as follow:

Ag | AgCl (RE$_2$) | 100 mM NaCl +20 mM HEPES in H$_2$O ‖ 5 mM TDATPBCl + X μM SOPC in DCE | 10 mM LiCl + saturated TDACl in H$_2$O | AgCl (RE$_1$) | Ag
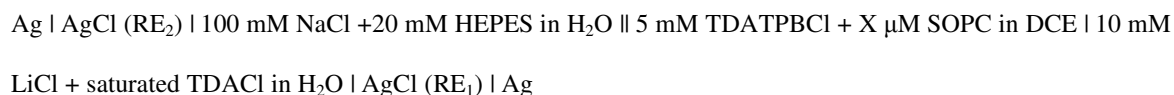
where ‖ represents the interface of interest and X varies from 0 to 12.5. A saturated TDACl solution is prepared by soaking 100 mg TDACl in a gently shaken flask containing 100 ml of 10 mM LiCl aqueous solution. The solutions are electrically conductive as a result of adding electrolytes (NaCl, LiCl, TDATPBCl, and TDACl) into solutions; therefore, the electric potential difference across the interface can be controlled electrochemically to investigate the lipid monolayer response to electric potential differences between the bulk phases. Two platinum meshes (platinum gauze, 52 mesh woven from 0.1 mm diameter wire, 99.9 % metals basis, purchased from Alfa Aesar) are used as counter electrodes. The meshes are large, ~25 cm^2, to ensure that the electric field is uniform across the plane of the interface. The mesh in the top aqueous phase is positioned ~1 cm from the interface; the mesh in the bottom organic phase is ~1.5 cm from the interface. Ag|AgCl reference electrodes placed in Luggin

capillaries located within a few mm of the interface are used to monitor the electric potential difference across the interface. The reference electrode in the Luggin capillary connected to the DCE phase is immersed in 10 mM LiCl and saturated TDACl conductive aqueous solution. All electrodes are connected to Solartron 1287 potentiostat (Solartron Instruments, England) through insulated wires. The applied electric potential difference is controlled and recorded by the Solartron 1287. The electric potential difference across the galvanic cell, measured by the Solartron 1287, is $\Delta\phi_{cell}^{w-o}$. We adopt the rational potential scale[53,54] that approximates the electric potential difference $\Delta\phi^{w-o} = \phi^{water} - \phi^{oil}$ between the aqueous and organic bulk phases (far from interfaces and electrodes) as $\Delta\phi^{w-o} = \Delta\phi_{cell}^{w-o} - \Delta\phi_{pzc}^{w-o}$, where the potential of zero charge, $\Delta\phi_{pzc}^{w-o} = 0.167$ V, is determined from the apex of the electrocapillary curve for the supporting electrolytes.

Tubing sealed at the bottom with float glass extends downward from the cap and is immersed in the water phase to provide a path for the laser beam used for quasi-elastic light scattering (QELS) measurements of interfacial tension. A 1 cm diameter hole in the middle of each Pt mesh allows for passage of this laser beam. Comparative X-ray reflectivity measurements with and without this hole were identical, indicating that the hole had a negligible effect on the interfacial structure.

X-ray reflectivity measurements require a very flat interface. Pinning the interface to the cell wall and adjusting the volume of the lower DCE phase accomplishes this. The interface can be pinned by the top edge of a hydrophobic strip when the cell glass is hydrophilic. The cell was soaked in concentrated (98%) sulfuric acid solution of ammonium persulfate (18 g per liter of H_2SO_4) for 5 hours to render it hydrophilic. In previous experiments that studied the interfacial distribution of just the supporting electrolytes, a Teflon strip was used to pin the interface.[52,55,56] In the presence of interfacial SOPC lipids, the Teflon strip proved inadequate to pin the interface. Instead, the interface was pinned to the top edge of a hydrophobic gold-coated strip of Mylar prepared as follows. After evaporation of a 100 nm thick gold layer onto a 1.5 cm wide by 20 cm long strip of 0.18 mm thick Mylar (purchased from ePLASTICS), a 1-hexadecanethiol layer was self-assembled on the gold by immersing the Mylar strip in 4 mM 1-hexadecanethiol for 2 days under argon or nitrogen atmosphere. The Mylar strip was pressed against the inside of the glass cell with a thin strip of stainless steel and its upper edge positioned vertically midway between the ends of the Luggin capillaries (Figure 7). Once the interface is pinned

by the top edge of the Mylar strip, adjusting the volume of the bottom phase with a syringe and leveling the cell along axes parallel and perpendicular to the incident X-ray beam with a tilt stage, described below, produces a very flat interface. The curvature of the interface can be determined by X-ray reflection.
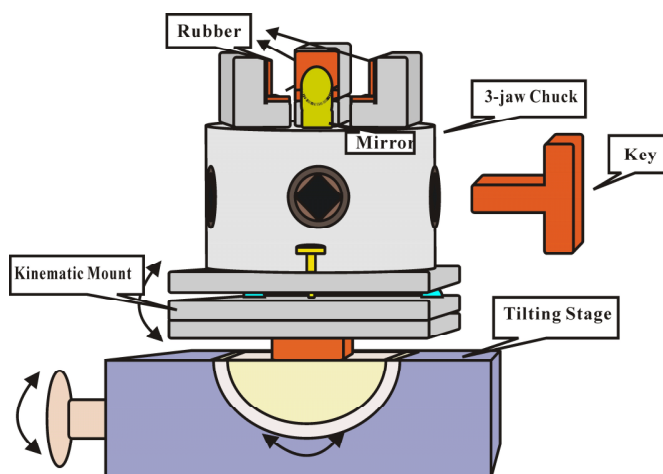
Figure 8. Illustration of the tilting stage, kinematic mount, and 3-jaw chuck used to mount the sample cell.

Fine adjustment to level the interface to meet the requirements of X-ray reflectivity measurements is done with the tilting stage and kinetic mount illustrated in Figure 8. During the X-ray measurement at the Advanced Photon Source, a 3-jaw chuck, mounted to the tilting stage and kinematic mount, holds the electrochemical sample cell to prevent its movement during the process of changing the X-ray incident angle. Six pieces of rubber are attached to the jaws to protect the thin glass wall. Three square holes on the sides of the 3-jaw chuck can be rotated by a key to adjust the opening of the chuck. A 45 degree optical mirror is placed in the middle of the 3-jaw chuck in order to direct a laser beam onto the bottom of the sample cell. The laser beam is used for quasi-elastic light scattering measurements of interfacial tension, described later. The tilt stage levels the cell along the direction of the X-ray beam and the kinematic mount levels the cell in the horizontal direction transverse to the X-ray beam. Combining this leveling with modification of the volume of the lower phase with a syringe, previously described, produces a very flat interface.

3.2.4   Sample Cell Preparation

Flasks, sample cell and designed beaker were rinsed with ACS certified methanol, acetone and again methanol each three times and then plenty of water. They were then soaked in a sulfuric acid bath (18 g ammonium persulfate per liter of 98% H_2SO_4) for several hours. Afterwards, they were rinsed with plenty of pure water. An alternative procedure used for experiments at the Advanced Photon Source consisted of soaking the sample cell in the sulfuric acid bath for 30 minutes, rinsing with plenty of water, then soaking in 5 M NaOH solution for 30 minutes. The NaOH solution produces a hydrophilic glass wall faster than sulfuric acid; however, this should not be done on a regular basis because concentrated NaOH solution etches the glass wall of the sample cell. High purity nitrogen gas was used to blow out water drops that remain in the glass cell. A Pasteur pipette attached to an vacuum pump (referred to as an aspirator) was used to remove water left on the tip of the Luggin capillaries, which can interfere with electrochemical measurements. The aspirator pipette was also used to remove water from the lower platinum mesh to prevent the formation of water drops that can rise to the liquid-liquid interface during the experiment.

The gold-coated Mylar strip with the supporting stainless steel strip is placed into the sample cell with clean tweezers. To do this, a thin strip of stainless steel is placed on top of a Mylar strip on a clean alpha wipe, then they are curved into a circle together. The Mylar strip surrounds the stainless steel strip. A tweezer is used to hold the circle, and place it into the sample cell. The tweezer is slowly removed while a picker gently presses the connection of the Mylar strip to prevent it from moving with the tweezer. The upper edge of the strip is carefully leveled with a height gauge and two clean pickers. The SOPC solution, equilibrated to room temperature is diluted with 10 mM TDATPBCl solution, concentrated SOPC solution and saturated pure DCE solution to make an organic solution of the appropriate concentration. This procedure is used because the highly concentration SOPC stock solution in DCE cannot contain water. A 25 ml glass pipette is used to transfer the organic solution into the sample cell slowly and carefully until the interface is higher than the tip of the lower Luggin capillary. This requires several fillings of the pipette. The liquid is added by dripping it against the side of the sample cell to avoid drop formation or splashing. Then, a few drops of DCE solution are added to the outside tube of the lower Luggin capillary to remove any residual water left in the capillary. If the capillary is free of water, the level of DCE in the Luggin capillary changes smoothly. Undesired water in the Luggin capillary can block the flow of

DCE. If water is present, a rubber bulb placed on the opening of the outside tube is used to blow out the residual water residual. The organic solution surface is then aspirated carefully with a Pasteur pipette.

Water solution is then added slowly onto the DCE solution with a 25 ml pipette whose tip was resting against the inner wall of the sample cell. The weight of the added water will distort the liquid-liquid interface. The level of liquid-liquid interface should be carefully monitored during the process of adding water solution to prevent the interface from catching the tip of the lower Luggin capillary. If this happens, water solution can flow into the Luggin capillary, which will contaminate the electrochemical circuit. In this case the water must be removed with a rubber bulb or an aspirator as described above. During the process of adding water solution, a small amount of DCE solution can rise to the water-vapor interface and quickly evaporate, thus, leaving behind a precipitate of TDATPBCl salt. After each addition of 25 ml the top surface of the water is aspirated to keep it clean. If this precipitate is not removed it can eventually fall through the water phase to land on the liquid-liquid interface and disturb the X-ray measurements of this interface.

After the cell is filled with the two liquid phases, the sample cell is covered with a glass top (Figure 7). A 10 mM LiCl plus saturated TDACl solution is added into the outer tube of the lower Luggin capillary. Reference electrodes (Ag wires coated with AgCl) are added into both Luggin capillaries. Before connecting the sample cell to the Solartron potentiostat, the electrodes of the potentiostat are connected to a black box with a 1000 Ω resistor inside to reset the machine. After that, the Solartron was connected to the sample cell reference and counter electrodes through four grounded wires.

After preparation, the sample cell is represented by the scheme presented earlier: Ag|AgCl|100 mM NaCl +20 mM HEPES (H_2O)||5 mM TDATPBCl + X μM SOPC (DCE)|10 mM LiCl + saturated TDACl (H_2O)|AgCl|Ag. In this scheme, Ag|AgCl represents the electrodes in the Luggin capillaries. One electrode is directly in contact with the bulk water phase, which contains 100 mM NaCl and 20 mM HEPES. The latter buffers the water to a pH value of 7.2. The DCE phase is below the water solution. It consists of 5 mM TDATPBCl and X μM SOPC (DCE). The X refers to different concentration of SOPC. The TDATPBCl assures the conductivity of DCE phase. In the Luggin capillary connected to the DCE phase, a water solution containing

10 mM LiCl and saturated TDACl is placed on top of the DCE phase. A Ag|AgCl electrode is placed into this water solution to measure the potential difference $\Delta\phi_{cell}^{w-o}$ across the entire electrochemical cell.

3.2.5   Interfacial Tension Measurements

3.2.5.1   Theoretical Background of Quasi-Elastic Laser Scattering

The relation between the frequency ω_R of a wave on a liquid surface and its surface wave vector $\vec{k}$ and wave number k_0 is:

$$\omega_R^2 = gk_0 + \gamma k_0^3 / \rho_m \tag{3.1}$$

where g is the gravitational acceleration, γ is the surface tension coefficient and ρ_m is the fluid mass density. When wave vector k_0 is in the range of $k_0 > 10^4 m^{-1}$, the corresponding ripples are capillary waves whose frequencies are dominated by surface tension rather than gravity.[48]

QELS method has been developed and employed to examine the dispersion relationship of the frequency and surface wavevector of the capillary wave and to evaluate the interfacial tension of liquid surfaces[57-61] and the interfaces.[62-64] A QELS apparatus was built in our lab as shown in Figure 9, and the interfacial tension measurement in this thesis was carried out with QELS. Detailed operating procedures for the QELS setup can be found in Appendix A.

The interfacial ripple behaves as a moving diffraction grating whose properties depend upon the restoring forces due to surface tension and gravity and the damping force due to bulk viscosity. The angular study of the scattered laser intensity probes the spatial distribution of the fluctuations of the surface position, shown in Figure 10.
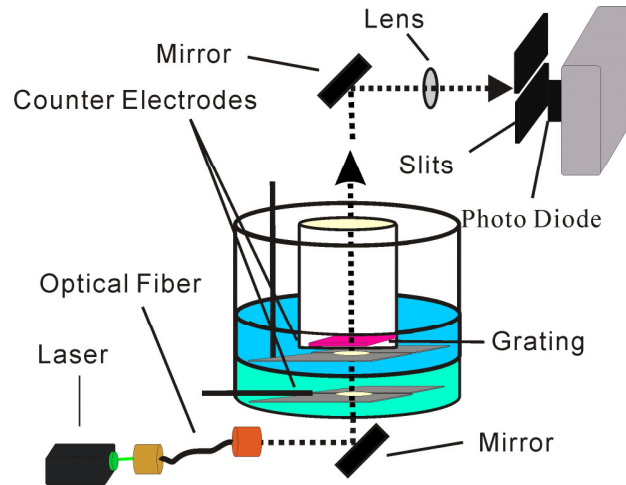
Figure 9. Illustration of quasi-elastic light scattering apparatus. A green Nd:YAG laser beam (wavelength 532 nm, 25 mW, Crystal Laser Corp.) is transmitted through the liquid-liquid interface, then scattered from a grating fabricated in the Nano Core Facility of the University of Illinois at Chicago. The optical fiber is purchased from OZ optics. The grating consists of float glass onto which chromium stripes 20 μm wide separated by 230 μm (for a grating constant 250 μm) were evaporated. The scattered laser beam is reflected by a 45 degree mirror and focused by a convex lens (f =2m). The mirror is 1" Broadband Dielectric Mirror (400-750 nm) purchased from Thorlabs. The optical heterodyne signal incident on a S1133 Hamamatsu photodiode was fed into a wide-band amplifier (model 13AMP005 Melles–Griot). A fast Fourier transform of the amplified signal was done electronically by FFT analyzer SRS760 (Stanford Research).
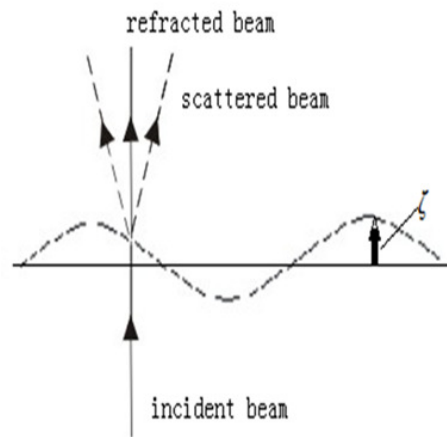
Figure 10. Incident laser beam reflected by the vertical displacement of ripples in spatial mode.

The spatial mode of the vertical displacement at time t of the surface can be described as:

$$\zeta_k(t) = A^{-1} \int d^2 r \zeta(\vec{r},t) \exp(i\vec{k} \cdot \vec{r})$$ (3.2)

where $\zeta(\vec{r},t)$ denotes the vertical displacement at time t of the surface element whose projection on the horizontal plane is $\vec{r}$. At thermal equilibrium, $\zeta(\vec{r},t)$ is random and the average displacement of the interface $\overline{\zeta(\vec{r},t)}$ is defined to be zero. The space-time correlation function $\overline{\zeta(\vec{r},t)\zeta(\vec{r}+\vec{\Delta},t+\tau)}$ satisfies invariance with respect to space and time translation, where $\vec{\Delta}$ represents the change in in-plane position $\vec{r}$ after time τ and $\vec{r}' = \vec{r} + \vec{\Delta}$ the projection of vertical displacement onto the vertical plane at time $t+\tau$. We use $g(\vec{\Delta},\tau)$ to represent the correlation function. Using the translation invariance combined with Eq.(3.2) we can write[65]

$$\overline{\zeta_k(t)\zeta_{k'}^*(t+\tau)} = A^{-2} \int d^2\Delta\, g(\vec{\Delta},\tau) \exp\frac{i(\vec{k}+\vec{k'}) \cdot \vec{r}}{2} \times \int d^2 R \exp i(\vec{k'}-\vec{k}) \cdot \vec{R}$$ (3.3)

where $\vec{R} = (\vec{r}'+\vec{r})/2$. Because $\int d^2 R \exp i(\vec{k'}-\vec{k}) \cdot \vec{R}$ equals zero unless $\vec{k'} = \vec{k}$, equation (3.7) can be transformed into:

$$G_k(\tau) = \overline{\zeta_k(t)\zeta_k^*(t+\tau)} = A^{-2} \int d^2\Delta\, g(\vec{\Delta},\tau) \exp i\vec{k} \cdot \vec{r}$$ (3.4)

Eq.(3.4) shows that the time correlation function $G_k(\tau)$ depends on $|\vec{k}|$ only. The Fourier transformation of $G_k(\tau)$, known as the surface fluctuation power spectrum, is determined by Fast Fourier transform (FFT) analyzer of the scattered laser beam. The magnitude of the power scattering can be calculated as follows:

$$P_k(\omega) = (2\pi)^{-1} \int_{-\infty}^{+\infty} d\tau\, G_k(\tau) \exp(i\omega\tau)$$ (3.5)

3.2.5.2 QELS Measurement and Data analysis

A 25 mW green Nd:YAG laser (wavelength 532 nm) purchased from Crystal Laser Corp. was scattered at normal incidence to the liquid-liquid interface. A grating was made in Nanotechnology Core Facility of UIC

with grating constant 250 um. The dark lines of the grating are 20 um wide, and the transparent stripe between them is 230 um wide. The scattered light is incident on a photodiode purchased from Hamamatsu (S1133) and the diode signal is amplified by a wide-band amplifier (Melles–Griot model #13AMP005). A fast Fourier transform of the amplified signal was computed by Stanford Research model SRS760.
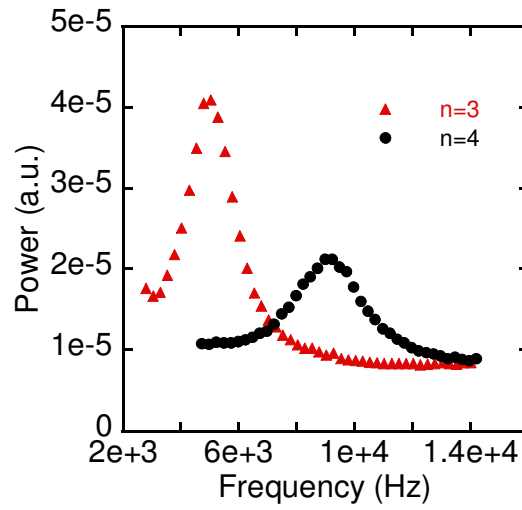
Figure 11. Power spectrum from different diffraction spots (n) for the capillary waves of the water-DCE interface.

Figure 11 displays the power spectrum for capillary waves of the water-DCE interface in the absence of SOPC. The peak frequency f_p represents the measured capillary wave frequency at certain wavenumber. The power spectrum is fit to a Lorentzian function with a linear background. Lamb's equation,[66] expressed in Eq.(3.6), is the approximate dispersion relation of the interface when the viscosity of both water and DCE phases are ignored. It describes the relationship between interfacial tension γ, mass density of water ($\rho_{m,w}$) and organic phase ($\rho_{m,o}$), wave number k_0 and the frequency of the capillary wave f_c :

$$f_c^2 \approx \frac{\gamma k_0^3}{(2\pi)^2 \left(\rho_{m,o} + \rho_{m,w} \right)} \qquad (3.6)$$

In this paper, the viscosities of both phases were taken into account by adding an offset to the frequency calculated from Lamb's equation to better approximate the capillary wave frequency f_p :[65,67,68]

$$f_p \approx f_c - \frac{f_c^{1/2} k_0 \left[\left(\rho_{m,w} \eta_w \right)^{1/2} + \left(\rho_{m,o} \eta_o \right)^{1/2} \right]}{4\sqrt{\pi}(\rho_{m,w} + \rho_{m,o})} \tag{3.7}$$

where $\eta_{w,o}$ is the kinematic viscosity of the water and organic phases. Therefore, the interfacial tension can be calculated from the peak frequency of the power spectrum for $\rho_{m,w} = 0.997 \times 10^3$ kg m^{-3}, $\rho_{m,o} = 1.246 \times 10^3$ kg m^{-3}, $\eta_w = 0.89 \times 10^{-3}$ kg m^{-1}s^{-1}, and $\eta_o = 0.78 \times 10^{-3}$ kg m^{-1}s^{-1}.[68]

The surface wave number k_0 was chosen by an external grating, which functioned as a local oscillator. In our apparatus, the incident angle of the laser beam is set to 90 degree as shown in Figure 12. Combining the scattering of the laser beam from a time-varying liquid surface wave and from a grating (Figure 12), the surface wave number k_0 can be expressed as[68]

$$k_0 = \frac{2\pi}{\lambda} \sin \alpha' \tag{3.8}$$

where α' is the angle shown in Figure 12 between the scattered beam and the direct beam, and λ is the wavelength of the laser. Compared to the distance between the grating and photodiode detector (~1.5 m), the distance between the interface and grating (~ 1.5 cm) is negligible. Note that neglecting this 1.5 cm offset leads to a 1% reduction in k_0 and a 3% increase in interfacial tension, which ultimately produces a negligible 1.5% reduction in interfacial roughness. As result, the angle α shown in Figure 12 is a good approximation for α'. The angle α and surface wave number k_0 can be derived from the grating constant d and the chosen diffraction order n.
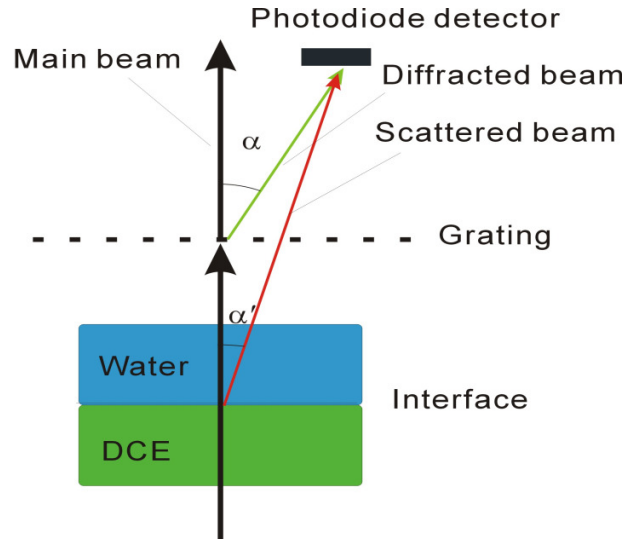
Figure 12. Diagram of laser scattering from interface and grating.

The surface wave number k_0 can be calculated as follows:

$$\sin \alpha = \frac{n\lambda}{d} \tag{3.9}$$

$$k_0 = \frac{2\pi}{\lambda} \sin \alpha' \approx \frac{2\pi n}{d}, \quad \alpha' \approx \alpha \tag{3.10}$$

3.2.5.3   Advantage of External Grating

The grating constant and diffraction order of the grating are well defined and easily measured, which significantly reduces the uncertainty of the measurement. The grating also functions as a local oscillator to optimize the signal of the scattered beam. The laser beam, quasi-elastically scattered by capillary waves at the liquid-liquid interface, is accompanied by a frequency shift $\omega_L \pm \omega_0$ [69] when the grating is added. The power of the signal i on the photodiode can be calculated as a combination of the amplitude of the diffracted beam A_0 and scattered beam A_s:

$$i \propto \left| A_0 e^{i\omega_L t} + A_s e^{i(\omega_L + \omega_0)t} \right|^2 \approx A_0 A_s^* e^{i\omega_0 t} + \left| A_s \right|^2 e^{2i\omega_0 t} + c.c \tag{3.11}$$

where ω_L is the angular frequency of the laser; ω_0 is the angular frequency of the capillary wave , as well as the power spectrum peak frequency. The width ratio of the dark and transparent parts of the external grating (equivalently, its transmission) is chosen so that $A_0 \gg A_s \gg \delta A_0$ to ensure that heterodyne detection is achieved,[57,58] where the amplitude of laser intrinsic noise is represented as δA_0. From Eq.(3.11), the term $A_0 A_s^*$ clearly shows that the contribution of the time variations part to the photodiode current is enlarged A_0 times by the diffracted beam. It means the signal from the scattering beam is amplified and the accuracy of the interfacial tension measurement is improved significantly.

3.2.6   Cyclic Voltammogram (CV)

Cyclic voltammograms are measured by cyclically and linearly varying the cell electric potential difference between initial and final values. This technique has been used to probe the reactivity, kinetics of reaction and/or the mass transfer process of the electrochemical system over a large range of potentials in a single or multiple sweeps.[70] Here, we probed the mass transfer process in order to determine the working potential window for the samples studied, as well as the adsorption/desorption process of lipid monolayer. Cyclic voltammograms were measured at a scan rate of 5 mV/s with our four-electrode sample cell. The Solartron potentiostat measures the current across the interface under a dynamically varying potential. A detailed description of this measurement appears elsewhere.[71]

3.2.7   X-ray Reflectivity

The liquid surface reflectometer used to meausure the X-ray reflectivity is located in the ChemMatCARS beamline 15-ID at the Advanced Photon Source (Argonne National Laboratory, USA). [29,47,71] In the thesis, the energy of the X-ray is selected to be 30kev with wavelength $\lambda = 0.4133 \pm 0.00005$ Å, and as mentioned in Binyang Hou's paper,[52] "the size of the beam ($\sim 0.018 \times 3$ mm^2, height by width) incident on the sample was set by a rectangular aperture (0.015×3 mm^2, height by width) positioned 68 cm before the sample". The reflected X-rays were recorded by a CCD detector (Bruker APEXII) placed 3.19 m from the sample center. Two slits were positioned between sample and CCD. A slit with a 5 mm vertical gap was positioned 0.5 m in front of CCD to reduce excess intensity on the CCD and block the direct, un-reflected beam. Its vertical position tracked the reflected X-ray beam. A second slit of dimensions 1 x 4 mm^2 was positioned 685.8 mm downstream

of the sample center to reduce background scattering from the sample. A window size of 60 pixels x 30 pixels (h x w, where each square pixel is 60 micrometers on a side) of the electronic slit was selected on the CCD to extract the reflectivity, and background is selected at ±0.1 degree off the reflectivity in a direction parallel to the interface. Final reflectivity intensity equals the intensity in the electronic slit minus the background.

3.2.8   Molecular Dynamics Simulations

3.2.8.1   Methodology.

Our collaborators, Irena Yzeiri and Petr Kral, computed atomistic molecular dynamics (MD) simulations using NAMD, TIP3P model for water, CHARMM36 force field for lipids, and the CHARMM27 force field for everything else.[72-74] Non-bonding van der Waals (vdW) coupling between the ith and j^{th} atoms is described by Lennard-Jones potentials. The short-range cutoffs for Coulombic and vdW interactions are, respectively, 10 Å and 12 Å. The time step is 1 fs. Langevin dynamics with a damping coefficient of 0.01 ps^{-1} sped up the simulations.[75,76] Particle mesh Ewald summation method (PME) was used for electrostatic interactions.[77] Simulations were run for 200 – 250 ns to reach a steady state interfacial structure. The NAP_zT (P = 1 atm, T = 300 K) ensemble was used with constant area in the x-y plane. Under constant area simulations, the x-y simulation cell parameters and thus the lipid density are kept constant at values that match the experimental values. Fluctuations of the simulation box size occur only in the z direction and the total height Z of the box is determined at the end of the simulation.

3.2.8.2   Systems.

Simulated systems consist of five layers in the following order: 1) aqueous solution (200 mM NaCl), 2) SOPC monolayer (100 SOPC lipids), 3) DCE solution (200 mM BTPPA$^+$ / TPBCl$^-$ (bis-triphenylphosphoranylidene / tetrakis(4-chlorophenyl)borate)), 4) SOPC monolayer (100 SOPC lipids), 5) aqueous solution (200 mM NaCl). We present results for only the top SOPC monolayer; the bottom monolayer prevents mixing of the solvents and improves system stability. In the absence of an applied electric field, the bottom half of the unit cell is practically a mirror image of the top. This is no longer true when an electric field is applied in the direction perpendicular to the lipid monolayer. In addition, significant monolayer curvature out of the x-y plane is inhibited by the application of a small force (0.2 kcal/mol/Å) on the C2 carbon of each lipid.

The choice of systems with different areas per lipid and applied electric fields (see Table 1) is guided by experimental conditions. The organic cation BTPPA$^+$ is used in place of the experimental cation TDA$^+$ to reduce simulation time. Under conditions of positive electric potential difference, $\Delta\phi^{w-o} > 0$, organic cations are depleted from the region adjacent to the lipid monolayer. Therefore, organic cations only influence the potential drop in the DCE phase and use of a slightly different cation in the organic solvent should not significantly affect our results.

Table 1. Simulation systems[a]

area per lipid (Å^2)	unit cell ($X \times Y \times Z$) (Å^3)	electric field (kcal mol^{-1} Å^{-1} e^{-1})	electric potential difference (V)
72.25	($85 \times 85 \times 288$)	-0.01839	-0.12
72.25	($85 \times 85 \times 288$)	0.00000	0.00
81.00	($90 \times 90 \times 260$)	0.03095	0.23
90.25	($95 \times 95 \times 233$)	0.03947	0.28
121.00	($110 \times 110 \times 175$)	0.07200	0.33

[a] The total height of the simulation cell Z is obtained at the end of the simulations.

3.3 Results and Analysis

3.3.1 Cyclic Voltammetry

Cyclic Voltammetry was used to probe the interface between water and DCE solution. With and without SOPC dissolved in the DCE phase, two cyclic voltammograms from the interface are shown in Figure 13.. Excess current in the presence of SOPC is observed for $\Delta\phi^{w-o} > 0.2$ V and has been attributed to lipids leaving the interface and re-dissolving in the bulk DCE phase.[17] As described in Binyang Hou's paper,[52] "The currents are much lower during X-ray reflectivity and interfacial tension measurements because the voltage ramping rate is lower, 1 mV s^{-1}, and the measurements take place after relaxation to a steady state. The maximum electric

potential differences for X-ray reflectivity measurements were chosen to limit the maximum currents to 0.13 µA cm^{-2} to reduce the effect of ion transport on these measurements. Typical values of relaxed currents in the central part of the potential window are 0.03 µA cm^{-2}. "
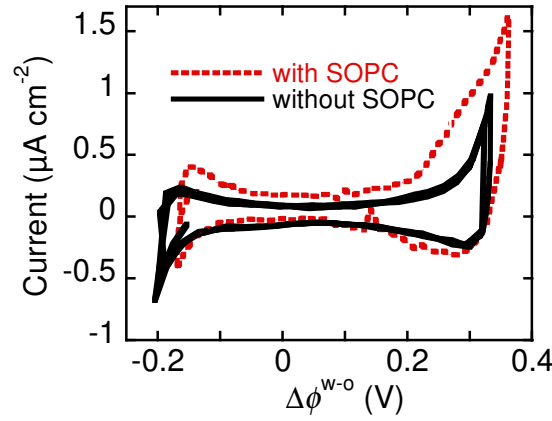
Figure 13. Cyclic voltammograms measured at a scan rate of 5 mV s^{-1} for interfaces between and aqueous solution of 100 mM NaCl + 20 mM HEPES (*p*H 7.2) and a DCE solution of 5 mM TDATPBCl in the absence (solid line – 3 cycles) and presence (dashed line – 1 cycle) of 3 µM SOPC in the DCE phase. The electric potential difference $\Delta\phi^{w-o} = \Delta\phi_{cell}^{w-o} - \Delta\phi_{pzc}^{w-o}$ is the difference between the potential difference applied across the galvanic cell $\Delta\phi_{cell}^{w-o}$ and the potential of zero charge $\Delta\phi_{pzc}^{w-o} = 0.167$ V .

3.3.2   Interfacial Tension Measurements

Figure 14 shows the interfacial tension γ as a function of electric potential difference $\Delta\phi^{w-o} = \Delta\phi_{cell}^{w-o} - \Delta\phi_{pzc}^{w-o}$, *i.e.*, the electrocapillary curve, for samples with different concentrations of SOPC in the DCE phase. As shown in Figure 14, the potential of zero charge is determined to be $\Delta\phi_{pzc}^{w-o} = 0.167 \pm 0.008$ V in the absence of SOPC.[52]. Binyang Hou wrote that, "According to Lippmann's equation,[78] the excess charge per unit area of the interface $Q_{tot}(\Delta\phi^{w-o})$ is expressed as $Q_{tot}(\Delta\phi^{w-o}) = -(\partial\gamma/\partial\Delta\phi^{w-o})_{T,p,\mu_i}$, where T is the thermodynamic temperature, p is the external pressure and μ_i is the chemical potential of species i. As described

previously, a hyperbolic cosine describes the data well enough to determine the potential of zero charge, $\Delta\phi_{pzc}^{w-o}$,

for which $Q_{tot}(\Delta\phi^{w-o}) = 0$."[52] In this thesis, a hyperbolic cosine function is used to fit the data in order to

determin the potential of zero charge.
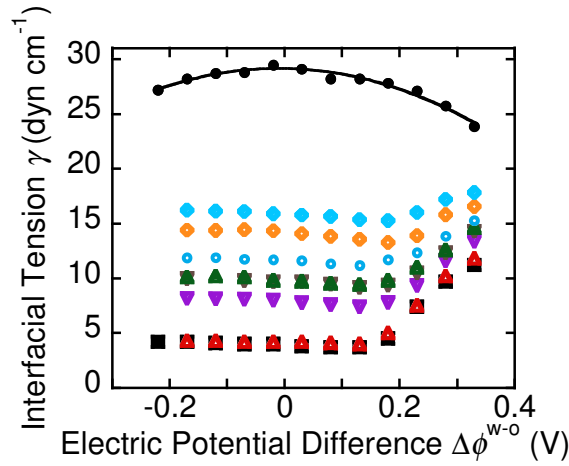
Figure 14. The interfacial tension γ measured under different potential difference $\Delta\phi^{w-o}$ ($T = 23$ °C) for interfaces between a DCE solution of X μM SOPC and 5 mM TDATPBCl and an aqueous solution of 0.1 M NaCl and 20 mM HEPES, with X = 0 (●), 1.6 (♦), 2 (◊), 2.4 (○), 3 (▽), 3.4 (▲), 5 (▼), 10 (Δ, red), 12.5 (■).

Figure 14 shows that the interfacial tension γ for a fixed concentration sample is nearly constant below

0.2 V, but increases above 0.2 V. This variation in γ is reversible. Qualitatively similar variations in interfacial

tension have been reported for other lipids at the electrified liquid-liquid interface[15,17,79] The surface excess or

adsorption of SOPC at the interface can be calculated from the variation of γ with sample concentration,

according to $(\partial\gamma/\partial\ln c)_{\Delta\phi^{w-o},\mu_i,T,p} = -RT\,\Gamma$, where Γ is the Gibbs surface excess, c is the mole fraction of

SOPC, R is the gas constant, and the concentrations of all other components are held constant.[79] The linear

relation between γ and log c shown in Figure 15 indicates a constant adsorption Γ over a range of bulk

concentration for a fixed value of $\Delta\phi^{w-o}$. The deviation from linearity that occurs upon increasing log c above a

certain value indicates that the critical micelle concentration (CMC) has been exceeded, though the interface

remains saturated with SOPC lipids. Linearity between γ and log c holds for all values of $\Delta\phi^{w-o}$ for the 3 µM

SOPC sample that will be studied with X-ray reflectivity. The other SOPC concentration studied by X-ray

reflectivity, 12.5 µM, is above the CMC.
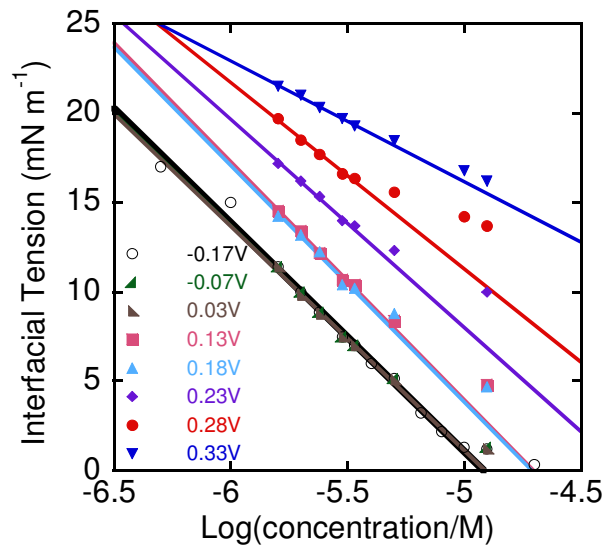
Figure 15. Interfacial tension as a function of the logarithm of the molar concentration of SOPC determined from the data shown in Figure 14. For clarity, the tension values for $\Delta\phi^{w-o}$ = -0.17 V, -0.07 V, and 0.03 V are offset by -3 mN/m, $\Delta\phi^{w-o}$ = 0.23 V and 0.28 V are offset by 4 mN/m, and $\Delta\phi^{w-o}$ = 0.33 V is offset by 5 mN/m. Error bars are smaller than the symbol size.

Table 2 lists the slopes of the lines drawn in Figure 15 and the associated interfacial area per SOPC

molecule for 3 µM SOPC samples. Essentially the same values are expected for the 12.5 µM SOPC samples.

Values of 70-74 Å^2 per SOPC molecule are measured for $\Delta\phi^{w-o}$ < 0.2 V. These are in good agreement with

values of 70.1 Å^2 and 66.5 Å^2 reported for DOPC and DPPC bilayer vesicles, respectively, and the value of 71 Å

for DOPC monolayers at the electrified liquid-liquid interface.[79,80] Table 2 also demonstrates an increase in

interfacial SOPC area per molecule for increasing $\Delta\phi^{w-o}$ > 0.2 V. This is consistent with the additional current

observed in the cyclic voltammogram in Figure 13 for $\Delta\phi^{w-o} > 0.2$ V if, as suggested by Marecek and others, neutral SOPC lipids are charged either by protonation or complexation with other cations prior to desorbing from the interface.[15,17,79] A minimum in the area per SOPC is observed for $\Delta\phi^{w-o}$ between 0.13 V and 0.18 V. This is consistent with the minimum in interfacial tension observed in Figure 14 for this range of $\Delta\phi^{w-o}$.

Table 2. Inverse surface density (area per molecule) of SOPC calculated from the data in Figure 15 for 3 μM SOPC samples

$\Delta\phi^{w-o}$(V)	Slope (mN m^{-1})	Area per Molecule(Å^2)
-0.17	-12.78±0.28	74±2
-0.07	-12.78±0.28	74±2
0.03	-12.78±0.28	74±2
0.13	-13.31±0.41	70±2
0.18	-13.31±0.41	70±2
0.23	-11.65±0.65	80±4
0.28	-10.43±0.49	85±4
0.33	-6.76±0.55	123±10

3.3.3   X-ray Reflectivity Data

Figure 16 illustrates X-ray reflectivity data normalized to the Fresnel reflectivity $R_F(Q_z)$ (calculated for a flat, structureless interface[29]) from samples with 3 μM and 12.5 μM SOPC in the DCE phase. X-ray reflectivity probes the gradient of the electron density variation with depth, $d(\rho(z))/dz$, where $\rho(z)$ has been

averaged over the in-plane ($x - y$) region of the X-ray footprint on the sample interface and the coordinate z is perpendicular to the interface. The "Kiessig fringes" generated by the phase shift of the X-ray reflections from the lipid monolayer is shown in the data. The presence of these fringes indicates that the lipid layer has a well-defined electron density profile perpendicular to the interface. Reflectivity measurements for $-0.15 \text{ V} \leq \Delta\phi^{w-o} \leq 0.13 \text{ V}$ are nearly indistinguishable, indicating that the electron density profile of the SOPC layer is essentially unaffected over this biologically relevant range of electric potential difference. Larger positive values of $\Delta\phi^{w-o}$ lead to successive variations in the measured reflectivity as indicated in Figure 16 by the monotonic shift in reflectivity minima and maxima. As discussed below, the qualitative differences in $R(Q_z)/R_F(Q_z)$ for the two different concentrations of SOPC are primarily the result of the smaller interfacial tension of the larger concentration (12.5 µM SOPC) sample, whose larger interfacial roughness influences the X-ray reflectivity.
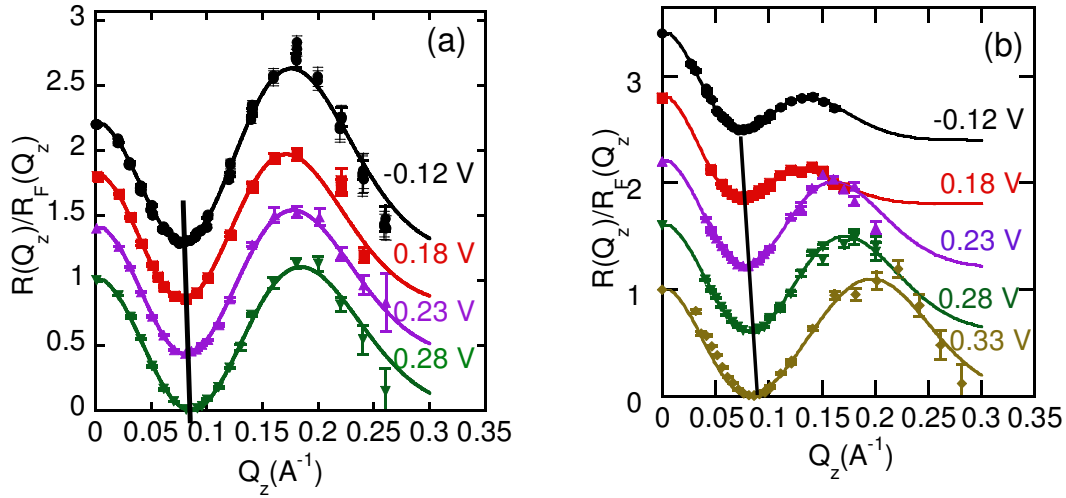
Figure 16. X-ray reflectivity normalized to Fresnel reflectivity $R(Q_z)/R_F(Q_z)$ for various electric potential differences $\Delta\phi^{w-o}$ as a function of wave vector transfer Q_z from liquid-liquid interfaces between (a) 3 µM or (b) 12.5 µM SOPC + 5 mM TDATPBCl in DCE and 0.1 M NaCl + 20 mM HEPES in water. The experiments were carried out at $T \approx 23\,°C$. Curves are ordered from bottom to top with decreasing $\Delta\phi^{w-o}$ and are successively displaced upwards for clarity (note that $R(Q_z)/R_F(Q_z) \rightarrow 1$ as $Q_z \rightarrow 0$ for each separate reflectivity curve). Values at $Q_z = 0$ are measurements of the direct beam when the interface is moved out of the beam path. When $\Delta\phi^{w-o} < 0.18$ V, the reflectivity curves for $\Delta\phi^{w-o}$ = -0.15 V, -0.12 V, -0.07 V, -0.02 V, 0.03 V, 0.08 V, 0.13 V are indistinguishable as shown by overlapping data sets for these different values of $\Delta\phi^{w-o}$ in panel (a). A similar effect was observed for the 12.5 µM sample whose data is in panel (b), but only the -0.12 V data are shown. The two nearly vertical straight lines illustrate the variation in position of the first minimum. The fits are described in the text.

The data shown in Figure 16 are the result of measurements that span eight orders of magnitude for each curve, from $R(Q_z) = 1$ to $R(Q_z) \approx 10^{-8}$. The different range of Q_z for different curves is due to different values of interfacial tension and, consequently, roughness. For example, the smaller range of Q_z for the reflectivity measured for $\Delta\phi^{w-o}$ = -0.12 V in Figure 16b is due to the reduction in reflectivity at larger Q_z that occurs for large interfacial roughness. Measurements to larger values of Q_z were generally not possible because the additional time required for the measurement produced radiation damage. Careful monitoring and reproduction of the data in Figure 16 ensured that radiation damage was negligible.

3.3.4   X-ray Data Analysis

X-ray reflectivity data are fit to determine the arrangement of SOPC lipid molecules at the interface. A 1-slab model that describes the interface as a single slab of thickness L and homogeneous electron density sandwiched between the bulk aqueous and DCE electrolyte solutions could not fit the data in Figure 16. A 2-slab model provided a good fit to all the data. This model provides a sensible correspondence between each slab and the SOPC headgroups or tailgroups. It is well known that the applied electric potential difference $\Delta\phi^{w-o}$ establishes an interfacial ion distribution consisting of supporting electrolytes.[81] Therefore, we expect that, in addition to the monolayer of lipid molecules at the interface there should be a distribution of ions on either side of the lipid layer, which decays from a value near the lipid layer to the bulk ion concentration. Closely matched X-ray contrast of the ions and solvents produces an ion distribution that has a negligible effect on the interfacial electron density profile. This was confirmed by X-ray reflectivity measurements from samples containing only the electrolyte solutions, *i.e.*, without lipids. These X-ray reflectivity data, measured for $0 \le \Delta\phi^{w-o} \le 0.33$ V , could be fit with a simple interface consisting of a step function intrinsic electron density profile roughened by capillary waves,[29] thus demonstrating the negligible effect of supporting electrolytes on the electron density probed by X-ray reflectivity measurements shown in Appendix B.

The 2-slab model of the electron density profile $\langle \rho(z) \rangle$ contains the sum of three error functions (erf), each of which models the changing electron density through an internal interface (water/headgroup, headgroup/tailgroup, and tailgroup/DCE) within the DCE/SOPC-monolayer/water interfacial structure,

$$
\begin{aligned}
\langle \rho(z) \rangle = & \frac{1}{2}(\rho_h - \rho_w) \, erf\left(\frac{z}{\sqrt{2}\sigma}\right) + \frac{1}{2}(\rho_t - \rho_h) \, erf\left(\frac{z-L_h}{\sqrt{2}\sigma}\right) + \\
& \frac{1}{2}(\rho_{DCE} - \rho_t) \, erf\left(\frac{z-L_h-L_t}{\sqrt{2}\sigma}\right) + \frac{1}{2}(\rho_{DCE} + \rho_w)
\end{aligned}
\tag{3.12}
$$

The electron densities ρ represent the average electron density in the interfacial region of the SOPC headgroups, ρ_h, and tailgroups, ρ_t, and of the bulk aqueous (water), ρ_w, and DCE, ρ_{DCE}, phases. The thicknesses of the slabs that correspond to the SOPC headgroup and tailgroup regions are represented by $L_{h,t}$. The interfacial roughness σ represents the effect on the electron density profile of thermal fluctuations of the interface.[29]

Binyang Hou[52] wrote that, "the X-ray reflectivity is calculated from $\langle \rho(z) \rangle$ by use of the Parratt algorithm in which the electron density profile $\langle \rho(z) \rangle$ is divided into several hundred layers along the z-axis (with a layer spacing of 0.2 Å in the interfacial region) to model the continuously varying density".[28] In this thesis, the electron density profile is divided into 300 layers. The calculated reflectivity is used to fit the data in Figure 16 by non-linear least squares fitting of the parameters ρ_h, ρ_t, L_t, and the total thickness $L = L_t + L_h$. In addition, a small offset in Q_z, ~1 x 10^{-3} Å^{-1}, is fit to the data to account for a slight misalignment of the reflectometer. The other three parameters in Eq.(3.12), ρ_w, ρ_{DCE}, and σ, are calculated.

The bulk electron densities ρ_w and ρ_{DCE} are calculated using $\rho_s + \sum_{i=1}^{4} n_i (N_i - V_i \rho_s)$, where ρ_s represents the electron density of the pure solvent (water or DCE), n_i is the number density of ion i of the supporting electrolytes, and N_i and V_i are number of electrons and volume of ion i. The electrolytes dissociate into TDA$^+$, TPBCl$^-$, Na$^+$, and Cl$^-$ ions, which do not cross the interface to any appreciable extent for the values of $\Delta\phi^{w-o}$ studied, as illustrated by the cyclic voltammogram in Figure 13. The volumes of Na$^+$ and Cl$^-$, respectively 3.82 Å^3 and 24.82 Å^3, are calculated from their spherical diameters: 1.94 Å for Na$^+$ and 3.60 Å for Cl$^-$.[82] The volumes of TDA$^+$ and TPBCl$^-$, respectively 1219.02 Å^3 and 531.32 Å^3, are calculated as solvent excluded volumes using Gaussian03.[83] This yields the bulk electron densities of the DCE and aqueous phases to be 0.3795 e Å^{-3} and 0.3344 e Å^{-3}. The value for the critical wave vector for total reflection $Q_c = 0.00795$ Å^{-1} determined by these densities is consistent with the X-ray reflectivity data.[29]

The interfacial roughness σ is calculated from the measured interfacial tension γ and capillary wave theory, $\sigma^2 = (k_B T / 2\pi\gamma) \ln(q_{max} / q_{min})$, where T is the temperature, $q_{max} = 2/r = 2\sqrt{\pi/A}$ is the cutoff for the smallest wavelength capillary waves that uses r as the effective cross-sectional radius, A is the area per lipid, and q_{min} is the smallest capillary wave vector that can be resolved by the X-ray measurements, given by $q_{min} = (2\pi/\lambda)\Delta\alpha_s \sin\alpha_i$ ($\Delta\alpha_s = l/d = 5.6 \times 10^{-4}$ is the vertical angular acceptance of the detector, where $l = 1.8$ mm is the electronic slit size and $d = 3.19$ mm is the distance from the sample center to the CCD detector).[29]

Table 3 lists the calculated values of σ and fitting parameters for the best fits of the X-ray reflectivity data shown in Figure 16.

Table 3. Parameters for 2-slab model fitting to X-ray reflectivity measurements[a]

SOPC Concentration (μM)	$\Delta\phi^{w-o}$ (V)	L_h (Å)	ρ_h (e⁻ Å⁻³)	L_t (Å)	$L_{t\,min}$ (Å)	ρ_t (e⁻ Å⁻³)	σ (Å)	L (Å)
3	-0.12	$6.1^{\pm1.4}$	$0.411^{\pm0.037}$	$16^{\pm3}$	12.5	$0.321^{\pm0.009}$	$7.48^{+0.07/-0.58}$	$22.1^{\pm2.6}$
	0.18	$6.5^{\pm1.5}$	$0.415^{\pm0.039}$	$16^{\pm3}$	13.2	$0.323^{\pm0.011}$	$7.8^{+0.1/-0.6}$	$22.5^{\pm3.1}$
	0.23	$8.8^{\pm2.4}$	$0.402^{\pm0.029}$	$16^{\pm4}$	11.2	$0.339^{\pm0.012}$	$7.12^{+0.05/-0.56}$	$24.8^{\pm2.4}$
	0.28	$8.6^{\pm2.3}$	$0.399^{\pm0.025}$	$16^{\pm4}$	10.5	$0.341^{\pm0.009}$	$6.61^{+0.03/-0.37}$	$24.6^{\pm1.9}$
12.5	0.28	$9.1^{\pm2.9}$	$0.408^{\pm0.034}$	$15.2^{\pm4.5}$	10.5	$0.334^{\pm0.011}$	$7.7^{+0.07/-0.6}$	$24.3^{\pm2.7}$
	0.33	$8.7^{\pm3.1}$	$0.401^{\pm0.029}$	$15.1^{\pm5.1}$	7.85	$0.338^{\pm0.012}$	$6.84^{+0.06/-0.39}$	$23.8^{\pm2.3}$

[a] Four parameters are fit to the X-ray reflectivity data: electron densities ρ_h and ρ_t of slabs that include the SOPC headgroups and tailgroups plus intercalated solvents, total thickness $L = L_t + L_h$ of the SOPC monolayer, and thickness L_t of the lipid tailgroup slab. The headgroup slab thickness L_h is calculated from L and L_t. A lower limit $L_{t\,min} = 950/A$ is imposed when fitting the SOPC tailgroup layer thickness, which does not affect the fitted values but only influences the "-" error bar. Similarly $L - L_t = L_h$ is restricted to lie between 5 and 12 Å. A conservative estimate for $L_{t\,min}$ is given by the volume occupied by the SOPC tailgroup V_t (ignoring possible solvent intercalated into the tailgroup region) divided by the area per lipid A listed in Table 2. The value of 950 Å² in the expression for $L_{t\,min}$ is determined by the known value of the POPC tailgroup volume,[84,85] which has two fewer carbon atoms in each tail. The interfacial roughness σ is calculated from capillary wave theory, where the "+" error is due to measured errors on the interfacial tension and the "-" error is due to the possibility of a small interfacial bending rigidity, see Discussion. Fitting parameters for $\Delta\phi^{w-o} < 0.18$ V (-0.15 V, -0.12 V, -0.07 V, -0.02 V, 0.03 V, 0.08 V, 0.13 V) are essentially the same so the values for $\Delta\phi^{w-o} = -0.12$ V are given as representative values. Samples with 12.5 μM SOPC and $\Delta\phi^{w-o} < 0.28$ V exhibit roughness values larger than 8 Å, which produce X-ray reflectivity measurements with limited spatial resolution and consequently, large errors on the fit parameters. Fitting parameters for these values of $\Delta\phi^{w-o}$ are not shown, nevertheless, analysis of these samples yields parameters that agree within error bars with those for the 3 μM SOPC sample at the same values of $\Delta\phi^{w-o}$. The fitting program is listed in Appendix C.

3.3.5   MD Simulations
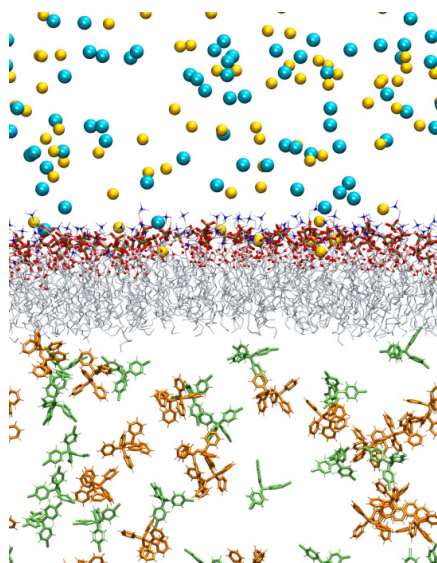
Figure 17. SOPC monolayer at the water (top)-DCE (bottom) interface in the top half of the simulated unit cell. The area per lipid molecule is 121 Å^2 and a 0.33 V electric potential difference is applied across the monolayer such that the water is at higher potential. The cations (Na+, BTPPA+) in their respective solvents are colored dark blue and the anions (Cl-, TPBCl-) are yellow. Solvents are not shown for clarity.

Figure 17 illustrates the top half of the simulation cell for one of the systems listed in Table 1. The monolayer resides in the *x-y* plane. The simulated areas per lipid are chosen from experimental values and fixed by the *x-y* dimensions of the simulation cell, which remain constant throughout the simulation (see Table 1 for a description of the five different simulation cells). An electric field along the *z* -axis is applied to every charge in the simulation cell. Figure 18 shows the profile of the electric potential difference along the *z* -axis calculated using the simulated charge density and Poisson's equation for the five systems listed in Table 1 as shown in 0.[86] An electric potential difference across the lipid monolayer is present even in the absence of an applied electric

field, as illustrated in Figure 18, as a result of, for example, the potential drop across the interfacial region that

contains partially oriented headgroup dipoles (represented by the jagged peaks at $z \approx 100$ Å). The potential

difference simulated for zero applied electric field $\Delta\phi_{s,0}$ is taken as the reference potential difference to

determine the simulated electric potential difference between the water and oil (DCE) phases,

$\Delta\phi_s^{w-o} = \Delta\phi_{s,0} - \Delta\phi_s$, where $\Delta\phi_s$ is the simulated electric potential difference for non-zero applied electric field

(Figure 18). This reference potential difference is comparable to the experimental reference $\Delta\phi_{pzc}^{w-o}$, discussed in

Section 3.2.3, that corresponds to a sample for which the ion distribution $c_i(z)$ is constant as z varies from the

interface to the bulk, in the absence of lipids.
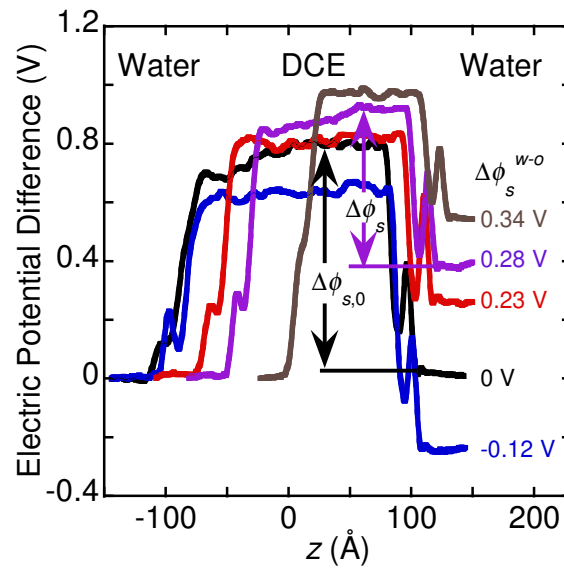
Figure 18. Simulated electric potential difference profiles. Simulation cell consists of water/DCE/water electrolyte solutions with a lipid monolayer at each interface. The simulated electric potential difference between the water and DCE phases in the absence of applied electric field is shown by $\Delta\phi_{s,0}$. The electric potential difference in the presence of electric fields is shown by one value of $\Delta\phi_s$.

The simulated SOPC lipid monolayer is further characterized by calculating its thickness L_s and orientation angles α of the SOPC headgroup and β of the entire SOPC molecule, where the angles are illustrated in Figure 19.[87] Average values of these parameters are calculated by averaging over all 100 lipids in the monolayer, then further averaging over the 500 simulation frames that span the last 4 ns of each simulation trajectory. The thickness L_s is the difference between the maximum and minimum z coordinate of each lipid. Table 4 shows that the membrane thins with increasingly positive electric fields. Constancy of the length along the first principle axis of the SOPC, shown by values of $L_{s,SOPC} = L_s / \cos\beta$ listed in Table 4, indicates that the variation in membrane thickness is due to tilting of the entire SOPC molecule and not due to changes in the configuration of the molecules.

Table 4. Angular orientation and thickness of simulated SOPC monolayers[a]

$\Delta\phi_s^{w-o}$ (V)	L_s (Å)	$L_{s,SOPC}$	α (°)	β (°)
-0.12	23.7 ± 0.2	24.8 ± 0.2	65.6 ± 1.8	17.4 ± 0.8
0	23.8 ± 0.2	25.0 ± 0.2	66.7 ± 1.3	18.1 ± 0.8
0.23	23.1 ± 0.2	24.8 ± 0.3	67.6 ± 1.8	21.1 ± 1.1
0.28	22.3 ± 0.2	24.7 ± 0.4	69.1 ± 2.2	25.6 ± 1.7
0.33	21.6 ± 0.2	24.9 ± 0.4	74.1 ± 2.9	30.0 ± 1.4

[a]Angles α and β denote the tilt angle of the SOPC headgroup and entire SOPC molecule measured from the z-axis (Figure 19), L_s represents the simulated thickness of the lipid monolayer, and the calculated value $L_{s,SOPC} = L_s / \cos\beta$ is the simulated total length of SOPC molecules.
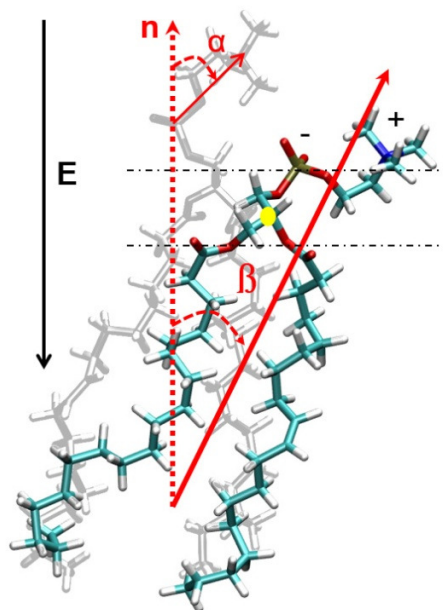
Figure 19. Simulated tilt angles of SOPC. Faded image shows the headgroup tilt angle α measured between the z-axis and a line connecting P to N atoms in the headgroup. The entire SOPC tilt angle β is measured between the first principle axis of the lipid molecule and the z-axis. The faded image illustrates a typical SOPC orientation in zero applied electric field (fixed area per lipid of 72 $\AA^2$) and the normal image illustrates a typical SOPC orientation in a large electric field (E = 0.08999 kcal mol^{-1} $\AA^{-1}$ e^{-1} with fixed area per lipid of 121 $\AA^2$). The dashed lines show the boundaries where a small force (f= 0.2 kcal/mol/$\AA$) is applied on the C2 carbon (yellow dot) in each lipid. The force can prevent C2 carbons from passing the boundary.

Figure 20 illustrates the electron density profiles calculated from MD simulations for the five systems. They exhibit a peak of higher electron density corresponding to the interfacial region containing SOPC headgroups and a lower electron density region corresponding to the SOPC tailgroups. The thinning of the lipid monolayer, previously discussed is clearly observable. Comparison with experimental results will be presented in the Discussion section.
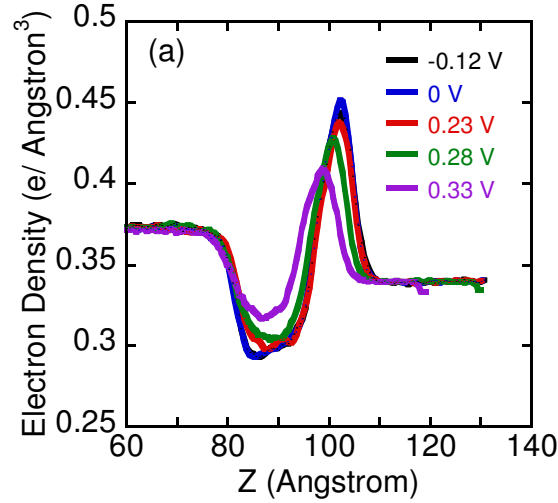
Figure 20. Electron density profile calculated from MD simulations.

3.4   Discussion

In this section the experimental and MD simulation characterizations of the lipid monolayer structure under conditions of different electric fields are compared.

3.4.1   Electron Density Profile

X-ray reflectivity measurements of the SOPC monolayer were analyzed in terms of an intrinsic electron density profile roughened by thermal capillary waves. The intrinsic electron density profile is characterized by the 2-slab model (Eq.(3.12)) when the roughness parameter σ is set to zero. The full experimental electron density profile probed by the X-ray reflectivity is given by the 2-slab model with the best-fit parameters listed in Table 3, including the roughness σ whose effect is to smear the profile along the z-axis. Neither of these electron density profiles can be compared directly to the profile from MD simulations shown in Figure 20 because the small cross-sectional dimensions of the simulation cell (e.g. 85 x 85 Å^2) limit the capillary wave roughness to a small, but non-zero value, 3.2 Å, whereas the experimental value of roughness is close to 7 Å.

Figure 21 illustrates a comparison between the full experimental electron density profiles and modified MD simulated electron density profiles. The simulated profiles were modified by fitting the simulated profiles with the 2-slab model, then substituting roughness values from experiment. The two sets of profiles are qualitatively similar, though there are some quantitative differences. The total monolayer thicknesses are slightly larger for the simulations, as discussed later, though the trend towards thinning with increasingly positive electric potential difference is observed in both sets of profiles. The simulated electron density value is smaller in the tailgroup minimum by about 0.01 e$^-$Å^{-3} and larger in the headgroup maximum by a similar amount. Similar discrepancies between experimental and simulated values are noted in the electron densities of the bulk DCE and water phases.
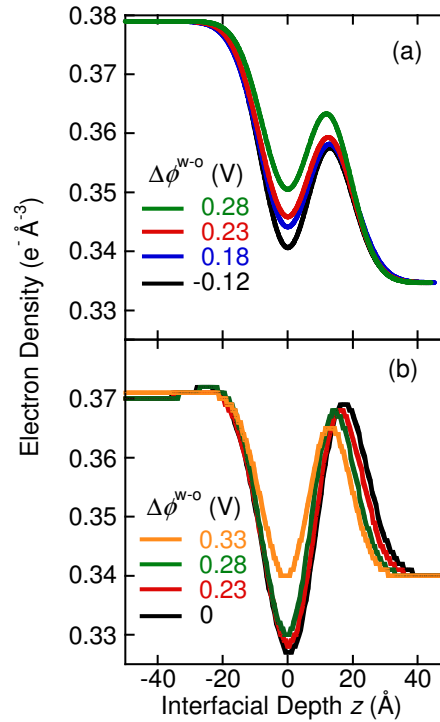
Figure 21. Fitted electron density profiles from (a) X-ray reflectivity and (b) MD simulations, whose values of thermal capillary wave roughness are matched at a similar value of electric potential difference. The electron density profile in (b) is calculated as described in 1.a.i.Appendix C.

Tailgroup Region Close-packed saturated alkyl chains have electron densities that vary from 0.325 to 0.343 $e^- Å^{-3}$ for alkane rotator phases to crystalline bulk phases of long chain alkanols.[88] Such close-packed chains have a cross-sectional area of ~19 $Å^2$ that is much smaller than half the 73 $Å^2$ per lipid or greater interfacial area that is occupied by the disordered monolayer of two-tailed SOPC. The unsaturated oleoyl tail of SOPC frustrates the chain packing, forcing it to occupy a larger interfacial area than close-packed chains. Therefore, even though values of the intrinsic electron density ρ_t of the tailgroup slab, determined by X-ray reflectivity, vary from 0.32 $e^- Å^{-3}$ to 0.34 $e^- Å^{-3}$, they cannot represent close-packed tailgroups. Instead, this high electron density is the result of DCE molecules, with an average density of 0.38 $e^- Å^{-3}$, intercalating into the region of the tailgroups. As $\Delta\phi^{w-o}$ increases, the area per lipid increases, thus allowing for greater intercalation

of the DCE and an increase in electron density. Figure 22 shows that the trend in electron density with $\Delta\phi^{w-o}$ is

consistent with MD simulations. The number of DCE in the tailgroup region can be estimated based on the

electron density of the tailgroup. If the volume of the tail group is 960 Å^3, then 4, 6, or 9 DCE molecules are

needed to reach electron density values of 0.32, 0.33, or 0.34 e$^-$ Å^{-3}, respectively. Therefore, there are about 4

DCE molecules in the tailgroup region when $\Delta\phi^{w-o}$ is less than 0.2 V, and 9 DCE molecules at higher potential.

In the simulation, the number of DCE in the tail group region is 2, 3, and 6 for $\Delta\phi^{w-o}$ less than 0.23 V, 0.28 V,

and 0.33 V, respectively. This is consistent with the electron densities shown in Figure 22.
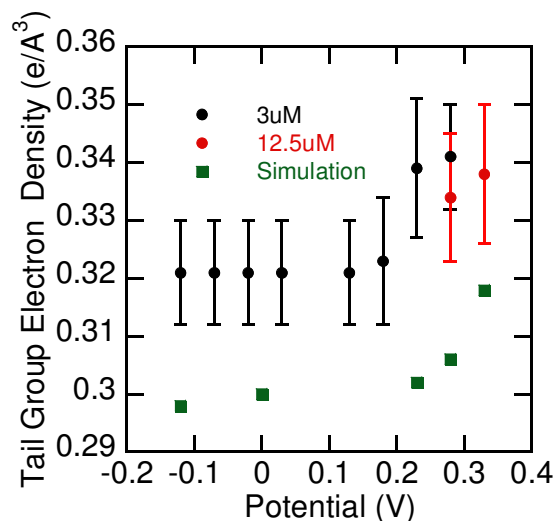
Figure 22. Comparison of the intrinsic electron density of the interfacial tailgroup slab determined by fitting X-ray reflectivity measurements (Table 3) and MD simulations.

The disordered nature of SOPC tailgroups is consistent with the 15 Å to 16 Å thickness of the tailgroup

slab determined by X-ray reflectivity (Table 3). An all-trans alkyl chain with 17 carbon atoms will have a length

of 21.5 Å (= (17-1+9/8)*1.265 Å)[89], which is much more than the measured thickness of the tailgroup slab.

Headgroup Region The thickness of the SOPC head group region of 7.5 Å to 8.5 Å (Table 3) is consistent with literature values of PC lipid headgroup thicknesses in monolayers on liquid surfaces that vary from 7 Å to 12 Å.[90] Similarly, the measured headgroup electron density of 0.399 e⁻ Å⁻³ to 0.415 e⁻ Å⁻³ lies within the range of values previously observed.[90] Note that measurements of the volume of the PC headgroup of ~320 Å³ yield an electron density of 0.53 e⁻ Å⁻³.[84,85,91] As expected, substantial hydration of the headgroup is required to reduce its electron density to the measured values. By assuming the thickness of the SOPC head group region thickness to be 8.5 Å, 15 water molecules are needed to lower the electron density to 0.415 e⁻ Å⁻³ and 20 to 0.399 e⁻ Å⁻³. In the simulation, about 12, 14, 15, 19 water molecules are found for $\Delta\phi^{w-o}$ less than 0.23 V, 0.23V, 0.28 V, 0.33 V, respectively. The simulation agrees well with the experiment.

3.4.2 Bending Rigidity

The fluctuation spectrum of lamellar lipid bilayer phases is known to be influenced by the bending rigidity (or modulus) κ.[92] Similarly, the roughness σ of an interface is influenced by κ, which preferentially suppresses short wavelength thermal fluctuations of the interface, as observed from the expression for the energy $u(\vec{q}_{xy})$ per capillary mode with wave vector $\vec{q}_{xy}$,[29]

$$u(\vec{q}_{xy}) \approx \frac{\left|h(\vec{q}_{xy})\right|^2}{2A_{tot}}[\Delta\rho_m g + \gamma\left|\vec{q}_{xy}\right|^2 + \kappa\left|\vec{q}_{xy}\right|^4 + ...] \qquad (3.13)$$

where $h(\vec{q}_{xy})$ is the Fourier transform of the surface height function, A_{tot} is the total surface area, $\Delta\rho_m$ is the mass density difference between the two phases, and g is the gravitational acceleration. The surface bending rigidity κ is the amplitude of the $\left|\vec{q}_{xy}\right|^4$ term, which is large at short wavelength capillary waves. The expression in Eq. (3.13) leads to a revised expression for the interfacial roughness σ,[93]

$$\sigma^2 \approx \frac{k_B T}{2\pi\gamma}\ln\frac{(\gamma/\kappa)^{1/2}}{q_{min}} \qquad (3.14)$$

where the value of q_{min} was given in Section 3.3.4. X-ray reflectivity measurements probe the spatially averaged (over the *x-y* plane of the interface) fluctuation spectrum to yield the interfacial roughness σ, but cannot

separate the effects of tension γ and surface bending rigidity κ. Our QELS measurements also probe the

thermal fluctuation spectrum, but do so at much longer capillary wavelengths ($\sim 8.5 \times 10^{-5}$ m), thus allowing for a

measurement of γ that is unaffected by small values of κ. The analysis of X-ray reflectivity presented in

Section 3.3.4 used the value of roughness $\sigma^2 = (k_B T / 2\pi\gamma) \ln(q_{max} / q_{min})$ determined by the QELS measurement

of γ. Re-analysis of X-ray reflectivity data with the smaller roughness given by Eq.(3.14) can place an upper

limit on values of κ that fit the data. The 12.5 µM SOPC sample provides the most sensitive conditions because

it exhibits the lowest tension values (Figure 14). Since the surface bending rigidity is known to be maximized at

the highest interfacial density of lipids[94], re-analysis of the reflectivity data for the 12.5 µM SOPC sample at

$\Delta\phi^{w-o}$ = -0.12 V provides an upper limit $\kappa \leq 1.5 \, k_B T$. Under these conditions the interfacial roughness σ

decreases from a value of 12 Å when $\kappa = 0$ to 10.5 Å when $\kappa = 1.5 \, k_B T$. The lower error bar on σ listed in

Table 3 shows the variation in σ due to the value of $\kappa = 1.5 \, k_B T$ for other sample conditions.

3.4.3   Total Monolayer Thickness

The values of monolayer thickness L determined from X-ray measurements (listed in Table 3) and

values of L_s from the MD simulations (listed in Table 4) are very similar, ~22 to 25 Å, depending upon the

interfacial area per lipid. One complication arises in the further comparison of these values to determine the

variation of monolayer thickness with electric potential difference $\Delta\phi^{w-o}$. As shown in Table 3, the fitted values

of L have one standard deviation errors up to ±3 Å; nevertheless, the electron density profiles that are produced

by sets of fit parameters that vary within one standard deviation of the best-fit parameters are indistinguishable

from the best-fit electron density profiles shown in Figure 21. This shows that the electron density profile is

accurately determined by the X-ray measurements, but that correlations among the fitting parameters yield

unphysically large variations. This complication is multiplied by the inability to directly measure the bending

rigidity described in the previous section. Varying the bending rigidity from the minimum to maximum values (0

to 1.5 $k_B T$) yields an additional variation in of ~3 Å in the fitting parameter L, without changing the electron

density profile. This problem can be circumvented by directly analyzing the electron density profiles.

Figure 23 shows the 10-90 thickness of the SOPC monolayer, calculated by analysis of the electron density profiles in Figure 21a to determine the largest distance between positions z where the density is less than the DCE bulk phase density by 10% and 90% of the density difference between the two bulk phases. Partially as a result of the thermal roughness of the interface, the 10-90 thicknesses are artificially larger than the true length of SOPC. Nevertheless, the advantage of this measure is that it can be compared to the same measure of thickness calculated from the roughened MD simulation profiles shown in Figure 21b. Figure 23 demonstrates that the 10-90 thicknesses are about 5 Å larger for the simulations, as is confirmed by visual observation of the two panels in Figure 21. Also observable from both experiment and simulation is the thinning of the monolayer at about the same values of $\Delta\phi^{w-o}$, although a larger effect is observed in the simulations.
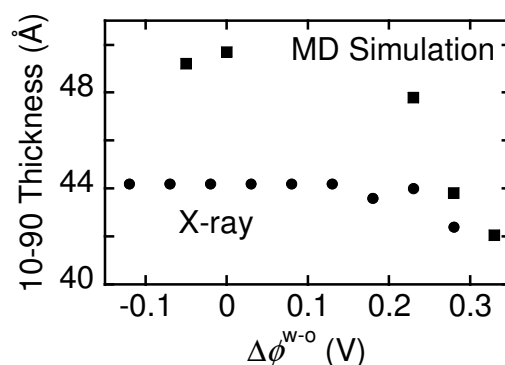
Figure 23. 10-90 monolayer thickness determined by analysis of the electron density profiles shown in Figure 21 from X-ray reflectivity (3 µM SOPC sample – dots) and MD simulations (squares). This measure of monolayer thickness includes the effect of thermal roughness.

3.5   Conclusion

The effect of membrane potential on the molecular ordering of lipids within a biomimetic membrane, a self-assembled monolayer of SOPC lipids at an electrified liquid-liquid interface, is studied with X-ray reflectivity measurements, interfacial tension measurements, and MD simulations. The electric potential

difference $\Delta\phi^{w-o}$ is applied at a liquid-liquid interface between two immiscible electrolyte solutions. Closely matched X-ray contrast of the ions and solvents produces an ion distribution that has a negligible effect on the interfacial electron density profile, thus allowing for a simpler analysis of the structure of the lipid monolayer from X-ray measurements.

Interfacial tension and X-ray reflectivity measurements demonstrate that stable and reproducible SOPC monolayers are formed with surface densities that can be varied from the high densities typical of unsaturated lipids in biomembranes (~ 70 $\mathring{A}^2$ per lipid molecule) to densities lower by about a factor of two. The measurements of higher density SOPC monolayers are nearly indistinguishable over a biologically relevant range of electric potential differences, -0.15 V $\le \Delta\phi^{w-o} \le 0.13$ V , indicating that the structure of the SOPC layer is essentially constant over this range of $\Delta\phi^{w-o}$. The X-ray reflectivity measurements determined values of the thickness and electron densities of the two layers that correspond to the SOPC headgroups and tailgroups, which are consistent with values in the literature for layers of unsaturated lipids in other geometries, such as bilayer vesicles or Langmuir monolayers. Measurements at higher positive potentials, up to 0.33 V, illustrate a monotonic increase in the interfacial area per lipid and accompanying variations in the interfacial configuration of the lipid.

MD simulations, designed to mimic the experimental conditions, confirm in atomistic detail the measured potential-dependent characteristics of SOPC monolayers. The variation of measured tailgroup electron density and monolayer thickness with $\Delta\phi^{w-o}$ is consistent with MD simulations. MD simulations of the length along the first principle axis of SOPC molecules indicates that the variation in membrane thickness is due to tilting of the entire SOPC molecule and not due to substantial changes in the configuration of the molecules, except possibly at the highest value of $\Delta\phi^{w-o} = 0.33$ V. This may be due to the larger area per lipid at these higher values of $\Delta\phi^{w-o}$ or it may be that rotation of the headgroup dipole by the electric field produces a rotation of the entire molecule, except at the highest simulated electric field. Ongoing simulations with the same area per lipid, but much lower electric fields indicate that the electric field has only a small effect on the configuration of SOPC molecules, except at the highest potentials. This is consistent with the approximate energy of the headgroup dipole in the electric field, $U = -\vec{p}\cdot\vec{E}$, which is calculated to be ~ $k_B T$ for a headgroup dipole

moment of 10 D and electric fields of ~ 10^8 V/m. The combination of simulations and experiments suggest that the primary effect on the SOPC configuration in the monolayer is due to the change in area per lipid that varies with $\Delta\phi^{w-o}$.

This study demonstrates a useful model system to create stable lipid layers subjected to a controlled range of biologically relevant electric potential differences. We anticipate using this model system in subsequent experiments to study electrostatic processes in biomimetic membranes.

Chapter 4

MODULATION OF PROTEIN-LIPID BINDING BY ELECTRIC FIELDS

4.1   Introduction

Protein translocation induced by peripheral membrane proteins between cellular compartments has been known as a very important mechanism for cell signaling and vesicle trafficking. This translocation between the peripheral membrane proteins and the peripheral regions of the lipid bilayer is believed to be achieved through one or more lipid binding domains.[10,95-100] The protein cytosolic phospholipase, cPLA2, a water-soluble lipase with a C2 domain on its N-terminal, catalyzes the release of arachidonic acid at the sn-2 position of some phospholipids to provide free arachidonic acid for the biosynthesis of eicosanoids.[101] It translocates from the cytosol to the nuclear membrane and endoplasmic reticulum with the increase of intracellular calcium, and the calcium-dependent behavior is due to the C2 domain.

C2 domains are important binding domains relevant for the membrane binding of many peripheral proteins. They were first identified as the second conserved domain of Ca^{2+}-dependent PKC isoforms.[97,98] Later, the presence of C2 domains in many other proteins is revealed,[99] and proteins with C2 domains are involved in many different cell functions.[12,14,102-105] The high-resolution structures of over ten C2 domains have been determined. These structures show that the C2 family shares a common fold consisting of an eight-stranded antiparallel β sandwich.

The membrane binding of peripheral proteins involves interactions that depend on the physicochemical properties of both membrane and protein. Extensive biophysical and structure-function studies have shown that the binding can be driven by a combination of electrostatic interactions, hydrophobic interactions, and complex interactions involving aromatic side chains.[95,96] The C2 domains in many cases have been characterized as membrane-docking modules triggered by calcium. Previous studies have revealed that the electrostatic mechanism of docking for most of the C2 domains are a Ca^{2+} induced electrostatic attraction for negative charged

phospholipids.[12,106,107] In contrast, cPLA2α-C2 represents a different group of C2 domains that bind to zwitterionic lipids.[10,99,102,104,105] Hydrophobic interactions have been shown to be largely responsible for the membrane binding of cPLA$_2$.[10,108] Calculations also show that electrostatic interactions alone do not explain cPLA$_2$α-C2 binding with zwitterionic lipids, but the increase in electrostatic potential near the binding site of cPLA2α-C2 reduces the desolvation penalty that accompanies membrane association and penetration.[11]

The interaction of peripheral membrane proteins in an aqueous solution with a monolayer of lipids at the interface is a good model for the behavior of these proteins.[109-111] Combined monolayer and cell studies have demonstrated the relevance of this model system.[11,101,106-108,112,113] In this paper, an electric field is applied to the SOPC monolayer to investigate the role of the electrostatic interactions on the binding of cPLA2α-C2 and SOPC monolayers.

4.2   Experimental Details

4.2.1   Materials

The unsaturated phospholipid 1-stearoyl-2-oleoyl-sn-glycero-3-phosphocholine (SOPC, $C_{44}H_{86}NO_8P$, CAS# 56421-10-4) was used as received from Avanti Lipids. The aqueous electrolytes, NaCl (Alfa Aesar Puratronic®, 99.999% metals basis), LiCl (certified ACS, crystal from Fisher Scientific Company) and CaCl$_2$ (ultra dry, 99.99% metals basis, Alfa Aesar) were roasted at 450 °C for 45 mins to remove organic contaminants and water. Water from a Nanopure UV Barnstead system was used to prepare aqueous alkali chloride solutions. HEPES buffer solution (1 M) was purchased from Fisher Scientific. 1,2-dichloroethane (DCE, CHROMASOLV, for HPLC, 99.8%) was purchased from Sigma Aldrich and purified by passing it six times through a column of water-saturated aluminum oxide (activated basic alumina). DCE was further filtered through a 0.2 μm Millipore filter (OMNIPORE membrane filter, PTFE) using a stainless steel pressure filter holder from Sartorius-Stedim Biotech (16249), to remove residual alumina. The organic electrolytes tetradodecylammonium tetrakis(4-chlorophenyl)borate (TDATPBCl) and tetradodecylammonium chloride (TDACl, >97%) were used as received from Aldrich. 1-hexadecanethiol (99%) was purchased from Sigma Aldrich and used as received. The expression and purification of the cPLA2α-C2 domain were previously described.[102] cPLA2α-C2 was dissolved in 100 mM NaCl, 20 mM HEPES, and 0.1mM CaCl$_2$ buffer solution, frozen by liquid nitrogen, and then stored at -20 ℃.

4.2.2   Liquid-Liquid Sample Cell
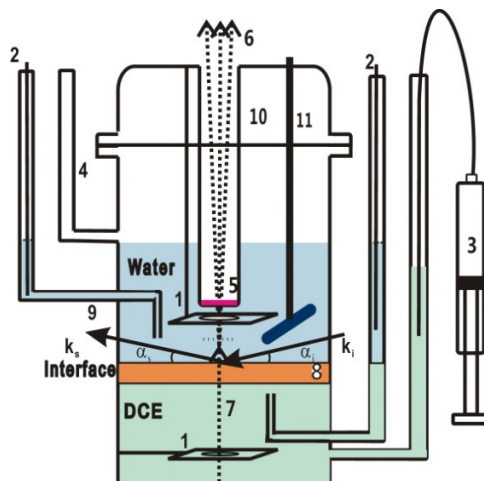
Figure 24. Schematic of four-electrode glass sample cell. (1) Counter electrodes (CE1,2, Pt mesh) (2) Reference electrodes in Luggin capillaries (RE1,2, Ag|AgCl) (3) Syringe to adjust volume of DCE phase in order to flatten the liquid-liquid interface (4) Pressure release valve (5) Optical grating for quasi-elastic light scattering (6) Laser beam diffracted by grating (7) Laser beam for quasi-elastic light scattering (8) Gold coated Mylar strip to pin the interface (9) X-rays (10) Tube with grating, which can be removed while keeping the rest of the top cap in place. A syringe can be placed through the hole formerly occupied by the glass tube in order to inject 20 mg/l cPLA2α-C2 solution (11) Glass propeller for stirring

The four-electrode glass electrochemical sample cell is shown as Figure 24. In combination with a Solartron 1287 potentiostat, this sample cell provides precise control and measurement of the electrical current and potential difference across the interface between two immiscible electrolyte solutions, ITIES, as well as the ability to monitor the interfacial tension during measurements of X-ray reflectivity from the liquid-liquid interface. All experimental measurements in this paper used this sample cell that has a flat water-DCE interface with an area of about 38 cm^2. The galvanic cell can be represented by the scheme:

Ag|AgCl|100 mM NaCl +20 mM HEPES (H$_2$O)+0.1mM CaCl$_2$+6mg/l cPLA2α-C2 ‖5 mM TDATPBCl + 3μM

SOPC (DCE)|10 mM LiCl + saturated TDACl (H$_2$O)|AgCl|Ag
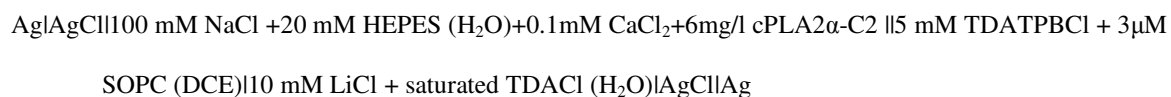
The solutions are electrically conductive as a result of dissolving electrolytes (e.g., NaCl, LiCl, TDATPBCl, and TDACl) into the solutions, therefore the response of cPLA2α-C2 (bound to the lipid monolayer) to different electric potential differences across the interface can be investigated. We adopt the rational potential scale[53,54] that approximates the electric potential difference $\Delta\phi^{w-o} = \phi^{water} - \phi^{oil}$ between the aqueous and organic bulk phases (far from interfaces and electrodes) as $\Delta\phi^{w-o} = \Delta\phi_{cell}^{w-o} - \Delta\phi_{pzc}^{w-o}$, where the potential of zero charge, $\Delta\phi_{pzc}^{w-o} = 0.167 \text{ V}$, is determined from the apex of the electrocapillary curve for the supporting electrolytes (as described in Chapter 3).

The sample without protein is made following the procedures described in Chapter 3. Prior to adding the protein to the sample, X-ray reflectivity is measured at the potential of zero charge to check that the SOPC monolayer was formed properly. The protein solution, consisting of 100 mM NaCl, 20 mM HEPES, and 0.1 mM $CaCl_2$ buffer solution with 20 mg/l cPLA2α-C2, is removed from the freezer and allowed to equilibrate slowly to room temperature. The protein solution is then filtered through a 0.2 μm Corning Syringe filter with a diameter of 25 mm. Afterwards, the filter is rinsed by 10 ml water solution (100 mM NaCl, 20 mM HEPES, and 0.1 mM $CaCl_2$) 3 times to collect the protein. This 30 ml of protein solution is injected by a syringe inserted through a hole in the top of the sample cell (Figure 24) into the aqueous phase (~70 ml volume prior to injection) while holding the electric potential difference at the potential of zero charge. During this process the aqueous phase is stirred gently with a 1.5 cm long glass propeller shown in Figure 24. The stirring is continued for ~30 to 50 minutes while measuring interfacial tension with a custom Quasi-Elastic Light Scattering (QELS) apparatus described in Chapter 3. The interfacial tension decreases from 10.2 mN/m to 7.6 mN/m as the protein binds to the SOPC monolayer. X-ray reflectivity measurements are started once the interfacial tension stabilizes.

4.3   Experimental Data Analysis

4.3.1   Interfacial Tension Measurement

The change in interfacial tension after cPLA2α-C2 is injected into the sample cell is shown in Figure 25, which indicates that cPLA2α-C2 went to the interface, presumably to bind to the SOPC monolayer. The interfacial tension of the pure SOPC monolayer was taken prior to X-ray exposure, though it agrees with other

measurements taken during X-ray reflectivity measurements. The interfacial tension after adsorption of cPLA2α-

C2 was measured during the measurement of X-ray reflectivity.
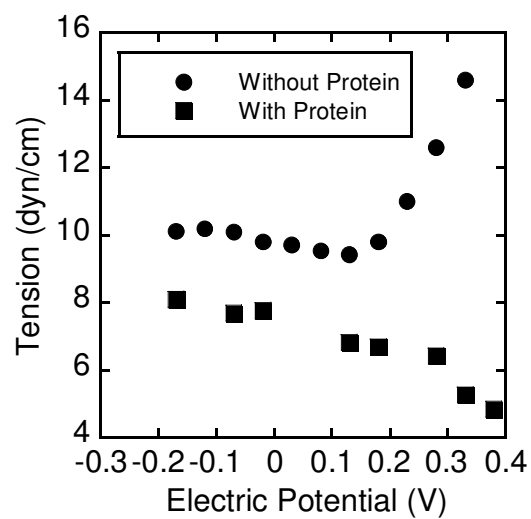
Figure 25. Potential dependence of the interfacial tension with and without cPLA2α-C2 in the aqueous phase. The measurements were made on separate samples.
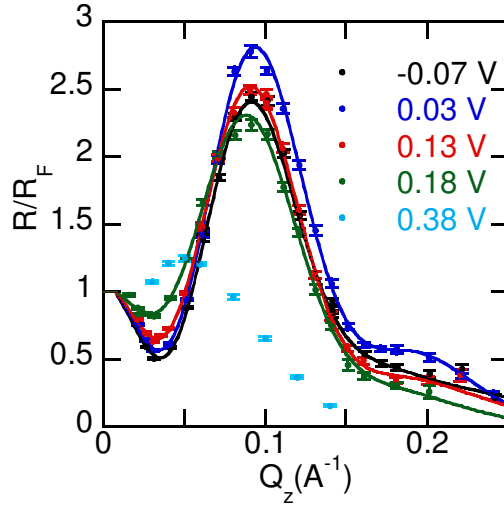
Figure 26. X-ray reflectivity (normalized to the Fresnel reflectivity) as a function of the wave vector normal to the interface between 3 μM SOPC + 5 mM TDATPBCl in DCE and 0.1 M NaCl + 20 mM HEPES + 0.1 mM CaCl$_2$ + 6 mg/l cPLA2α-C2 in water. The data point at Q_z =0 represents the intensity of the incident beam that passes through water phase above the interface without reflection. All the curves are fitted to two slabs plus protein model.

4.3.2   X-ray Reflectivity Data

X-ray reflectivity curves from cPLA2α-C2 domains bound to an SOPC monolayer under different $\Delta\phi^{w-o}$ are shown in Figure 26. Based on the study of SOPC monolayers presented in Chapter 3, the area per lipid of the monolayer is essentially unchanged for values of $\Delta\phi^{w-o}$ between -0.07 V and 0.18 V, thus the SOPC lipid monolayer can provide a stable base for cPLA2α-C2 over this potential range. Measurements for different values of $\Delta\phi^{w-o}$ were repeated at least once on different samples and the data points averaged. A much higher potential difference $\Delta\phi^{w-o}$ =0.38 V was also measured. The reflectivity measurements at 0.38 V vary by 20 to 30 % , which may due to an instability of the lipid monolayer at this high value of $\Delta\phi^{w-o}$. In this thesis, the analysis on high potential will provide only qualitative comparison with low potential ones.

The method of analysis used to fit the X-ray reflectivity curves in this paper was described previously.[12]

In this methodology, the lipid monolayer is in the *x-y* plane and the *z*-axis is perpendicular to the monolayer. Two slabs of uniform electron density represent the two layers containing separately the head groups and tail groups of the SOPC monolayer.[12,14] The electron density profile derived from the crystallographic structure of cPLA2α-C2 is utilized to model the protein. This procedure assumes that the structure of cPLA2α-C2 in solution and upon binding to the lipid layer is similar to the crystallographic structure. Although some changes are expected in the more flexible regions of the protein, it has been previously demonstrated that the overall structure is robust.[14,114]
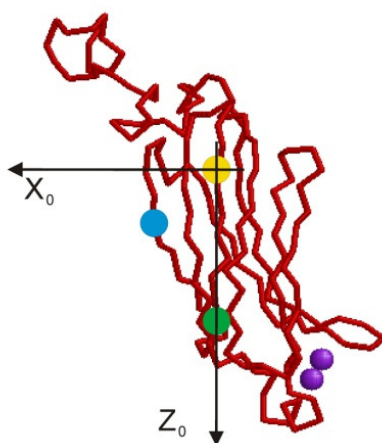
Figure 27. Crystal structure of cPLA2α-C2 protein domain with three reference atoms shown. The coordination system to describe the protein rotation is defined by α-carbons in residues F20 (yellow), A27 (Green) and K118 (Blue).[14]
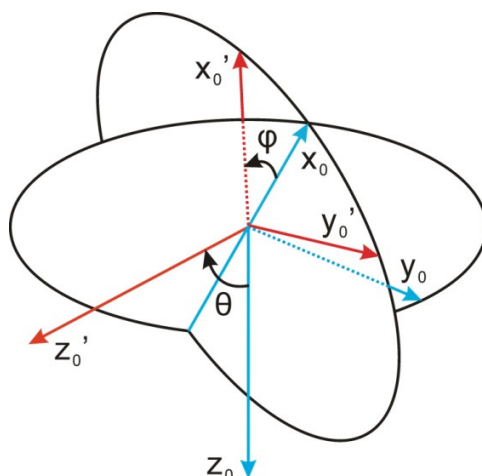
Figure 28. Rotation diagram for cPLA2α-C2 protein coordination system. Two Euler angles, θ and φ, is used to describe the rotation of the cPLA2α-C2 protein.[12] The angle θ measures the angle between the protein's z_0 axis and z_0' rotating about x_0 axis, and the angle φ is the angle between x_0 axis and x_0' axis and represents an azimuthal rotation about the direction of the z_0' axis.

To utilize the crystallography structure of cPLA2α-C2, a coordination system is built to quantitatively rotate the protein and calculate the electron density profile of the protein in each orientation. In previous studies on cPLA2α-C2,[14,102] the three α-carbon atoms of residues F20, A27, and K118 were chosen to establish the coordinate system to describe the orientation of cPLA2α-C2. The same coordinate system is used in this paper to allow a direct comparison of our X-ray reflectivity data from the liquid-liquid interface to X-ray reflectivity data from the liquid-air interface, and to electron paramagnetic resonance (EPR) measurements.[14,102,115] As shown in Figure 27, two α-carbons atoms, F20, A27, are located in the longest β-strand of the domain and the third carbon atom is located in the furthest strand in the same plate. Residue A27 is set to the origin of the coordination system, the z_0 axis of the protein extends from A27 to F20, the x_0-axis is in the plane established by A27, F20, K118 and perpendicular to z_0 axis, and the y_0 axis is defined by right-hand rule. The angle θ measures the angle between the protein's z_0 axis and z_0' rotating about the x_0 axis, and the angle φ is an azimuthal rotation about the direction of the z_0' axis axis shown in Figure 28.

The values chosen to fit φ to the X-ray data are initially spaced by 5° over the range from 0° to 180°

and values of θ are initially spaced by 20° over the range from 0 to 360°. Ultimately, a finer resolution was chosen for values of φ, spaced by 2 degrees over the range from 60° to 120°, and for values of θ, spaced by 5° over the range from 220° to 320°, near the best-fit configuration. For each orientation, the smallest rectangle box of the protein with sides parallel to the x, y and z axes was built to calculate the electron density over the x-y plane with spacing 0.5 Å in the z direction.[116] Eight parameters (COV, ρ_h, ρ_t, L_t, L_h, d_p, θ, φ) are used to define the model of the electron density profile of the system described as:

$$\rho_i(z) = COV \times \rho_{bpD}(z_p) + (1-COV)\rho_{DCE} \text{ for } z > 0 \qquad (4.1)$$

$$\rho_i(z) = COV \times \rho_{ep}(z_p) + \rho_t \text{ for } -L_t \leq z \leq 0 \qquad (4.2)$$

$$\rho_i(z) = COV \times \rho_{ep}(z_p) + \rho_h \text{ for } -L_t - L_h \leq z \leq -L_t \qquad (4.3)$$

$$\rho_i(z) = COV \times \rho_{bpW}(z_p) + (1-COV)\rho_{Water} \text{ for } -L_t - L_h - (L_p - PEN) \leq z \leq -L_t - L_h, \qquad (4.4)$$

where COV represents the percentage of interfacial area covered by protein boxes, ρ_t and ρ_h are the electron densities of SOPC head group and tail group layers. The height $z_p = z - d_p$, where d_p is the distance between the bottom of the lipid monolayer and the bottom of protein box. The penetration $PEN = L_t + L_h - d_p$ indicates the distance from the interface of water and headgroup to the residue that penetrates most deeply. A schematic of cPLA2α-C2 bound to SOPC monolayer is shown in Figure 29. The intrinsic electron density profile is convoluted with a Gaussian roughness function with interfacial roughness σ calculated from capillary wave theory. The roughened profile is then sliced into hundreds of layers of thickness 0.2 Å to calculate X-ray reflectivity by the Parratt algorithm. X-ray reflectivity curves are fit to the model profile with a non-linear least square algorithm. The electron density of a protein box with and without water at height z_p are represented by $\rho_{bpW}(z_p)$ and $\rho_{ep}(z_p)$. The electron density of a protein box with DCE is $\rho_{bpD}(z_p)$. The box dimensions are based on the orientation of the protein and correlated to θ and φ. The length L_p is the length of protein in z direction under certain orientation.
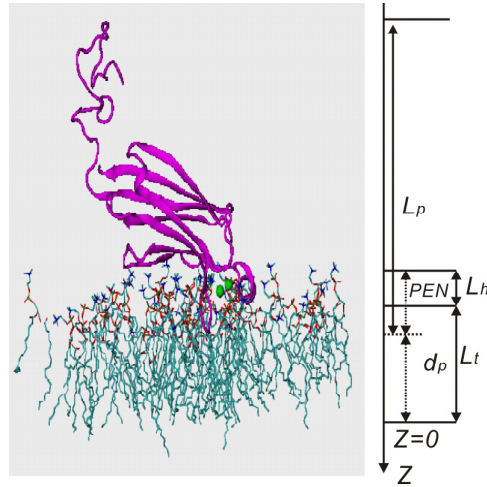
Figure 29. Schematic of cPLA2α-C2 bound to SOPC monolayer.

X-ray reflectivity analyzed according to this model yields the orientation and penetration of the protein into the lipid monolayer. Since the electron profile of cPLA2α-C2 in z direction varies for different protein orientations, the electron density profiles are taken to fit the reflectivity data, which yields the best orientation and penetration depth. Based on molecular structure studies[117] and our lipid research, limits are placed on some of the parameters to simplify the fitting procedure. The thickness of head group layer L_h is limited to 5 Å -12 Å and the thickness of tail group layer L_t is limited to 12.5 Å -21 Å. The electron density in the tail group layer ρ_t is limited to 0.27 e/Å^3 - 0.36 e/Å^3 from the previous study of electron density of SOPC hydrocarbon chains (Chapter 3) after taking into account the volume of the SOPC tail group and area per lipid. The electron densities in tail group ρ_t from the best fit were found within this range when $\Delta\phi^{w-o}$ is between -0.07 V and 0.18 V. When $\Delta\phi^{w-o}$ equals 0.38 V, the limit of ρ_t is set to 0.27 e/Å^3 - 0.375 e/Å^3 because ρ_t increases as $\Delta\phi^{w-o}$ increases. When the upper limit on ρ_t is set to 0.375 e/Å^3, which is almost the same as DCE phase electron density, ρ_t of the best fit will not be affected by the limit setting. The interfacial roughness for each potential is calculated from the interfacial tension, with a lower limit corresponding to the presence of a bending rigidity of 10 k_BT [25,26] and the upper limit to 0 k_BT.

X-ray reflectivity data for different $\Delta\phi^{w-o}$ were analyzed for orientations of cPLA2α-C2 over the range $0° \le \theta \le 180°$, $0° \le \varphi \le 360°$ to identify the best-fit orientation. Contour plots of the goodness of fit parameter χ^2 are shown in Figure 30 and Figure 31, as well as the areas corresponding to 1, 2, and 3 standard derivations (SD) from the best-fit. The center of the 1st SD area is taken as the best-fit orientation.

Electric potential difference $\Delta\phi^{w-o}$ = **-0.07 V, 0.13 V, 0.18 V** The centers of the 1st SD area for potential difference -0.07 V, 0.13 V, 0.18 V are well defined as shown in Figure 30.
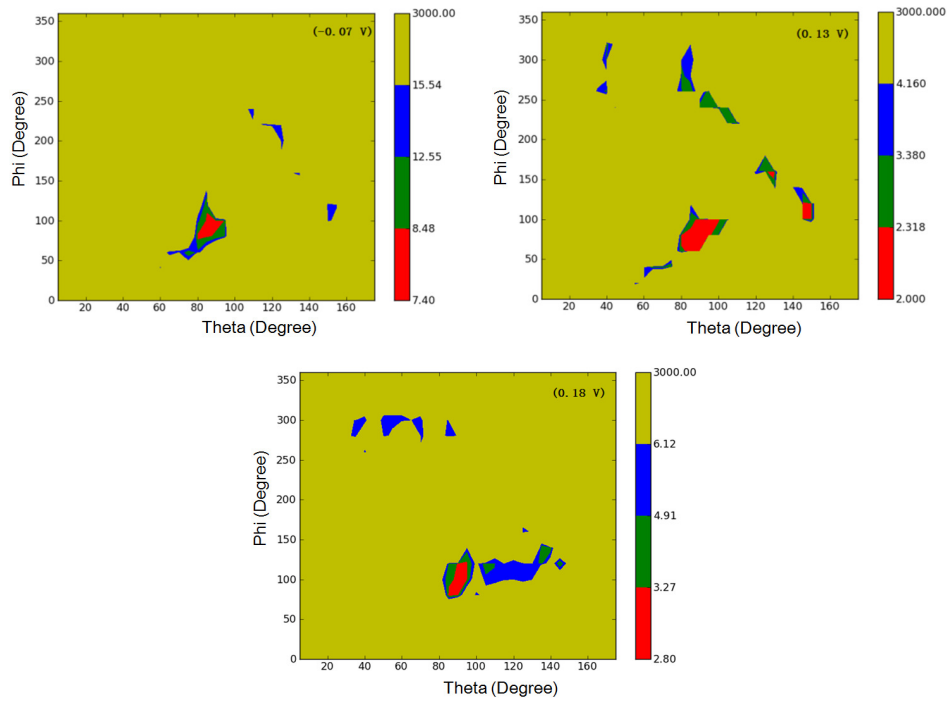
Figure 30. Contour plots of the goodness of fit (χ^2) to the X-ray reflectivity data for the cPLA2α-C2 domain oriented at angles θ and φ under different potential differences (-0.07 V, 0.13 V, 0.18 V). One to three standard deviations (SD) from the best fits are drawn in red, green, and blue (shown in the legend). The regions colored olive represent fits that vary from the best fit by more than 3 SD. The center of the 1st SD area is taken as the best fit.

Electric potential difference $\Delta\phi^{w-o}$ **= 0.03 V** For $\Delta\phi^{w-o}$ = 0.03 V, whose χ^2-contour plot is shown in

Figure 31, the best-fit configuration is not well defined. A consideration of known qualitative features of

cPLA2α-C2 binding can eliminate some of the ambiguity. For example, biochemical and X-ray studies

demonstrate that the calcium binding loops (CBLs) of cPLA2α-C2 are essential for protein binding.[13,14,102] The

binding of calcium alters the electric potential of the protein domain, leading to an electrostatic attraction with

the SOPC headgroup dipole moment. In addition, penetration of hydrophobic residues on the CBLs into the

SOPC monolayer will lead to favorable interactions with the lipid tailgroups. Since it is known that the bulk of

the cPLA2α-C2 cannot penetrate into the lipid layer, the orientations in the region marked "II" in Figure 31

correspond to CBLs located in the aqueous solution outside of the lipid layer and will not be considered further.

In addition, orientations with $\theta \geq 100°$ have CBLs located in the aqueous solution outside of the lipid layer and

will not be considered further.
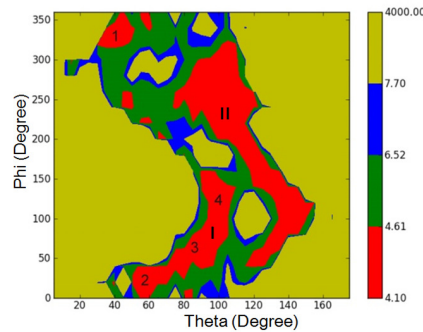
Figure 31. Contour plot of the goodness of fit (χ^2) to the X-ray reflectivity data for the cPLA2α-C2 domain
oriented at angles θ and φ for $\Delta\phi^{w-o}$ = 0.03 V.

There are two regions marked 'I' and "II" in the contour plot. The orientations in domain "II"

correspond to CBLs located in the aqueous solution outside of the lipid layer. The four best-fit orientations for

this potential difference are marked as "1" ($\theta = 40°, \varphi = 320°$), "2" ($\theta = 64°, \varphi = 50°$), "3"($\theta = 84°, \varphi = 70°$), "4"

($\theta = 100°, \varphi = 260°$). The four best-fit orientations of cPLA2 α -C2 of the 0.03 V reflectivity measurements can yield identical electron profile. Table 5 contains the fitting parameters for the four best-fit orientations.

Table 5. Best-fit parameters of the four minima for $\Delta\phi^{w-o} =$ 0.03 V.[a]

	1	2	3	4
$\theta\,(°)$	40	60	84	100
$\varphi\,(°)$	320	40	70	140
σ (mN/m)	$8.6^{+0.3}_{-1.2}$	$8.6^{+0.3}_{-1.2}$	$8.6^{+0.3}_{-1.2}$	$8.6^{+0.3}_{-1.2}$
L_h (Å)	$9.8^{+2.1}_{-4.7}$	$6.2^{+4.3}_{-1.1}$	$6.9^{+5.1}_{-1.9}$	$9.4^{+2.6}_{-3.0}$
ρ_h (e/Å^3)	$0.425^{+0.059}_{-0.024}$	$0.402^{+0.031}_{-0.048}$	$0.415^{+0.042}_{-0.039}$	$0.459^{+0.023}_{-0.047}$
L_t (Å)	$14.7^{+6.3}_{-1.5}$	$14.1^{+6.4}_{-1.6}$	$15.7^{+4.8}_{-3.2}$	$12.7^{+8.4}_{-0.2}$
$L_{\min}$ (Å)	12.5	12.5	12.5	12.5
ρ_t (e/Å^3)	$0.321^{+0.018}_{-0.022}$	$0.312^{+0.021}_{-0.036}$	$0.336^{+0.006}_{-0.025}$	$0.308^{+0.033}_{-0.004}$
COV	$0.80^{+0.03}_{-0.11}$	$0.98^{+0.02}_{-0.06}$	$0.91^{+0.02}_{-0.06}$	$0.83^{+0.005}_{-0.12}$
PEN (Å)	$9.5^{+0.5}_{-1.4}$	$17.1^{+2.6}_{-1.56}$	$11.5^{+1.7}_{-1.7}$	$2.4^{+3.0}_{-0.8}$

[a]The interfacial roughness σ is not fit to the reflectivity data, rather it is calculated from capillary wave theory using the measured values of interfacial tension. The "+" error on σ is due to measured errors on the interfacial tension and the "-" error is due to the possibility of a small interfacial bending rigidity 10 $k_B T$.[14] The fitting program is listed in 1.a.i.Appendix D.

As shown in Figure 32, for the $\theta = 40°, \varphi = 320°$ orientation 1, a 9.5 Å penetration of cPLA2α-C2 leads to the residue ALA34 (A34) of CBL1 having the deepest penetration into the SOPC monolayer. In addition the residue VAL127 (V127) on a β-strand has an almost equivalently deep penetration. This orientation will not be considered further because previous EPR and X-ray measurements are not consistent with deep penetration of a β-strand. Orientation 4, $\theta = 100°, \varphi = 260°$, has a very shallow penetration of 2.4 Å. CBL3 barely penetrates into the SOPC headgroup, and CBL1 is left in the water phase. In this case the β3-strand, not the CBLs, seem to be responsible for the binding. Mutational,[13] X-ray reflectivity,[14] and labeling[104] studies have identified the residues in the CBLs that play a key role in membrane binding. The results of the mutational study by Bittova et al.[13]

shows that all of the hydrophobic residues except for Met38 and Met98 in CBL1 and CBL3 appear to have significant contributions to the hydrophobic membrane binding. Previous X-ray reflectivity measurements at the water-vapor interface demonstrated that both CBL1 and CBL3 penetrated into the lipid monolayer.[14] In addition, the orientation from EPR measurements also showed that both CBL1 and CBL3 are interacting with the lipid membrane and involved in membrane penetration.[13,102,103,115] Therefore, this configuration will also not be considered further because it contradicts previous results that implicate the CBLs in the binding and provide support for a critical role for Ca^{2+} ions in the lipid-protein binding.[13,14,102,115]
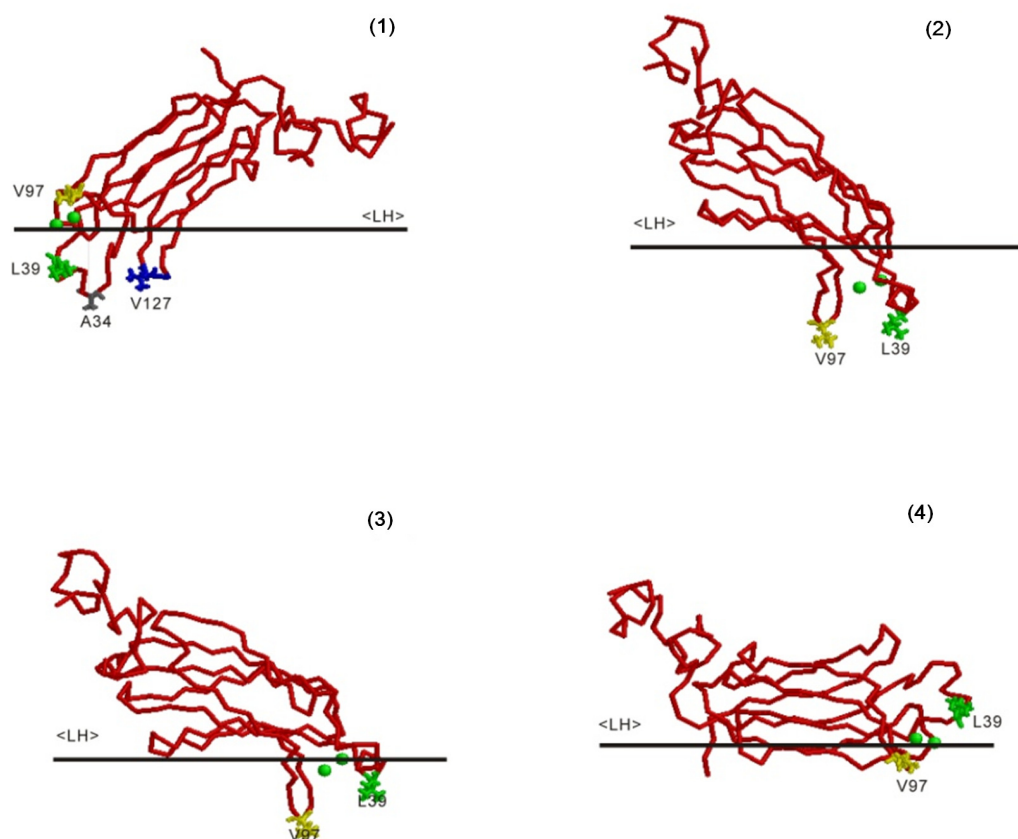
Figure 32. Four best-fit protein configurations for the reflectivity under potential difference 0.03 V. (1) $\theta = 40°, \varphi = 320°$ (2) $\theta = 60°, \varphi = 40°$. (3) $\theta = 84°, \varphi = 70°$ (4) $\theta = 100°, \varphi = 140°$ The green spheres in the figures represent Ca^{2+} ions. The horizontal line marked <LH> represents the top of the lipid head group layer. The distance between the deepest atom and the horizontal line is determined from the fit and the atomic crystallographic arrangement in PDB ID:1RLW.

Orientation 2, near $\theta = 60°, \varphi = 40°$, exhibits a very deep 17.1 Å penetration that leads to penetration of both CBL1 and CBL3 into the SOPC monolayer, with V97 on CBL3 and L39 on CBL1 penetrating most deeply to nearly the same depth. The penetration is so deep that Ca^{2+} atoms are far from the lipid phosphate, which does not agree with previous X-ray and EPR measurements.[13,14,102,115] Also this orientation doesn't agree with the measurements at other values of $\Delta\phi^{w-o}$.

Orientation 3, $\theta = 84°, \varphi = 70°$, which has 11.5 Å penetration, is chosen as the most appropriate orientation for $\Delta\phi^{w-o} = 0.03$ V. CBL1 and CBL3 penetrate into the SOPC monolayer, but V97 of CBL3 penetrates more deeply than L39 which is consistent with the result of Frazier et al.[115] This orientation is sensibly similar to the best-fit orientations for slightly smaller and larger values of $\Delta\phi^{w-o}$. The Ca^{2+} atoms are at nearly the same level as the lipid phosphate, which is considered to be important for the Ca^{2+} activated protein binding to the lipid.[102] Also, this orientation is close to the results of Ball et al.[104] for cPLA2α-C2 bound to DOPM.[104]

Fitting parameters for the best-fit orientations are shown in Table 6. The penetrations for all the $\Delta\varphi^{w-o}$ between -0.07 V and 0.18 V are fitted to be nearly 12^{+3}_{-3} Å. The area per cPLA2α-C2 on the lipid layer is calculated from the area of the protein box of each best-fit configuration on xy plane.[12] For $\Delta\phi^{w-o} = $ -0.07 V, 0.03 V, 0.13 V, 0.18 V, the area per protein is 2203 Å^2, 1963 Å^2, 2013 Å^2, 2245 Å^2, respectively. Area per cPLA2α-C2 measured from the radioactive labeling method is 2110 Å^2,[14] which agrees well with our results.

Electron density profiles of cPLA2α-C2 bound to SOPC monolayer are shown in Figure 33. Although there are substantial error bars listed for the model fitting parameters in Table 6, the electron density profiles shown in Figure 33 are well defined. In other words, electron density profiles for a given value of $\Delta\phi^{w-o}$ are indistinguishable when produced from different sets of fit parameters that are taken from fits that fall within 1 standard deviation of the best fit. The electron density profiles shown in Figure 33 provide a more accurate representation of the experimental results than the error bars shown in Table 6 because of statistical correlations between fit parameters in the chosen model. A similar statement can be made about the analysis of X-ray reflectivity from SOPC monolayers presented in Table 3 and Figure 21a of Chapter 3. Consequently, we will compare the results in Figure 33 directly to the results in Figure 21a by extracting values of electron densities

directly from the figures.

Table 6. The parameters for cPLA2 α-C2 protein domain bound to SOPC lipid monolayer on water-DCE interface under potentials $\Delta\phi^{w-o}$ = -0.07 V, 0.03 V, 0.13 V, 0.18 V. [a]

	-0.07 V	0.03 V	0.13 V	0.18 V
$\theta\,(°)$	86	84	90	90
$\varphi\,(°)$	95	70	90	100
σ (mN/m)	$8.8^{+0.3}_{-1.2}$	$8.6^{+0.3}_{-1.2}$	$9.2^{+0.3}_{-1.1}$	$9.4^{+0.3}_{-1.1}$
L_h (Å)	$6.6^{+5.4}_{-1.6}$	$6.9^{+5.1}_{-1.9}$	$8.5^{+3.5}_{-3.5}$	$8.5^{+3.5}_{-3.5}$
ρ_h (e/Å^3)	$0.422^{+0.028}_{-0.038}$	$0.415^{+0.035}_{-0.039}$	$0.412^{+0.038}_{-0.022}$	$0.439^{+0.011}_{-0.053}$
L_t (Å)	$16.7^{+2.5}_{-4.2}$	$15.7^{+4.8}_{-3.2}$	$15.2^{+5.0}_{-2.6}$	$15.6^{+4.9}_{-3.6}$
L_{min} (Å)	12.5	12.5	12.5	12.5
ρ_t (e/Å^3)	$0.315^{+0.023}_{-0.023}$	$0.336^{+0.006}_{-0.025}$	$0.339^{+0.007}_{-0.023}$	$0.346^{+0.013}_{-0.021}$
COV	$0.82^{+0.03}_{-0.03}$	$0.91^{+0.02}_{-0.06}$	$0.82^{+0.05}_{-0.03}$	$0.83^{+0.036}_{-0.032}$
A_{box} (Å^2)	1806	1767	1671	1841
A (Å^2)	2200^{+80}_{-80}	1960^{+40}_{-130}	2010^{+120}_{-80}	2220^{+100}_{-90}
PEN (Å)	$10.4^{+1.9}_{-1.9}$	$11.5^{+1.7}_{-1.7}$	$10.6^{+1.8}_{-2.0}$	$11.2^{+1.4}_{-3.2}$

[a]The Euler angles (θ, φ) of best-fit configuration for each potential are listed. The items COV, ρ_h, ρ_t, L_t, L_h, d_p, θ, φ, σ are fitting parameters. The lower limit of L_t is represented as L_{min}. The limits on σ are not fitted errors, rather they are calculated from the capillary wave theory. The upper limit on σ is calculated from the experimental uncertainty of the interfacial tension measurement, and lower limit is calculated by assuming a bending rigidity of 10 $k_B T$. The parameter σ is fit within the stated limits. Box size[12] of the protein is A_{box}. Area per protein A is calculated from $A = A_{box} / COV$.
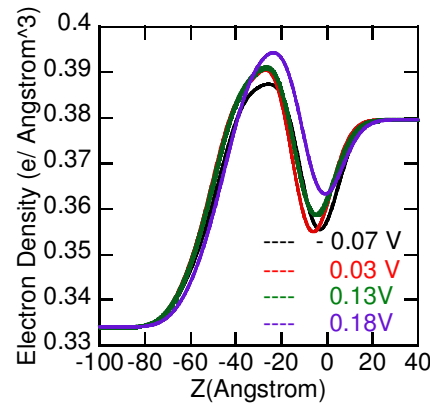
Figure 33. The electron density profile of cPLA2α-C2 and SOPC monolayer binding system as a function of interfacial depth.

Figure 21a shows that the electron densities of the lipid tail group layer determined from a study of SOPC monolayers without protein are about 0.343 e$^-$Å^{-3} for $\Delta\phi^{w-o}$ = 0.18 V and 0.341 e$^-$Å^{-3} for $\Delta\phi^{w-o}$ = -0.07 V, 0.03 V, and 0.13 V. After binding to cPLA2α-C2, the electron densities of the lipid tail group layer have increased to about 0.361 e$^-$Å^{-3} for 0.18 V and 0.355 e$^-$Å^{-3} for the other values of $\Delta\phi^{w-o}$. Because the roughness in two systems are different, the electron density profiles shown in Figure 21a were re-plotted with the same roughness as the lipid monolayer after binding in order to investigate the influence of the roughness on tail group layer electron density. This shows that the tail group layer electron density increased to 0.35 e$^-$Å^{-3} for $\Delta\phi^{w-o}$ = 0.18 V and 0.346 e$^-$Å^{-3} for $\Delta\phi^{w-o}$ = -0.07 V, but they are still lower than for the lipid monolayer after the binding. Note that a similar increase in electron density is also apparent from Tables 3 and 6, however, the error bars on the smaller and larger values do not allow them to be distinguished. As recently stated, these error bars are artificially large due to correlations between parameters in the model, but the electron density profiles shown in the figures are more accurately defined (±0.003 e$^-$ Å^{-3}). In addition to an increase in the tail group electron density upon protein binding, the tail group density also increases as $\Delta\phi^{w-o}$ increases from the lower values of $\Delta\phi^{w-o}$ (up to about 0.13 V) to $\Delta\phi^{w-o}$ = 0.18 V.

The increase in tail group layer electron density upon protein binding can be due to either protein penetration into the tail group layer or to DCE penetration into the tail group layer that occurs because of an increase in the area per lipid when cPLA2α-C2 penetrates into the head group region of the SOPC monolayer. As discussed, X-ray reflectivity measurements provide indirect evidence that several residues from CBL3 of cPLA2α-C2 penetrate into the tailgroup layer. If the increase in the tail group electron density is the effect of the residues, by assuming the length of tail group layer L_h to be 15 Å, the increase of the electron density caused by the CBL3 $\Delta\rho_t$ to be 0.01 e⁻Å⁻³, one can easily calculate the number of electrons that is necessary to cause this change: $n_{ele} = L_h * A * \Delta\rho_t$ =300 e⁻, where A is the area per protein and set to be 2000 Å² for approximation, and $COV = 1$. The total number of electrons for residues (TYR96, VAL97, MET98) is about 123, and even the number of electrons for CBL3 (ASP93-GLU100) is 267; therefore we can estimate that the contribution from the residues penetrating into the tail group is about 0.005 e⁻Å⁻³, assuming a coverage of 1. This issue can be investigated further by a more direct comparison of the electron density profiles from experiments without cPLA2α-C2, whose results are shown in Figure 21a, and the electron density profiles from experiments with cPLA2α-C2, but artificially removing the protein by setting $COV = 0$, but and keeping the other best-fit parameters unchanged. This provides two sets of electron density profiles, one that shows the SOPC monolayer before adding protein to the sample and the other that shows the structure of the SOPC monolayer in the presence of the protein, but with the protein extracted.

These artificial SOPC-only electron density profiles for $\Delta\phi^{w-o}$ = -0.07 V, 0.13 V and 0.18 V are shown in Figure 34 to exhibit correlations with protein configurations. Four configurations in 1st SD area of each potential are used to generate the electron profiles, and one can observe that the tailgroup layer electron density increases as θ increases. It is because that under 1st SD area the decrease of θ will result in larger penetration depth and increases the contribution from residues of cPLA2α-C2, but even the smallest electron density is still significantly greater than 0.343 e⁻Å⁻³ for 0.18 V and 0.341 e⁻Å⁻³ for -0.07 V, 0.03 V and 0.13 V or 0.35 e⁻Å⁻³ for 0.18 V and 0.346 e⁻Å⁻³ for -0.07 V, 0.03 V and 0.13 V when roughness is changed to be the same as the rougness after lipid bound with cPLA2α-C2 for lipid-only monolayer tailgroup electron density as shown in Chapter 3. It indicates that the area per lipid increases under these potential differences.

In Figure 35, the electron density profiles for all four potential differences by setting $COV = 0$ are shown. Comparing with Figure 33, the decrease of electron density of the tailgroup layer is observed, and a larger penetration will result in a bigger decrease. When $COV = 0$ the contribution from CBL3 is removed. This confirms that the contribution from the CBL3 residues penetrating into the tail group is less than 0.005 e$^-$Å^{-3}. In addition, comparing with Figure 21a, Figure 35 shows that without the CBL3 residues, the electron densities of the lipid tail group layer are 0.361 e$^-$Å^{-3} for 0.18 V and 0.352 e$^-$Å^{-3} for the other values of $\Delta\phi^{w-o}$, which are still higher than 0.35 e$^-$Å^{-3} for $\Delta\phi^{w-o}$ = 0.18 V and 0.346 e$^-$Å^{-3} for $\Delta\phi^{w-o}$ = -0.07 V. Therefore, DCE penetration into the tail group region upon protein binding, in addition to the effect of the protein penetration into the tail group, is required to explain the measured electron densities in the tail group region. Even though relatively small regions of the protein penetrate into the tail region, the net effect of protein binding is to alter the lipid organization to allow DCE penetration.
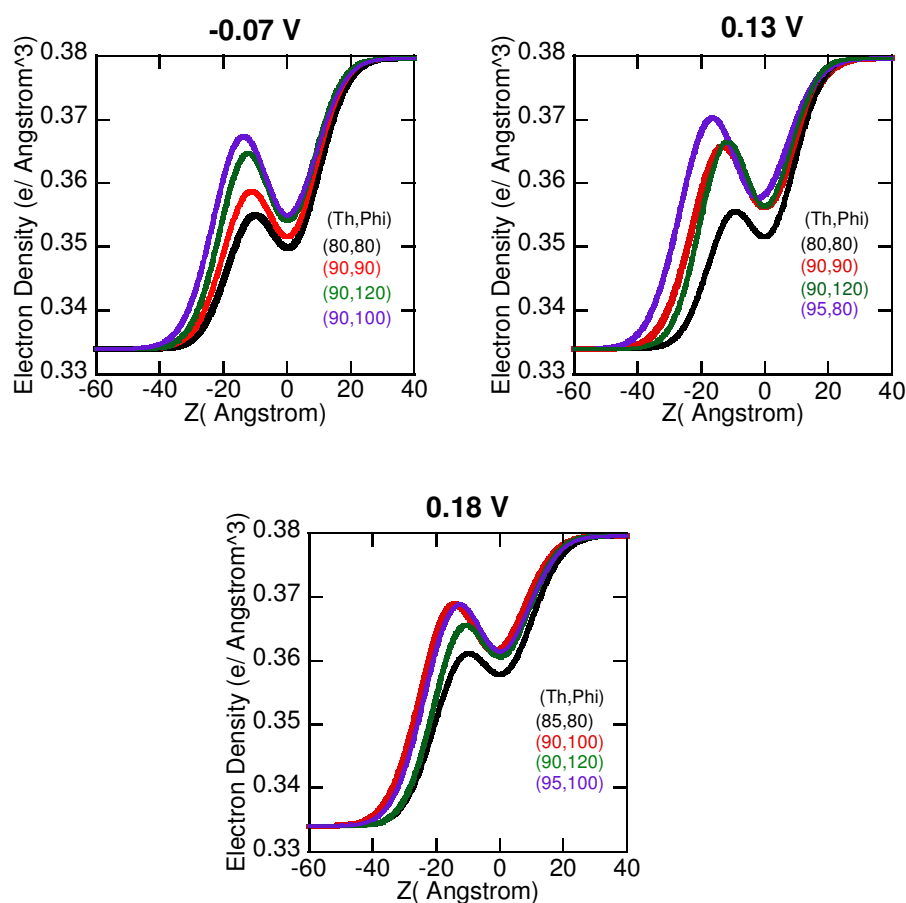
Figure 34. The electron densities for $\Delta\phi^{w-o}$ = -0.07 V, 0.13 V and 0.18 V when the protein cPLA2α-C2 is artificially removed from the SOPC monolayer by setting $COV = 0$.
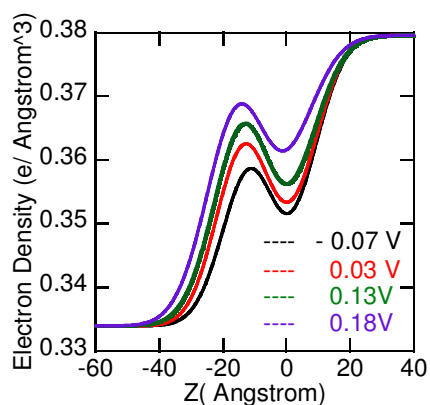
Figure 35.   The electron density profile of SOPC monolayer at best-fit orientations when the protein cPLA2α-C2 is artificially removed from the SOPC monolayer by setting $COV = 0$.

4.4   <u>Molecular Dynamics Simulations</u>

4.4.1   Simulation procedures

All-atom molecular dynamics (MD) simulations were performed by our collaborators Zenmei Ohkubo and Emad Tajkhorshid (University of Illinois at Urbana-Champaign) in order to investigate the binding of cPLA2α-C2 to a PC-lipid monolayer at atomic resolution. NAMD package[118] in conjunction with the CHARM27 force field parameters[119] and the CMAP corrections[120] was employed. The details of the simulation settings were described elsewhere[121].

4.4.2   Binding of cPLA2α-C2 to a monolayer of short-tailed PC lipids

In order to realize a spontaneous, repeated binding of cPLA2α-C2 to lipid monolayers within a computationally accessible time, the HMMM model is employed, i.e., divalerylphosphatidylcholine (DVPC) is used as a short-tailed version of SOPC. The simulated system consisted of a 90-Å-thick upper water layer, a 30-Å-thick DCE layer, and a 20-Å-thick lower water layer with 222 DVPCs at the water-DCE interfaces (111 lipids per interface) and a cPLA2α-C2 placed initially ~10 Å above the upper interface, resulting in a ~137 X 90 X 90 $Å^3$ (along the x, y and z axes) unit cell. The system was then neutralized with Na^+ and Cl^- ions while the concentration of the cation was set at of 0.1 M, followed by a short energy minimization and relaxation with weak restraints on the C2 atoms of SOPC as used for the MD simulation in Chapter 3. Subsequently, 50-ns-long NPnAT simulations were repeated 3 times. One of these simulations was extended to 100 ns in order to convert to the full-lipid (SOPC) system.

4.4.3   The SOPC monolayer-bound cPLA2α-C2 with applied electric fields

To simulate the PC-bound cPLA2α-C2, the system of short-tailed lipids was converted to the full-lipid system, i.e., DVPC lipids in the system mentioned in the previous section were converted to SOPCs, by extending their acyl tails. The tail-growing was performed by utilizing carbon atoms in DCE in a repeated manner. For each carbon at the tail tips (C5 in the first cycle, then C7, C9… in the following cycles), the closest available DCE was picked. Then the chlorines in the DCE were removed and appropriate bonding among the carbons and addition/removal of hydrogens were processed to make a 2-carbons-longer tail. Once all tails were

elongated, the modified system was treated by a short energy minimization and equilibration. This process was repeated until all DVPC lipids were extended to become SOPC lipids.
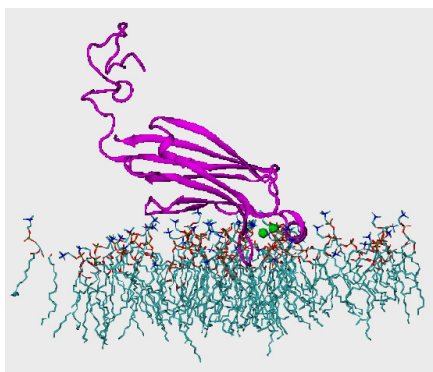
Figure 36. cPLA2α-C2 bound to SOPC monolayer at the water (top)-DCE (bottom) interface. The lipid density is 73 Å^2/ lipid and a postive electric field is applied perpendicular to the monolayer surface in the $-z$ direction.

It is often the case that the closest available DCE was not quite in the neighborhood of a tail tip of interest. The energy-minimization, however, quickly changed the positions of the carbons to realize the standard carbon-carbon bonding distance, providing some randomness in the orientation of the acyl tails. The introduced randomness is desirable, because it dramatically reduces the time needed for the grown tails to be equilibrated (or "melted"), when compared to the case in which tails of upright, regular conformations are added

The DCE slab between the two leaflets of SOPC was supplemented with more DCE molecules after tail-growth, because the process made the DCE layer too thin. The resulting modified system was ~166 X 90 X 90 Å^3. A short energy-minimization and relaxation with weak restraints on the C atoms of cPLA2α-C2 were performed, and then 50-ns-long NPnAT simulations were repeated with different electric fields applied along the membrane normal (0 V, ±0.2 V, ±0.3 V, and ±0.5 V, respectively).

Table 7. The result of penetration and deepest residue penetrated into the SOPC monolayer from MD simulation

Potential (V)	θ	φ	PEN (Å)	Deepest Residue	Running Time (ns)
-0.5	52	67	8.2	L39	50
-0.3	66	60	9.5	V97	50
-0.2	70.6	70	10.3	V97	50
0	60.5	56.7	8.5	L39	200
0.1	65	78	10.5	V97	50
0.2	60.2	60	8.2	V97	300
0.3	63.5	56.8	8.3	V97	400
0.5	46	59	8	L39	50

4.5   Discussion

4.5.1   Comparison between different results
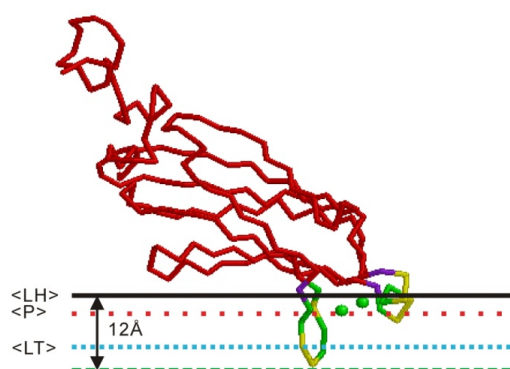
Figure 37．Backbone representations of the best-fit configuration. The experimental $\theta = 84°, \varphi = 70°$ orientation with a protein penetration of $11.5^{+1.7}_{-1.7}$ Å is shown. The lines marked <LH> and <LT> represent the average head group/water and headgroup/tailgroup interfaces, respectively. The red dashed line indicates the average level of the lipid phosphates that lies close to the mid-plane of the lipid headgroup. Hydrophobic residues are drawn in yellow, hydrophilic residues in green, and neutral residues in purple. The green spheres represent Ca^{2+} ions.
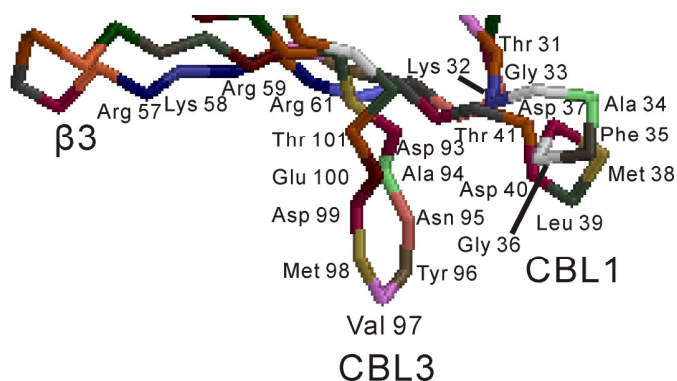
Figure 38. Residuals on CBL3, CBL1 and β3

The best-fit orientation of the cPLA2α-C2 binding to SOPC monolayer proposed in this chapter under

0.03 V is $\theta = 84°, \varphi = 70°$, and the penetration is fit to be $11.5^{+1.7}_{-1.7}$ Å. The schematic of the protein bound to

SOPC monolayer is shown in Figure 37. The distances between the atoms in this schematic are estimated by the

coordination of the cPLA2α-C2 provided in the protein data bank (PDB ID:1RLW). The average distance

between the headgroup phosphate PO_4^- and the headgroup/water interface (marked <LH> in Figure 37) is

estimated to be about 4 Å.[14] Based on this geometry, the Ca^{2+} ions in the cPLA2α-C2 are almost at the same

level as PO_4^-. This result is consistent with the models discussed by Malmberg et al.[102] and Malkova et al.[14] It is

known that the binding of C2 domains to the lipid layer is driven by two kinds of interactions, electrostatic and

hydrophobic, as well as entropic effects.[14] In our best-fit orientation, the tip of CBL3 inserts into the hydrocarbon

phase of the lipid tailgroup, while the other CBL1 remains in the headgroup region or the aqueous phase. This

orientation is very similar to the model proposed by Perisic et al.[103] It is consistent with the amino acid

composition of the CBLs. Assuming that the geometry of the protein from the PDB file remains unchanged upon

protein binding, the positions of amino acid residues can be determined by inspection of Figure 37 and Figure 38.

The three residues that penetrate most deeply, Tyr 96, Val 97, Met 98, are large and hydrophobic. Biochemical

studies show that Tyr 96 and Val 97 make a large contribution to protein binding[13], in agreement with the

orientation shown in Figure 37 . Hydrophilic residues Asp 93, Ala94, Asn 95, Asp 99, Glu 100, and Thr 101

remain in the headgroup region or in water. Some residues of CBL1 insert into the lipid head group.

Hydrophobic residues Phe 35, Met 38, Leu 39 were found in the head group region which can interact with

hydrophobic methyl groups of the lipid head group.[103] Hydrophilic residues Thr 31, Lys32, Asp 37, Asp 40, and Thr 41 in CBL1 are in contact with the lipid head group and water. In addition, the three cationic residuels (Arg 57, Lys 58, Arg 59) are positioned close to the lipid monolayer in this orientation,. This may explain how the β3-strand can be involved in membrane binding, as suggested by the mutational study of cationic residues by Bittova et al.[13]

Significant changes in the orientation were not observed between $\Delta\phi^{w-o} =$ -0.07 V, 0.03 V, 0.13 V and 0.18 V, and the orientations are similar to Figure 37. In the MD simulation, the configuration without imposed electric field is determined to be $\theta = 61° \pm 5°, \varphi = 57° \pm 10°$ with a penetration of ~9 Å. The orientation doesn't change much with potential differences between -0.3 V and 0.3 V. The MD result is similar to the experimental result for small electric potential differences, for example $\Delta\phi^{w-o} = 0.03$ V.

EPR measurements of the cPLA2α-C2 bound to POPC/POPS vesicles are also compared to our results, and the orientations from Frazier et al. [115], Malmburg et al.[102] are $\theta = 68°, \varphi = 66°$, and $\theta = 52°, \varphi = 53°$, respectively, though error bars on these values were not provided. Ball et al.[104] also used EPR to measure cPLA2α-C2 bound to DOPM (1,2-dioleoyl-sn-glycero-3-phosphomethanol) vesicles. Although Ball et al.[104] do not provide numerical orientation their configuration is very similar to the configuration reported here, $\theta = 84°, \varphi = 70°$. Wijkander et al.[122,123] found that phospholipase A2 (PLA$_2$) binding to the lipid membrane is affected by the curvature of the substrate by studying highly curved sonicated vesicles (phospholipid or membrane). The binding is much more stable when PKC-c2 is bound to a highly curved vesicles than to a normal membrane because of the change in the spacing among the headgroups of the lipids . This may explain the small differences between the binding orientation determined by EPR and X-ray reflectivity measurements.

4.5.2   The influence of high potential to the binding orientation

It is known that the qualitative behavior of R / R_F at low Q_z is determined by the signs of the electron density gradients at the top and bottom of the interfacial layers.[124] The shape of the normalized reflectivity curves is determined by the sign of the electron density gradients at the top and bottom of the interfacial structure. When $\Delta\varphi^{w-o} \leq 0.18$ V, as shown in Figure 33, the electron density gradient is positive when going from the water

phase to the protein layer and is also positive when going from the lipid tail group layer to the DCE phase. This produces a minimum in R/R_F at low Q_z (= 0.04 Å^{-1}), as seen in Figure 26. On the contrary, when $\Delta\varphi^{w-o} = 0.38$ V, the lipid tail group electron density is almost the same as the DCE phase, as shown in Figure 39, which could be due to desorption of lipid and high interfacial roughness. In this situation, the sign of the gradient of the electron density from water phase to protein layer is positive, but the gradient with the DCE phase is essentially negative. This is consistent with the increase in R/R_F at low Q_z shown in Figure 26 for $\Delta\varphi^{w-o} = 0.38$ V.

When the electric potential difference is increased to 0.38 V, the analysis reveals a significant change in the bound configuration of cPLA2α-C2. Although there are three best-fit regions with $\theta \leq 90°$ shown in Figure 40, only the one with $50° \leq \theta \leq 65°$ is physically sensible and it is very close to the orientation from X-ray reflectivity measurements of cPLA2α-C2 bound to SOPC Langmuir monolayers at the air-water interface.[14] It shows that now both CBL1 and CBL3 penetrate into the SOPC monolayer. Unfortunately, we cannot quantify the penetration of cPLA2α-C2 into the SOPC monolayer because of large error bars, but the data can be fit with 12.4 Å penetration depth and 10.3 Å lipid head group layer thickness at $\theta = 55°, \varphi = 100°$. This orientation is very close to the results of Malkova et al.[14] We suggest the following explanation for these results. When $\Delta\varphi^{w-o}$ increases, the area per lipid on the interface increases, and more room is available for CBL1 to penetrate into SOPC monolayer. In addition, the electrostatic equipotential profiles[125] of cPLA2α-C2 show that the negative residues on the β-sheets may be rotated by the large positive external electric field, which could contribute to the change in orientation to make the CBL1 penetrate into the SOPC tailgroup layer.
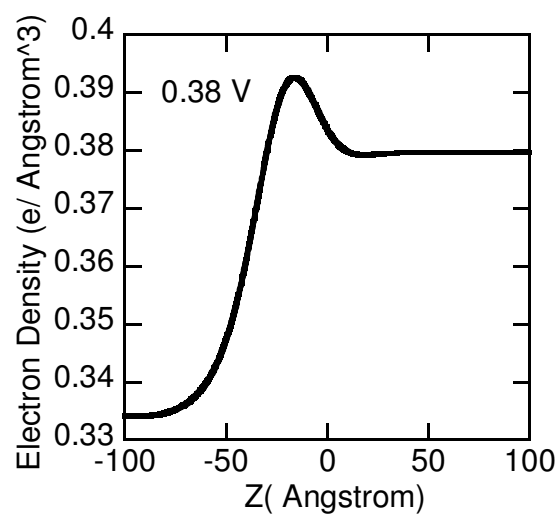
Figure 39 The electron density profile of cPLA2α-C2 and SOPC monolayer binding system as a function of interfacial depth at $\Delta\varphi^{w-o} = 0.38$ V.
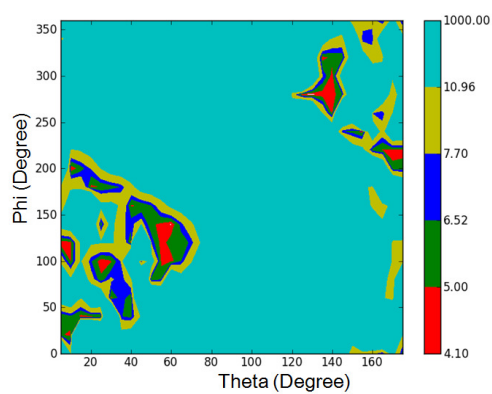
Figure 40. Contour plot of the goodness of fit (χ^2) to the X-ray reflectivity data for the cPLA2α-C2 domain oriented at angles θ and φ under difference potential difference. One to four standard deviations (SD) from the best fits drawn in red, green, blue, yellow (shown in the legend) corresponding to the best fit.

4.6   Conclusion

The analysis of X-ray reflectivity on cPLA2α-C2 domains bound to the SOPC monolayer on the water|DCE interface provides information on the angular orientation and penetration depth of the domains. An electric field is applied across the interface containing the cPLA2α-C2 bound to SOPC monolayer to investigate the effects of different membrane potentials on protein binding. To acquire the information, a two-slab model is built for the SOPC layer and the additional electron density from the crystal structure of cPLA2α-C2 under different orientation is utilized in the model to fit the X-ray reflectivity.

Although X-ray reflectivity curves for potential difference $\Delta\phi^{w-o}$ =-0.07 V, 0.03 V, 0.13V, 0.18V are quite different, the best-fit orientations for these four potentials are very similar. The best-fit orientation for 0.03 V is $\theta = 84°, \varphi = 70°$, and the penetration is $11.5^{+1.7}_{-1.7}$ Å. Under this orientation, the calcium binding loop CBL3 penetrates into the hydrocarbon chains of the SOPC monolayer, and the hydrophobic interaction between the chains and the hydrophobic residues such as V97 is believed to be important for binding. In addition, the Ca^{2+} ions on the CBLs are located within 1 Å of the lipid phosphate group, which can increase the electrostatic attraction between cPLA2α-C2 and lipids. This configuration generally agrees with the MD simulation and EPR measurements carried out by other groups.

Under low potential difference range (-0.07 V to 0.18 V), after the binding, the electron profile shows an increase of electron density in lipid hydrocarbon chains. The contribution from the residues of CBL3 to the electron density has been estimated to be less than 0.005 e⁻Å⁻³, but the electron densities of the lipid tail group layer have increased from 0.35 e⁻Å⁻³ for $\Delta\phi^{w-o}$ = 0.18 V and 0.346 e⁻Å⁻³ for $\Delta\phi^{w-o}$ = -0.07 V (roughness has been changed) to about 0.361 e⁻Å⁻³ for 0.18 V and 0.355 e⁻Å⁻³ for the other values of $\Delta\phi^{w-o}$ after cPLA2α-C2 binds to SOPC monolayer. The protein penetration is protein penetration is responsible for some but not all of the increase in tail group density, thus there is another possibility is DCE penetration into tail group region. This could be due to reorganization of the tail group region of the lipid, or to entire reorganization of proteins due to, for example, an increase in area per lipid. When potential difference is increased to 0.38 V, the reflectivity curves change dramatically. The analysis shows a decrease in protein coverage and penetration. Our study of

SOPC monolayers shows that the lipid density will decrease at these high potentials, thus reducing the number of binding sites for proteins. It is also likely that the highly negative charged (-7.6 at pH=7) cPLA2α-C2 domains are removed from the interface by the large positive potential difference. In addition, the electron density profile shows that the electron density of the tail group layer increases. As demonstrated by our study of just the SOPC monolayer this can be a consequence of DCE penetration into the region of lower tail group density.

Appendix A   <u>ALIGNMENT OF THE QUASI-ELASTIC LIGHT SCATTERING</u>

<u>OPTICS</u>

1. Close the laser shutter, then turn on the laser. Wait about 10 to 15 minutes for the laser to warm up.

2. For alignment, remove the optical fiber attached to the collimator by gently pressing it in and twisting it counterclockwise. Open the the laser shutter and adjust the position of the collimator vertically and horizontally to optimize the laser intensity penetrating through the lenses of the collimator. Then, slightly twist the collimator to make sure that the incident angle of the laser into the collimator is close to 90 degrees. It is critical to adjust the incident angle close to 90 degrees because any misalignment will significantly affect the focusing of the laser beam by the lenses of the collimator onto the optical fiber . Place a piece of white paper behind the collimator. If the collimator is perfectly aligned, the projected laser beam on the white paper should be circular and the brightest spot should at the center of the circle. Then the collimator is fixed with a screw on the collimator holder after the coarse adjustment.

3. Gently re-attach the optical fiber to the collimator, matching the notch on the optical fiber to the collimator. There are six screws surrounding the optical fiber on the collimator. Three of them are used for fine adjustment of the incident angle of the collimated laser into the optical fiber and the others are used to fix the angle once the output of the laser through the optical fiber is optimized either by visual observation of the laser through the optical fiber or use of a power meter. The alignment screws are different from the rest, and the highest screw is one of the alignment screws. Use a special Allen wrench to adjust the screw on top of the optical fiber to maximize the output power of the laser through the fiber. If you do not observe a strong laser beam coming out of the the optical fiber, you should repeat step 2. Adjust the screws on the left and right of the optical fiber to optimize the laser output.

4. Place the other end of the optical fiber into the support on the side of the 3-jaw chuck sample holder. The laser is reflected upwards into the sample cell by the 45° mirror mounted in the middle of the chuck. After being scattered by the interface, the laser will be diffracted by an optical grating placed in the bottom of the glass tube in the upper part of the sample cell. The grating is usually placed onto the bottom of the tube with tweezer. Make sure that the bottom of the glass tube passes into the upper liquid phase by passing through the liquid-vapor interface. Also, check that the platinum mesh does not block the laser beam path. Adjust the

position and tilt angle of the 45° mirror above the sample cell to reflect the laser beam through the convex lens. The diffracted laser beam is focused onto the slit in front of the photodiode. The position of the slit can be adjusted to pass different diffraction orders. The signal is measured by the photodiode, amplified, and subsequently Fourier transformed by the SR760 FFT electronics.

Appendix B   <u>REFLECTIVITY FROM SUPPORTING ELECTROLYTE</u>

It is well known that supporting electrolytes form ion distributions at liquid-liquid interfaces subject to an electric potential difference $\Delta\phi^{w-o}$. The distribution will usually have its highest ion concentration close to the interface, within a distance given approximately by the diameter of the ions. The concentration will decay further from the interface. A similar distribution will be present even when other chemical components, such as lipids or proteins, are adsorbed to the interface. It is expected, though, that at the same value of $\Delta\phi^{w-o}$ the maximum concentration of the ion distribution in this case will be less than in the absence of the adsorbed components because the ions closest to the interface will be displaced from the interface by the adsorbed molecules and, therefore, subject to smaller electric fields. An exception to this will occur if the adsorbed molecules are charged.

The above discussion assumed that the supporting electrolytes have negligible interfacial activity. If, however, the supporting electrolytes are adsorbed to the interface like surfactants, then they can also set up an ion distribution that extends further away from the interface. Depending upon their interfacial activity, they could compete with other interface active components, like lipids or proteins, for a place at the interface. The ion distribution may or may not affect X-ray reflectivity measurements depending upon the electron density contrast between the solvent and the ions. If the contrast is small, then the electron density profile that is produced by the ion concentration profile (i.e., the distribution) will not be very different from the pure solvent and the X-ray reflectivity will not be sensitive to the ion distribution. Here, we show that this is the case for the supporting electrolytes used in this study of lipid monolayers and protein binding.

Figure 41 shows X-ray reflectivity curves measured for different electric potential differences $\Delta\phi^{w-o}$ from the liquid-liquid interface of a sample containing only solvents and supporting electrolytes (100 mM NaCl and 20 mM HEPES in water phase and 5 mM TDATPBCl in DCE phase). These data are fit well by an error function electron density profile that has been used previously to model simple interfaces without adsorption or ion distributions, [29]

$$\langle\rho(z)\rangle = \frac{1}{2}\left(\rho_{DCE} - \rho_w\right)erf\left(\frac{z}{\sqrt{2}\sigma}\right) + \frac{1}{2}\left(\rho_{DCE} + \rho_w\right)$$

where σ is the roughness of the interface. Table 8 compares the best-fit values of roughness to values calculated from capillary wave theory. , $\sigma^2 = (k_B T / 2\pi\gamma)\ln(q_{max}/q_{min})$, where T is the room temperature 23 °C, $q_{max} = 2/r$ is the cutoff for the smallest wavelength capillary waves that uses r as the effective cross-sectional radius. The radii of TDA$^+$ and TPBCl$^-$ are calculated to be 6.62 Å and 5.02 Å based on their volume assuming a spherical shape. The smallest capillary wave vector q_{min} can be resolved by the X-ray measurements, given by

$q_{min} = (2\pi / \lambda)\Delta\alpha_s \sin\alpha_i$ ($\Delta\alpha_s = l/d = 5.6\times10^{-4}$ is the vertical angular acceptance of the detector, where $l = 1.8$ mm is the electronic slit size and $d = 3.19$ mm is the distance from the sample center to the CCD detector). The comparison demonstrates that when $\Delta\phi^{w-o} \geq 0.03$ V, the roughness from the fitting is within about two standard deviations of the calculated roughness. It is expected that the concentrations of supporting electrolytes Na$^+$ and TPBCl$^-$ are enhanced at the interface, and the other two supporting electrolytes depleted, when $\Delta\phi^{w-o} > 0$. The near agreement of the measured and calculated values of roughness indicates that the effect of the supporting electrolytes Na$^+$ and TPBCl$^-$ on the electron density of the interface is negligible.

When $\Delta\phi^{w-o} = -0.12$ V, the electron density profile of the interface is influenced by the supporting electrolytes, either Cl$^-$ or TDA$^+$, thus indicating that the ion distribution or interfacial activity of TDA$^+$ cannot be ignored at negative values of $\Delta\phi^{w-o}$. Fortunately, for values of $\Delta\phi^{w-o}$ in the range from -0.12 V to 0.03 V, the X-ray reflectivity curves from liquid-liquid interfaces with SOPC monolayers are indistinguishable. This means either that SOPC is a much stronger surfactant than the supporting electrolyte TDA$^+$ or that the maximum of the ion distribution of TDA$^+$ is sufficiently weakened by being displaced from the interface by the SOPC monolayer. In either case, these results show that the contribution of the supporting electrolyte to the interfacial electron density profile does not need to be considered in our studies of SOPC monolayers or of protein binding to these monolayers over the range of $\Delta\phi^{w-o}$ from -0.12 V to 0.33 V.
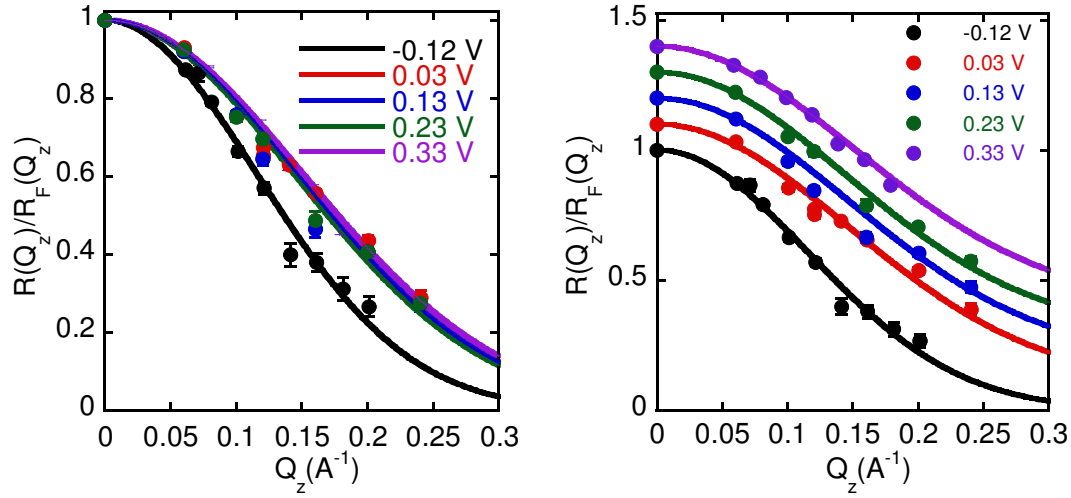
Figure 41. Fresnel reflectivity $R(Q_z)/R_F(Q_z)$ from the liquid-liquid interfaces between 0.1 M NaCl + 20 mM HEPES in water and 5 mM TDATPBCl in DCE under different external electric potential differences. The experiments were carried out at $T \approx 23\,°\text{C}$. In the right-hand figure, curves are ordered from bottom to top with increasing $\Delta\phi^{w-o}$ and are successively displaced upwards for clarity (note that $R(Q_z)/R_F(Q_z) \rightarrow 1$ as $Q_z \rightarrow 0$ for each separate reflectivity curve). Values at $Q_z = 0$ are measurements of the direct beam when the interface is moved out of the beam path.

Table 8. Interfacial roughness calculated from capillary wave theory compared to the roughness from fitting X-ray reflectivity to an error function electron density profile.

Potential ($\Delta\phi^{w-o}$)	Calculated Roughness (Å)	Fit Roughness (Å)
-0.12 V	4.72	$6.11^{+0.09}_{-0.11}$
0.03 V	4.55	$4.82^{+0.11}_{-0.12}$
0.13 V	4.61	$5.01^{+0.15}_{-0.16}$
0.23 V	4.70	$4.89^{+0.09}_{-0.21}$
0.33 V	4.88	$4.68^{+0.05}_{-0.06}$

Appendix C   PARRATT FITTING FUNCTION FOR REFLECTIVITY FROM

SOPC MONOLAYER

This program is used to fit the X-ray reflectivity data with 2-slab model. One slab is head group layer of the lipid which contains the lipid head group and the water molecules penetrate into the head group; the other slab is the tail group of the lipid and the DCE molecules among the hydrocarbon chains. The electron density profile of the model is convoluted by a Gaussian function with interfacial roughness as width. The convoluted electron density profile is cut into slices and Parratt algorithm has been applied to calculate the reflectivity. There are 5 parameters used to describe the electron profile of the interface are fitted in the program as follow:

rough_2: the interfacial roughness

d_1, rho_1:the thickness and electorn density of the 1st slab

d_2, rho_2: the thickness and electorn density of the 2st slab

 d_3: the totoal thickness of the interface

Note that, **d_1=d_3-d_2**; therefore, **rough_2, rho_1, d_2, rho_2, d_3** are fitted in the model. There are also constants to represent the characteristics of the system.

rho_bottom: The electron density of the water phase

rho_top: The electron density of the DCE phase

# of layers: Number of layers to represent the system, and here the number is 2.

wave vector: k0: The wave vector calculated from the energy of the X-ray.

# of slabs: Number of slices the system is cut into for Parrat reflectivity calculation

qz_off: Offset of the transfer of momentum Q_z

The following program is modified based on the the program named *fitref.5.c* developed by Michael Kelley from The Ames Lab (https://www.ameslab.gov/groups/reflec/fitref5-reflectivity-fitting-c-plot), and the program is written in CPLOT (Certified Scientific Software, Cambridge, Massachusetts).

```
/*  @(#)p_proto.5.c        4.4  02 Jul 1993 CSS
*   Certified Scientific Software's C-PLOT
*
*        cplot_complile: makefunc fitref2.5
*
*        This function was written from a modified version of fitref.5.c
```

```
*/

#define VERSION 5


/** Adjust the following 4 parameters for the size of your problem. **/
#define NUM_XS  1      /* The number of independent variables (no limit) */
#define MAXPAR  44     /* The number of P and C parameters total        !!!--!!!*/
#define MAXPTS  1024   /* The most points for fitting */
#define MAXPLT  1024   /* In-core points for plot (pg, ps, md, mr and sA) */

#define lastP  33
#define firstP 1       /* The first and last parameter index value       !!!--!!!*/
#define lastC  11
#define firstC 1

#include <string.h>
#include <math.h>
#include <p_fitsize.h>
#include "cplx.h"     /* Complex math functions */
#include <stdio.h>
#include "error.h"


struct init_4 initial[] = {
    /* Name     Deriv? Fit? Initial  Limit?  Low  High */
    { "rough_1",  0,   0,     7.5,    3,   6,    9, },
    { "rough_2",  0,   1,     8.5,    3,   7,   10, },
    { "scale of y",  0,   1,     1,    3,   0.95,   1.05, },
        { "rho_bottom",  0,   0,  0.3804,   3,   0,    1, },
    { "my_bottom",  0,   0,     0,    0,   0,    0, },
        { "d_1",   0,   1,   10,    3,   7,  15, },
        { "my_1",  0,   0,     0,    0,   0,  3, },
        { "rho_1",  0,   1,   0.28,   3,   0.2,   0.33, },
        { "rough_1",  0,   1,     3,    3,   2,   5, },
        { "d_2",   0,   1,   10,    3,   6,  12, },
        { "my_2",  0,   0,     0,    0,   0,    0, },
        { "rho_2",  0,   1,   0.4,    3,   0.35,  0.45, },
        { "rough_2",  0,   1,     3,    3,   2,    5, },
        { "d_3",   0,   0,   5,    0,   2,  10, },
        { "my_3",  0,   0,     0,    0,   0,  100, },
        { "rho_3",  0,   0,   0.4,    0,   0,    1, },
        { "rough_3",  0,   0,     3,    3,   2,   5, },
        { "d_4",   0,   0,   22,    0,   18,  25, },
        { "my_4",  0,   0,     0,    0,   0,   3, },
        { "rho_4",  0,   0,     0.3,    0,   0.25,   0.35, },
        { "rough_4",  0,   0,     3,    3,   1.5,  8, },
        { "d_5",   0,   0,   5,    0,   2,   10, },
        { "my_5",  0,   0,     0,    0,   0,    0, },
        { "rho_5",  0,   0,     0.4,    0,   0,  1, },
        { "rough_5",  0,   0,     3,    0,   0.5,   10, },
        { "d_6",   0,   0,    22,    0,   18,   25, },
        { "my_6",  0,   0,     0,    0,   0,  100, },
        { "rho_6",  0,   0,   0.3,    0,   0.25,   0.35, },
        { "rough_6",  0,   0,     3,    3,   0.5,  10, },
        { "d_7",   0,   0,    0.3,    3,   2,    4, },
```

```
        { "my_7", 0,  0,    0,   0, 0,   0, },
        { "rho_7", 0,  0,    3,   3,  0, 100, },
        { "rough_7", 0,  0,   0.3,   0,  0,  100, },
        { "# of layers", 0,  0,   4,   0, 0,   0, },
        { "0:ref; 1: ed", 0,  0,   0,   0, 0,   0, },
        { "!= 0, y=log10(y)", 0,  0,    0,   0, 0,   0, },
        { "# of slabs", 0,  0,   100,   0, 0,   0, },
        { "wave vector: k0", 0,  0, 15.176,   0, 0,   0, },
        { "0:ref; !=0:rrf", 0,  0,    1,   0, 0,   0, },
        { "rho_top", 0,  0,   0.3334,   0, 0,   0, },
        { "my_oil", 0,  0,    0,   0, 0,   0, },
        { "qz_off", 0,  0,    0,   3, -0.0006,  0.0006, },
        { "1:fixed rough (rough_0)", 0,  0,    1,   1, 0,   0, },
        { "1:zero rough for ed", 0,  0,    0,   1, 0,   0, },
};

/* Refer to the parameters using the following structure members:
*
*  fpar[i].p_b   - The current value of the parameter.
*  fpar[i].p_fit - When non-zero, the parameter is being fit.
*  fpar[i].p_p   - Assign analytic derivative to this.
*
*  `p_fit' and `p_p' are only relevant for parameters that have the
*  analytic-derivative flag set.
*  The following `defines' may be useful. */

/* Define a mnumonic for ALL of the parameters                 !!!--!!!
   The array/mnumonic order below must correspond to the order defined
   above in the initial structure (above). I.e. the 5th parameter in the list above
   corresponds to the 5th fpar: fpar[4].  */
#define p1   fpar[0].p_b
#define fp1  fpar[0].p_fit
#define dp1  fpar[0].p_p
#define p2   fpar[1].p_b
#define fp2  fpar[1].p_fit
#define dp2  fpar[1].p_p
#define p3   fpar[2].p_b
#define fp3  fpar[2].p_fit
#define dp3  fpar[2].p_p
#define p4   fpar[3].p_b
#define fp4  fpar[3].p_fit
#define dp4  fpar[3].p_p
#define p5   fpar[4].p_b
#define fp5  fpar[4].p_fit
#define dp5  fpar[4].p_p
#define p6   fpar[5].p_b
#define fp6  fpar[5].p_fit
#define dp6  fpar[5].p_p
#define p7   fpar[6].p_b
#define fp7  fpar[6].p_fit
#define dp7  fpar[6].p_p
#define p8   fpar[7].p_b
#define fp8  fpar[7].p_fit
#define dp8  fpar[7].p_p
#define p9   fpar[8].p_b
#define fp9  fpar[8].p_fit
```

```
#define dp9  fpar[8].p_p

#define p10   fpar[9].p_b
#define fp10  fpar[9].p_fit
#define dp10  fpar[9].p_p

#define p11   fpar[10].p_b
#define fp11  fpar[10].p_fit
#define dp11  fpar[10].p_p

#define p12   fpar[11].p_b
#define fp12  fpar[11].p_fit
#define dp12  fpar[11].p_p

#define p13   fpar[12].p_b
#define fp13  fpar[12].p_fit
#define dp13  fpar[12].p_p

#define p14   fpar[13].p_b
#define fp14  fpar[13].p_fit
#define dp14  fpar[13].p_p

#define p15   fpar[14].p_b
#define fp15  fpar[14].p_fit
#define dp15  fpar[14].p_p

#define p16   fpar[15].p_b
#define fp16  fpar[15].p_fit
#define dp16  fpar[15].p_p

#define p17   fpar[16].p_b
#define fp17  fpar[16].p_fit
#define dp17  fpar[16].p_p

#define p18   fpar[17].p_b
#define fp18  fpar[17].p_fit
#define dp18  fpar[17].p_p

#define p19   fpar[18].p_b
#define fp19  fpar[18].p_fit
#define dp19  fpar[18].p_p

#define p20   fpar[19].p_b
#define fp20  fpar[19].p_fit
#define dp20  fpar[19].p_p

#define p21   fpar[20].p_b
#define fp21  fpar[20].p_fit
#define dp21  fpar[20].p_p

#define p22   fpar[21].p_b
#define fp22  fpar[21].p_fit
#define dp22  fpar[21].p_p

#define p23   fpar[22].p_b
#define fp23  fpar[22].p_fit
```

```
#define dp23  fpar[22].p_p

#define p24   fpar[23].p_b
#define fp24  fpar[23].p_fit
#define dp24  fpar[23].p_p

#define p25   fpar[24].p_b
#define fp25  fpar[24].p_fit
#define dp25  fpar[24].p_p

#define p26   fpar[25].p_b
#define fp26  fpar[25].p_fit
#define dp26  fpar[25].p_p

#define p27   fpar[26].p_b
#define fp27  fpar[26].p_fit
#define dp27  fpar[26].p_p

#define p28   fpar[27].p_b
#define fp28  fpar[27].p_fit
#define dp28  fpar[27].p_p

#define p29   fpar[28].p_b
#define fp29  fpar[28].p_fit
#define dp29  fpar[28].p_p

#define p30   fpar[29].p_b
#define fp30  fpar[29].p_fit
#define dp30  fpar[29].p_p

#define p31   fpar[30].p_b
#define fp31  fpar[30].p_fit
#define dp31  fpar[30].p_p

#define p32   fpar[31].p_b
#define fp32  fpar[31].p_fit
#define dp32  fpar[31].p_p

#define p33   fpar[32].p_b
#define fp33  fpar[32].p_fit
#define dp33  fpar[32].p_p


#define c1    fpar[33].p_b
#define fc1   fpar[33].p_fit
#define dc1   fpar[33].p_p

#define c2    fpar[34].p_b
#define fc2   fpar[34].p_fit
#define dc2   fpar[34].p_p

#define c3    fpar[35].p_b
#define fc3   fpar[35].p_fit
#define dc3   fpar[35].p_p

#define c4    fpar[36].p_b
```

```
#define fc4  fpar[36].p_fit
#define dc4  fpar[36].p_p

#define c5   fpar[37].p_b
#define fc5  fpar[37].p_fit
#define dc5  fpar[37].p_p

#define c6   fpar[38].p_b
#define fc6  fpar[38].p_fit
#define dc6  fpar[38].p_p

#define c7   fpar[39].p_b
#define fc7  fpar[39].p_fit
#define dc7  fpar[39].p_p

#define c8   fpar[40].p_b
#define fc8  fpar[40].p_fit
#define dc8  fpar[40].p_p

#define c9   fpar[41].p_b
#define fc9  fpar[41].p_fit
#define dc9  fpar[41].p_p

#define c10  fpar[42].p_b
#define fc10 fpar[42].p_fit
#define dc10 fpar[42].p_p

#define c11  fpar[43].p_b
#define fc11 fpar[43].p_fit
#define dc11 fpar[43].p_p


double *parameterP[lastP+1], *parameterC[lastC+1];
double swapP[lastP+1], swapC[lastC+1];   /* The swaps are for the swap function below */


/* setup() is called once when the fit process starts.
 *  Use it for one-time-only code.*/
setup() {
 int i;

        set_prompt(0, "mlayer_wb (? for help)");  /* Main prompt              !!!--!!!*/
        set_prompt(1, "mlayer_wb");  /* Command-file prompt                  !!!--!!!*/

/* These next arrays are pointers to the parameters to make user defined
   functions easier to write (you decide)                        !!!--!!!*/

        parameterP[1]=&p1;
        parameterP[2]=&p2;
        parameterP[3]=&p3;
        parameterP[4]=&p4;
        parameterP[5]=&p5;
        parameterP[6]=&p6;
        parameterP[7]=&p7;
        parameterP[8]=&p8;
        parameterP[9]=&p9;
```

```
        parameterP[10]=&p10;
        parameterP[11]=&p11;
        parameterP[12]=&p12;
        parameterP[13]=&p13;
        parameterP[14]=&p14;
        parameterP[15]=&p15;
        parameterP[16]=&p16;
        parameterP[17]=&p17;
        parameterP[18]=&p18;
        parameterP[19]=&p19;
        parameterP[20]=&p20;
        parameterP[21]=&p21;
        parameterP[22]=&p22;
        parameterP[23]=&p23;
        parameterP[24]=&p24;
        parameterP[25]=&p25;
        parameterP[26]=&p26;
        parameterP[27]=&p27;
        parameterP[28]=&p28;
        parameterP[29]=&p29;
        parameterP[30]=&p30;
        parameterP[31]=&p31;
        parameterP[32]=&p32;
        parameterP[33]=&p33;

        parameterC[1]=&c1;
        parameterC[2]=&c2;
        parameterC[3]=&c3;
        parameterC[4]=&c4;
        parameterC[5]=&c5;
        parameterC[6]=&c6;
        parameterC[7]=&c7;
        parameterC[8]=&c8;
        parameterC[9]=&c9;
        parameterC[10]=&c10;
        parameterC[11]=&c11;

        for (i=firstP; i<=lastP; i++) swapP[i]=0;
        for (i=firstC; i<=lastC; i++) swapC[i]=0;
}

/* In the model equation, you obtain the value of the current point
 *  with the following expressions for the independent variables.
 *  (`M_flag' is 1 when making data, 0 when fitting.) */

#define X  (M_flag? Make_x[0]:dp->d_xx[0])

/* Declare your functions below                        !!!--!!!*/
void calculateReflec(double P[], double C[], double x, double *result);
double ErrFunc1(double y);
double rh(double zz,double DD[],int nlay, double rho0, double sigma);

/* model() returns the value of the model equation at the current
 *  point using the current parameters.  If `deriv_flag' is nonzero,
 *  model() must also calculate the analytic derivative of the model
 *  equation with respect to each parameter that has the `fpar[i].p_fit'
```

```
*  flag set. */

double  model(deriv_flag)
int    deriv_flag;
{
      double yfit, P[lastP+1], C[lastC+1];
          int i;

          for (i=firstP; i<=lastP; i++)
            P[i]=*parameterP[i];

          for (i=firstC; i<=lastC; i++)
            C[i]=*parameterC[i];

          /* Your function here                              !!!--!!!*/
          calculateReflec(P, C, X, &yfit);

          return(yfit);
}
/**************************************************************************/
void calculateReflec(double P[], double C[], double x, double *result)      /* !!!--!!!*/
{
 /*fitref7.5.C
   This program is used to fit a reflection with hundreds of small boxes and several big boxes model.
   Each interface has a different roughness.


   Parameters in GENPLOT "P" array:
   P[1]= the factor of x
   P[2]= the roughness of the first interface(subphase and 1st big box)
   P[3]= the factor of y
   p[4],p[5]= the rho,my of the subphase
   P[6],p[7],p[8],p[9]=the height,my,rho,roughness of the 1st big box
   P[10],p[11],p[12],p[13]=..............................2nd .......
   ...
   ...

   Constants in GENPLOT "C" array:
   c[1]= the number of big boxes
   c[2]= flag (if it is equal to 0, return reflectivity, if it is equal to 1, return electron density)
   c[3]=flag (if c[3] != 0, y=log10(y))
   c[4]=the number of slabs
   c[5]=2*Pi/wavelength (A-1)
   c[6]=flag (if c[6] != 0, y=y/frsnll)
   c[7]=rho for the upper phase
   c[8]=my for the upper phase
    */
 struct cplx f[20000], an[20000], rn[20000], fnmax, f1, rn1;
 double rho[20000], d[20000], my[20000], sig, del[20000], bet[20000], y,l;
 double slu, xsum, theta,theta1, frsnll, qzoff;
 int nmax,nnmax, n, j, i;
 nnmax    =C[1]+2;  /* the number of layers between the water and oil */
 nmax     = C[4] + 2; /*the number of slabs*/
 rho[1]   = C[7];
 my[1]    = C[8];
 d[1]     = 0.0;
```

```
  rho[nmax] = P[4];
  my[nmax]  = P[5];
  d[nmax]   = 0.0;
  qzoff     = C[9];
  slu       = 2.817938e-5;   /* r-e in [AA] */

  if (C[2] == 0.0) {                    /* Refelectivity Calculations */
          if (x<0.5){
          theta1=(x>0.0)? x/(2.0*C[5]):0.0001/(2.0*C[5]);
          x=x+qzoff;
          if (x<=0) x=0.0001;
          theta = x/(2.0*C[5]);
          sig = P[1];
          P[6]=P[14]-P[10];          /*HaoYu  substitute the head group length by the total length*/
}
          if (x>0.49){
          x=x-0.5;
          theta1=(x>0.0)? x/(2.0*C[5]):0.0001/(2.0*C[5]);
          if (x<=0) x=0.0001;
          theta = x/(2.0*C[5]);
          sig = P[2];
          P[6]=P[14]-P[10];   /* Hao Yu, Ability to fit two reflectivity curve together */

}

  if (C[10]==1){         /*fixed roughness*/
    for (i=1;i<=nnmax-2;i++){
      P[4*(i+1)+1]=sig;
}
}
    del[nmax] = slu * 2.0 * 3.14159 / (C[5]*C[5]) * rho[nmax];
    bet[nmax] = .5/C[5]*1.e-8*my[nmax];
    del[1] =  slu * 2.0 * 3.14159 / (C[5]*C[5]) * rho[1];
    bet[1] = 0.0;

    f[nmax] = cplxsqrt(makecplx(theta*theta - 2.0 * (del[nmax]-del[1]),-2.0 * bet[nmax]));


    /*  P[nnmax*4-4]=258/P[nnmax*4-6]/C[10];*/
    /*  P[nnmax*4]=0;*/
    l=0.0;
    f[1]= cplxsqrt(makecplx(theta*theta,-2.0*bet[1]));
    for (j=1;j<=nnmax-2;j++){
     l=l+P[4*j+2];        /*total thickness for mlayers*/
     }
    if (C[1]==0) l=l+8*sig;
    else
     l=l+4*sig+4*P[4*(nnmax-2)+5]; /*total reflectivity calculation length: total thickness for mlayers plus
4*roughness for both sides*/
    for (n=nmax;n>=3;n=n-1) {
     d[n-1]=l/C[4];      /*thinkness for each lab*/
          rho[n-1]=rh((nmax-n+1/2.0)*d[n-1]-4*sig,P,nnmax, rho[1],sig)+rho[nmax]/2.0+rho[1]/2.0;
     my[n-1]=0;

     del[n-1]=slu*2.*3.14159/(C[5]*C[5])*rho[n-1];
     bet[n-1]=.5/C[5]*1.e-8*my[n-1];
```

```
    f[n-1]=cplxsqrt(makecplx(theta*theta-2.0*(del[n-1]-del[1]),-2.0*bet[n-1]));
    }

/* Calculate Fresnel law for subphase-only: */

    fnmax=cplxsqrt(makecplx(theta1*theta1-2.0*(del[nmax]-del[1]),-2.0*bet[nmax]));
    f1 = cplxsqrt(makecplx(theta1*theta1,-2.0*bet[1]));
    rn1= cdiv( cdiff(f1,fnmax),csum(f1,fnmax) );
    frsnll=modulus(rn1)*modulus(rn1);


    rn[nmax]=makecplx(0.0,0.0);

    for (n=nmax; n>=2; n--) {
     an[n-1]=cdiv( cdiff (f[n-1],f[n]),csum(f[n-1],f[n]) );
     rn[n-1]=cmult( cplxexp( cmult(makecplx(0,-2.*C[5]*d[n-1]),f[n-1])), cdiv( csum(rn[n],an[n-
1]),csum(cmult(rn[n],an[n-1]),makecplx(1.0,0) )));
    }



/* Output Of Reflectivity: */

    y = P[3]*modulus(rn[1])*modulus(rn[1]);

    if (C[6] != 0.0) y = y/frsnll;
    if (C[3] != 0.0) y = log10(y);

    *result=y;

    return;
   } /* End of Reflectivity Calculations */

   /* Real Space (Rho vs. X=Height: */

  if (C[2] == 1) {   /* SMAEARING */
   if (C[11]==1) {
     sig=0.001;
      for (i=1;i<=nnmax-2;i++){
     P[4*(i+1)+1]=0.001;
}
}
    *result=rh(x,P,nnmax, rho[1], P[1])+rho[nmax]/2.+rho[1]/2.;
    return;
     }
}
double rh(double zz, double DD[],int nlay,double rho0, double sigma) {
 double xx[10],xy[10],rsum,zx;
 int i,j;
   xy[1]=zz/sigma;
   xx[1]=0;
   for (j=2; j<=nlay-1; j++) {
    for (i=2; i<=j; i++) {
    xx[i] =xx[i-1]+ DD[4*i-2];
    }
    xy[j]=(zz-xx[j])/DD[4*j+1];
```

```
    }
   rsum=0.0;
    DD[nlay*4]=rho0;
    /*   DD[nlay*4-4]=258.0/DD[28]/DD[nlay*4-6];*/
   for (j=nlay-1; j>=1; j--) {
     zx = xy[nlay-j];
     rsum = rsum + ErrFunc1(zx) * (DD[(nlay-j)*4]-DD[(nlay-j+1)*4]);
    }

   return  rsum;
}


/********************************************************************************
Error function definition from Abramowitz and Segun page 299 7.1.25 */

double ErrFunc1(double y)
{
  double yx, sgn, tx, zx;

  yx=sqrt(y*y)/sqrt(2.);
  sgn=1.0;

  if (y <= 0.0) sgn=-1.;

  tx=1./(1. + .47047*yx);
  zx= 1.-(.34802*tx-.0958798*tx*tx+.7478556*tx*tx*tx)*exp(-yx*yx);
  zx =-0.5*sgn*zx;

  return zx;
}
/*

int initParam();
int setParam();
int newhelp();
int saveParam();
int varyParam();
void toggle(int *param, char name[]);
int whatParam();
int prefilter();
int postfilter();
int revert();
int saveRho();
int swapParams();
char swapPage=0;

struct  user_cmds {
        char    c_one;          /* The first letter of the command */
        char    c_two;          /* The second letter (or 0) */
        int     (*c_func)();        /* The name of the function */
} user_cmds[] = {
{ 'i', 'p', initParam },
        { 'l', 't', setParam },
        { '?', '\0', newhelp },
        { 'S', 'P', saveParam },
        { 'v', 'a', varyParam },
```

```
            { 'p', '\0', whatParam },
            {'e', '1', CreateCmdFile},
            {'e', '2', ReadCh},
            0,                  /* must be terminated with a zero */
};

/*****************************************************************************/
int swapParams()
{
  int i;
  double dummyP[lastP+1], dummyC[lastC+1];

  if (swapPage==0) {

    for (i=firstP; i<=lastP; i++) {
      dummyP[i]=*parameterP[i];
      *parameterP[i]=swapP[i];
      swapP[i]=dummyP[i];
    }

    for (i=firstC; i<=lastC; i++) {
      dummyC[i]=*parameterC[i];
      *parameterC[i]=swapC[i];
      swapC[i]=dummyC[i];
    }
    swapPage=1;
    printf("Parameters <--> Swap\n");
  } else {

    for (i=firstP; i<=lastP; i++) {
      dummyP[i]=swapP[i];
      swapP[i]=*parameterP[i];
      *parameterP[i]=dummyP[i];
    }

    for (i=firstC; i<=lastC; i++) {
      dummyC[i]=swapC[i];
      swapC[i]=*parameterC[i];
      *parameterC[i]=dummyC[i];
    }
    swapPage=0;
    printf("Swap <--> Parameters\n");
  }
}

/*****************************************************************************/
int saveRho()
{
  FILE * of;
  char *cmd = get_cmdbuf();  /* A pointer to the commmand buffer used to call the function */
  char fileName[255]="parameters.dat";
  int i;
  double dummy[10];

  if (strlen(cmd)>3)  /* There must be a file name typed */
    sscanf(cmd, "ro %s", fileName);
```

```
      else
        get_snum("What is the file name to save parameters to", fileName);

      of = fopen(fileName, "w");

      if (!of) {
        printf("There was an error opening the file %s!\n", fileName);
        return 0;
      }

      fprintf(of, "# This file (%s) created by fitref7.5\n\n", fileName);
      fprintf(of, "# Begin parameter list\n\n");

      dummy[0]=*parameterP[7];
      *parameterP[7] = (*parameterC[9]+*parameterP[10]*10)/(dummy[0] * *parameterP[6]);
      dummy[1]=*parameterP[10];
      *parameterP[10] = *parameterC[10]/(dummy[0] * *parameterP[9]);
      dummy[2]=*parameterP[13];
      *parameterP[13] = *parameterC[11]/(dummy[0] * *parameterP[12]);

      for (i=firstP; i<=lastP; i++)
        fprintf(of, "P[%d]=%lf\n", i, *parameterP[i]);

      for (i=firstC; i<=lastC; i++)
        fprintf(of, "C[%d]=%lf\n", i, *parameterC[i]);

      fprintf(of, "\n# End parameter list\n\n# End file\n");

      *parameterP[7] = dummy[0];
      *parameterP[10] = dummy[1];
      *parameterP[13] = dummy[2];

      fclose(of);
      printf("Parameters wrote to file:  %s\n", fileName);
      return 0;
    }

/*****************************************************************************/
int revert()
{
    FILE *inf;
    char ch, dummy;
    int n;      /* The array index */
    float val;  /* The array value */

    if (!strcmp(revertFileName, "-99")) {
      printf("You cannot revert without opening a file first!\n");
      return 0;
    }

    inf = fopen(revertFileName, "r");

    if (!inf) {
      fprintf(stderr,"There was an error opening the file %s!\n", revertFileName);
      return 0;
    }
```

```
  do {
    ch=fgetc(inf);
    switch (toupper(ch)) {
    case '#':                    /* Ignore comment lines */
          do { dummy=fgetc(inf); } while (dummy!='\n' && dummy!=EOF);
          break;
    case 'P':                    /* This is the parameter P */
          while (fgetc(inf)!='[');     /* Skip all characters until a [ is reached */
          fscanf(inf, "%d", &n);         /* The array index */

          while (fgetc(inf)!='=');       /* Skip all characters until an = is reached */
          fscanf(inf, "%f", &val);       /* The array value */

          if (n>=firstP && n<=lastP)
            *parameterP[n]=val;
          break;

    case 'C':
          while (fgetc(inf)!='[');     /* Skip all characters until a [ is reached */
          fscanf(inf, "%d", &n);          /* The array index */

          while (fgetc(inf)!='=');       /* Skip all characters until an = is reached */
          fscanf(inf, "%f", &val);        /* The array value */

          if (n>=firstC && n<=lastC)
            *parameterC[n]=val;
          break;

    default:                     /* Ignore any other characters */
      break;
    }
  } while (ch!=EOF);      /* Continue until the end of file marker */

  fclose(inf);
  printf("Parameters read from file:  %s\n", revertFileName);
  return 0;
}

/*****************************************************************************/
int prefilter()
{
  register int i;
  register struct f_data *d;

  for (d = f_data, i = 0; i < npts; i++, INC(d)) {
    d->d_y = log10(d->d_y);
  }
}

/*****************************************************************************/
int postfilter()
{
  register int i;
  register struct f_data *d;
```

```c
  for (d = f_data, i = 0; i < npts; i++, INC(d)) {
    d->d_y = pow(10,d->d_y);
  }
}

/*****************************************************************************/
int whatParam()
{
  char *cmd = get_cmdbuf(); /* A pointer to the commmand buffer used to call the function */
  char par, name[21];
  int i, n, len, vary;
  double val;

  if ((len=strlen(cmd))>2) { /* There must be a parameter name typed */
    for (i=2; i<=len && i<20; i++)
      name[i-2] = cmd[i];     /* Copy the cmdline to the name array */
    name[i+1]='\0';
  } else {
    strcpy(name, "c(1)");

    printf("\nYou MUST use the following format:  p[n] or p(n).");
    printf("\n     Where n is a number and p is the parameter.");

    get_snum("What is the parameter name in question", name);
  }

  name[0]=toupper(name[0]);

  if (name[1]=='[') sscanf(name, "%c[%d", &par, &n);
  if (name[1]=='(') sscanf(name, "%c(%d", &par, &n);

/* There needs to be a case statement for every parameter (i.e. case 0
     corresponds to P(0)                                !!!--!!! */

  switch (par) {
  case 'P':                              /* This is the parameter P */
    if (n>=firstP && n<=lastP) {
      val=*parameterP[n];
      switch (n) {
        case 1: vary=fp1; break;
        case 2: vary=fp2; break;
        case 3: vary=fp3; break;
        case 4: vary=fp4; break;
        case 5: vary=fp5; break;
        case 6: vary=fp6; break;
        case 7: vary=fp7; break;
        case 8: vary=fp8; break;
        case 9: vary=fp9; break;
            case 10: vary=fp10; break;
        case 11: vary=fp11; break;
            case 12: vary=fp12; break;
            case 13: vary=fp13; break;
        case 14: vary=fp14; break;
            case 15: vary=fp15; break;
            case 16: vary=fp16; break;
        case 17: vary=fp17; break;
```

```
        case 18: vary=fp18; break;
        case 19: vary=fp19; break;
      case 20: vary=fp20; break;
        case 21: vary=fp21; break;
        case 22: vary=fp22; break;
      case 23: vary=fp23; break;
        case 24: vary=fp24; break;
        case 25: vary=fp25; break;
      case 26: vary=fp26; break;
        case 27: vary=fp27; break;
        case 28: vary=fp28; break;
        case 29: vary=fp29; break;
        case 30: vary=fp30; break;
      case 31: vary=fp31; break;
        case 32: vary=fp32; break;
        case 33: vary=fp33; break;
      }
    } else
      printf("I don't recognize or use %s.  Reason: Wrong index value.\n", name);
    break;

/* There needs to be a case statement for every parameter (i.e. case 1
   corresponds to C(1)                               !!!--!!! */

  case 'C':
    if (n>=firstC && n<=lastC) {
     val=*parameterC[n];
     switch (n) {
      case 1: vary=fc1; break;
      case 2: vary=fc2; break;
      case 3: vary=fc3; break;
      case 4: vary=fc4; break;
      case 5: vary=fc5; break;
      case 6: vary=fc6; break;
      case 7: vary=fc7; break;
      case 8: vary=fc8; break;
      case 9: vary=fc9; break;
      case 10: vary=fc10; break;
      case 11: vary=fc11; break;
     }
    } else
      printf("I don't recognize or use %s.  Reason: Wrong index value.\n", name);
    break;

  default:
     printf("I don't recognize or use %s.  Reason: Unrecognizable parameter.\n", name);
     break;
   }

 printf("\n%c[%d]=%lf  %s\n", par, n, val, (vary==0)?"Constant":"Fit");
 return 0;
}

/*****************************************************************************/
int varyParam()
{
```

```
char *cmd = get_cmdbuf();  /* A pointer to the commmand buffer used to call the function */
char name[21], par;
int n, i, len;

if ((len=strlen(cmd))>3) {   /* If length > 3 the user must have type a parameter into cmd */
  for (i=3; i<=len && i<20; i++)
    name[i-3] = cmd[i];     /* Copy the cmdline to the name array */
  name[i+1]='\0';

} else {
  strcpy(name, "i.e. c(1)");

  printf("\nYou MUST use the following format:  p[n] or p(n).");
  printf("\n     Where n is a number and p is the parameter.");

  if (!get_snum("\nWhat is the parameter to toggle", name)) {
    printf("\nNo parameters toggled.\n");
    return 0;
  }
}

name[0]=toupper(name[0]);

if (name[1]=='[') sscanf(name, "%c[%d", &par, &n);
if (name[1]=='(') sscanf(name, "%c(%d", &par, &n);

/* There needs to be a case statement for every parameter (i.e. case 0
    corresponds to P(0)                                   !!!--!!! */

switch (par) {
case 'P':                           /* This is the parameter P */
   switch (n) {
     case 1: toggle(&fp1, name); break;
     case 2: toggle(&fp2, name); break;
     case 3: toggle(&fp3, name); break;
     case 4: toggle(&fp4, name); break;
     case 5: toggle(&fp5, name); break;
     case 6: toggle(&fp6, name); break;
     case 7: toggle(&fp7, name); break;
     case 8: toggle(&fp8, name); break;
     case 9: toggle(&fp9, name); break;
         case 10: toggle(&fp10, name); break;
     case 11: toggle(&fp11, name); break;
         case 12: toggle(&fp12, name); break;
         case 13: toggle(&fp13, name); break;
     case 14: toggle(&fp14, name); break;
         case 15: toggle(&fp15, name); break;
         case 16: toggle(&fp16, name); break;
     case 17: toggle(&fp17, name); break;
         case 18: toggle(&fp18, name); break;
         case 19: toggle(&fp19, name); break;
     case 20: toggle(&fp20, name); break;
         case 21: toggle(&fp21, name); break;
         case 22: toggle(&fp22, name); break;
     case 23: toggle(&fp23, name); break;
         case 24: toggle(&fp24, name); break;
```

```
        case 25: toggle(&fp25, name); break;
      case 26: toggle(&fp26, name); break;
        case 27: toggle(&fp27, name); break;
        case 28: toggle(&fp28, name); break;
        case 29: toggle(&fp29, name); break;
        case 30: toggle(&fp30, name); break;
      case 31: toggle(&fp31, name); break;
        case 32: toggle(&fp32, name); break;
        case 33: toggle(&fp33, name); break;
        default:
          printf("I don't recognize or use %s.  Reason: Wrong index value.\n", name);
          break;
    }
    break;

/* There needs to be a case statement for every parameter (i.e. case 1
   corresponds to C(1)                              !!!--!!! */

  case 'C':
    switch (n) {
        case 1: toggle(&fc1, name); break;
        case 2: toggle(&fc2, name); break;
        case 3: toggle(&fc3, name); break;
        case 4: toggle(&fc4, name); break;
        case 5: toggle(&fc5, name); break;
        case 6: toggle(&fc6, name); break;
        case 7: toggle(&fc7, name); break;
        case 8: toggle(&fc8, name); break;
        case 9: toggle(&fc9, name); break;
        case 10: toggle(&fc10, name); break;
        case 11: toggle(&fc11, name); break;
        default: printf("I don't recognize or use %s.  Reason: Wrong index value.\n", name); break;
        }
    break;
  default:
    printf("I don't recognize or use %s.  Reason: Unrecognizable parameter.\n", name);
    break;
  }
  return 0;
}

/*****************************************************************************/
void toggle(int *param, char name[])
{
 if (*param) {
   *param=0;
   printf("\n%s toggled from fit to constant.\n", name);
 } else {
   *param=1;
   printf("\n%s toggled from constant to fit.\n", name);
 }
}

/*****************************************************************************/
int saveParam()
{
```

```
  FILE * of;
  char *cmd = get_cmdbuf();  /* A pointer to the commmand buffer used to call the function */
  char fileName[255]="parameters.dat";
  int i;
  double P[35], C[10];

  if (strlen(cmd)>3)  /* There must be a file name typed */
    sscanf(cmd, "SP %s", fileName);
  else
    get_snum("What is the file name to save parameters to", fileName);

  of = fopen(fileName, "w");

  if (!of) {
    printf("There was an error opening the file %s!\n", fileName);
    return 0;
  }

  fprintf(of, "# This file (%s) created by fitref7.5\n\n", fileName);
  fprintf(of, "# Begin parameter list\n\n");

  for (i=firstP; i<=lastP; i++)
    fprintf(of, "P[%d]=%lf\n", i, *parameterP[i]);

  for (i=firstC; i<=lastC; i++)
    fprintf(of, "C[%d]=%lf\n", i, *parameterC[i]);

  fprintf(of, "\n# End parameter list\n\n# End file\n");

  fclose(of);
  printf("Parameters wrote to file:  %s\n", fileName);
  return 0;
}

/*****************************************************************************/
int newhelp()
{
  printf("\nFunctions That Have Been Added to C-Plot:\n");
  printf("\n\tip - Initialize Parameters:  Reads the parameters from a file.");
  printf("\n\tSP - Save Parameters:  Saves the parameters to a file readable by ip.");
  printf("\n\tlt - Let:  Changes the value of a parameter.");
  printf("\n\tva - Vary Parameter:  Toggles the vary flag for a parameter.");
  printf("\n\tp  - Print Parameter:  Prints a parameter's value and vary flag.");
  printf("\n\t?  - Help:  Displays this help screen.");
  printf("\n\tpr - Prefilter:  Calculates the log10 of the data.");
  printf("\n\tpo - Postfilter:  Undoes the prefilter.");
  printf("\n\tre - Revert:  Reverts to last parameter file opened with ip.");
  printf("\n\tro - Rho: Save parameters to an electron-density parameter file.");
  printf("\n\tsw - Swap: Swaps the current parameters with a buffer.\n");

  printf("\nSome Useful C-Plot Functions:\n");
  printf("\n\tfi - Fit the data points.");
  printf("\n\tpg - Get the data points.");
  printf("\n\tps - Send the data points to plot.");
  printf("\n\tmd - Make data and send to plot.");
  printf("\n\tmr - Make residuals.");
```

```
  printf("\n\tsp - Save/show parameters.");
  printf("\n\twt - Select how to weight the data.\n\n");

  return 0;
}

/*****************************************************************************/
int setParam()
{
 char *cmd = get_cmdbuf();  /* This is a pointer to the command line */
 char name[21]="\0", par;
 double val;
 int n, i, len;

 if ((len=strlen(cmd))>3) {   /* If length > 3 the user must have type a parameter into cmd */

   for (i=3; i<=len && i<20; i++)
     name[i-3] = cmd[i];     /* Copy the cmdline to the name array */
   name[i+1]='\0';

 } else {
   strcpy(name, "i.e. C[7]=4.0");

   printf("\nYou MUST use the following format:  p[n]=val or p(n)=val.");
   printf("\n     Where p is the parameter, n is the index number, and val is the value.");
   printf("\n     IMPORTANT:  Do not add any spaces or other characters.");

   if (!get_snum("\nCommand string", name)) {
     printf("\nNo values changed.\n");
     return 0;
   }
 }

 name[0] = toupper(name[0]);

 if (name[1]=='[') sscanf(name, "%c[%d]=%lf", &par, &n, &val);
 if (name[1]=='(') sscanf(name, "%c(%d)=%lf", &par, &n, &val);

 switch (par) {
 case 'P':                              /* This is the parameter P */
  if (n>=firstP && n<=lastP)
    *parameterP[n]=val;
  else
    printf("I don't recognize or use %s.  Reason: Wrong index value.\n", name);
  break;

 case 'C':
  if (n>=firstC && n<=lastC)
    *parameterC[n]=val;
  else
    printf("I don't recognize or use %s.  Reason: Wrong index value.\n", name);
  break;

 default:
    printf("I don't recognize or use %s.  Reason: Unrecognizable parameter.\n", name);
    break;
```

```c
    }

  printf("\n%c[%d]=%lf\n", par, n, val);
  return 0;
}

/*****************************************************************************/
int initParam()
{
 FILE *inf;
 char *cmd = get_cmdbuf();
 char ch, dummy, PfileName[255]="defaultparameters.dat";
 int n;     /* The array index */
 float val;   /* The array value */

 if (strlen(cmd)>3)  /* There must be a file name typed */
   sscanf(cmd, "ip %s", PfileName);
 else
  get_snum("Name of the parameter file to load", PfileName);

 inf = fopen(PfileName, "r");

 if (!inf) {
  fprintf(stderr,"There was an error opening the file %s!\n", PfileName);
  return 0;
 }

 strcpy(revertFileName, PfileName);

 do {
  ch=fgetc(inf);
  switch (toupper(ch)) {
  case '#':                  /* Ignore comment lines */
        do { dummy=fgetc(inf); } while (dummy!='\n' && dummy!=EOF);
        break;
  case 'P':               /* This is the parameter P */
        while (fgetc(inf)!='[');      /* Skip all characters until a [ is reached */
        fscanf(inf, "%d", &n);         /* The array index */

        while (fgetc(inf)!='=');        /* Skip all characters until an = is reached */
        fscanf(inf, "%f", &val);        /* The array value */

        if (n>=firstP && n<=lastP)
          *parameterP[n]=val;
        break;

   case 'C':
        while (fgetc(inf)!='[');       /* Skip all characters until a [ is reached */
        fscanf(inf, "%d", &n);          /* The array index */

        while (fgetc(inf)!='=');        /* Skip all characters until an = is reached */
        fscanf(inf, "%f", &val);        /* The array value */

        if (n>=firstC && n<=lastC)
          *parameterC[n]=val;
        break;
```

```
      default:                        /* Ignore any other characters */
        break;
      }
  } while (ch!=EOF);       /* Continue until the end of file marker */

  fclose(inf);
  printf("Parameters read from file:  %s\n", PfileName);
  return 0;
}
```

Appendix D   Parratt Fitting Function for Reflectivity from cPLA2α-C2 bound to SOPC monolayer

This program is used to fit the X-ray reflectivity data with 2-slab lipid model plus crystal structure of cPLA2α-C2. One slab is head group layer of the lipid which contains the lipid head group, water molecules and residuals of cPLA2α-C2 penetrate into the head group; the other slab is the tail group of the lipid and the DCE molecules and esiduals of cPLA2α-C2 among the hydrocarbon chains. The first step of using this program is to calculate the electron profile of the cPLA2α-C2 based on its crystal structure from Protein Data Bank.[12] The combined electron density profile of the model is convoluted by a Gaussian function with interfacial roughness as width. The convoluted electron density profile is cut into slices and Parratt algorithm has been applied to calculate the reflectivity. There are 7 parameters used to describe the electron profile of the interface are fitted in the program as follow:

roughness: the interfacial roughness

tail(1), rhotail: the thickness and electorn density of the tail group layer

head(2), rhohead: the thickness and electorn density of the head group layer

 PEN: the penetration of the protein into the lipid monolayer

cov(cov=0 lipid only): the coverage of the protein onto the lipid monolayer

There are also constants to represent the characteristics of the system.

QC : Critical angle of the system

lambda : Wavelength of the incident X-ray.

e step size : Step size to cut the electron density profile of the model for Parrat Reflectivity Calculation

The following program is written based on the basic script of CPLOT (Certified Scientific Software, Cambridge, Massachusetts).

```
/** Adjust the following 4 parameters for the size of your problem. **/
#define NUM_XS  1      /* The number of independent variables (no limit) */
#define MAXPAR  16      /* The number of parameters */
#define MAXPTS  1024   /* The most points for fitting */
#define MAXPLT  1024   /* In-core points for plot (pg, ps, md, mr and sA) */
#define slice   3000   /* total layers in this system */
#define Re     2.814e-5 /* classical electron radius */
```

```
#include <string.h>
#include <stdio.h>
#include <math.h>
#include <p_fitsize.h>
#include "parse.c"
#include "erf.c"
#include "complex.c"
#include "error.h"
#include <stdio.h>


/**
* The title is printed when the fit process starts and with the `V' command.
**/
char    *title = "Fit protein-lipid system";

/**
* The comment is added to the sF output file.
**/
char    *comment = "";

/**
* setup() is called once when the fit process starts.
* Use it for one-time-only code.
**/
FILE  *infile,*rdfile  ;
char   edfile[50]=" ",line[12]=" ";
double pz[slice]={0.0},epro[slice]={0.0}, eprobuf[slice]={0.0};
double thickness;
double edens[slice]={0.0},dlay[slice]={0.0},ddlay[slice]={0.0},dedens[slice]={0.0};
int    i,slicepro,in;




setup() {
        /*
        * Shown is optional user initialization of prompts.
        * Second argument must point to static storage.
        */
        set_prompt(0, "Protein");  /* Main prompt */
        set_prompt(1, "protein");  /* Command-file prompt */

        if(slicepro==0)
      {
       printf("enter the file name of input edfiles :\n") ;
       scanf("%s",&edfile) ;

       if((infile=fopen(edfile,"r"))==NULL)
        {fprintf(stderr,"no such file\n") ;
            exit(1) ;}
          }
        if(fgets(line,12,infile)!=NULL)
      line[12]='\0' ;
```

```
        printf("%s\n",line) ;
        rdfile=fopen(line,"r") ;

i= 0;
while(!feof(rdfile))
    { i=i+1 ;
      fscanf(rdfile,"%lf%lf%lf\n",&pz[i],&epro[i],&eprobuf[i]);

      printf("%d  %f  %f   %f\n",i,pz[i],epro[i],eprobuf[i]) ;
    }
thickness=fabs(pz[1]-pz[2]) ;
slicepro=i ;
fclose(rdfile) ;
}


/**
 * Indicate for each parameter:
 *   o The parameter name,
 *   o Whether you provide the analytic-derivative (1=yes, 0=no),
 *   o Whether to fit (as the initial default),
 *   o The default initial value of the parameter.
 * These next three are optional, and can be modified while running:
 *   o Whether to constrain the parameter within limits.  If set to 1,
 *     constrain lower; if 2, constrain upper; if 3, constrain both.
 *   o The lower constraint
 *   o The upper constraint
 **/
struct init_4 initial[] = {
     /* Name          Deriv?    Fit?    Initial    Limit?    Low     High */

 {"rho(0),R/Rf(1)    ",   0,       0,       1,        0,      0,      0,  },
     { "pp(< 0)     ",   0,       1,      -8.4,       3,    -15.0,   -3.0,  },

 {"cov(cov=0 lipid only)",   0,       1,      0.6,       3,     0.0,    1.0,  },

     { "tail(1)    ",   0,       1,      14.0,      3,      10,     19.0  },

     { "head(2)    ",   0,       1,      8.0,       3,      5.0,    12.0, },

     { "rhotail    ",   0,       1,      0.31,      3,      0.27,   0.35, },

     { "rhohead    ",   0,       1,      0.42,      3,      0.37,   0.48, },

     { "QC         ",   0,       0,      0.00795,   3,      0.0,    100.0, },

     { "lambda     ",   0,       0,      0.413,     3,      0.0,    100.0, },

     { "roughness  ",   0,       1,      8,         3,      7.6,    9.5, },

     { "topphase   ",   0,       0,      0.3796,    3,      0.0,    1000.0, },

     { "botphase   ",   0,       0,      0.334,     3,      0.0,    100.0, },

     { "e step size ",   0,       0,      0.2,       3,      0.0,    0.0, },
      {"putindex(1:read file)" ,   0,       0,      1.0,       3,      0.0,    1.0, },
```

```
      { "Q offset ",     0,       1,      0.001,      3,     -0.002,     0.002, },
      { "PEN ",      0,      1,     -8.4,      3,     -15.0,     -3.0, },

};

#define X (M_flag? Make_x[0]:dp->d_xx[0])
/**
*  Refer to the parameters using the following structure members:
*
*  fpar[i].p_b   - The current value of the parameter.
*  fpar[i].p_fit - When non-zero, the parameter is being fit.
*  fpar[i].p_p   - Assign analytic derivative to this.
*
*  `p_fit' and `p_p' are only relevant for parameters that have the
*  analytic-derivative flag set.
*  The following `defines' may be useful.
**/
#define TYPE        fpar[0].p_b
#define pp          fpar[1].p_b
#define cov         fpar[2].p_b
#define tail        fpar[3].p_b
#define head        fpar[4].p_b
#define rhotail     fpar[5].p_b
#define rhohead     fpar[6].p_b
#define QC          fpar[7].p_b
#define lambda      fpar[8].p_b
#define roughness   fpar[9].p_b
#define topphase    fpar[10].p_b
#define botphase    fpar[11].p_b
#define esize       fpar[12].p_b
#define putindex    fpar[13].p_b
#define Qoffset     fpar[14].p_b
#define PEN         fpar[15].p_b
#define TWOPI       6.28318531
#define SQTTWOPI    2.50662828
#define sr2         1.41421356


int ed1(int y,double pz[],const double epro[],
        const double eprobuf[],double dlay[],double edens[])
{ int i,j ;
 pp=-(tail+head+PEN);
 edens[1]=rhotail ;
 dlay[1]=-pp ;
 pz[0]=0.0 ;
 pz[1]=pp ;
 if(pp==0.0) j=0 ;
 else j=1 ;
 for(i=1;i<=y;i++)
   {pz[i+j]=pp-i*thickness ;
    dlay[i+j]=thickness ;
   if(pz[i+j-1]>(-tail)&&pz[i+j]<(-tail))
     {pz[i+j+1]=pz[i+j] ;
      pz[i+j]=-tail ;
      dlay[i+j]=pz[i+j-1]-pz[i+j] ;
      edens[i+j]=cov*epro[i]+rhotail ;
```

```
      dlay[i+j+1]=pz[i+j]-pz[i+j+1] ;
      edens[i+j+1]=cov*epro[i]+rhohead ;
      j=j+1 ;}

   else if(pz[i+j-1]>-(tail+head)&&pz[i+j]<-(tail+head))
     {pz[i+j+1]=pz[i+j] ;
      pz[i+j]=-(tail+head) ;
      dlay[i+j]=pz[i+j-1]-pz[i+j] ;
      edens[i+j]=cov*epro[i]+rhohead ;
      dlay[i+j+1]=pz[i+j]-pz[i+j+1] ;
      edens[i+j+1]=cov*eprobuf[i]+(1.0-cov)*botphase ;
      j=j+1 ;}
   else
     { if(pz[i+j]>=(-tail)) edens[i+j]=cov*epro[i]+rhotail ;
       else if(pz[i+j]<(-tail)&&pz[i+j]>=(-tail-head))
          edens[i+j]=cov*epro[i]+rhohead ;
       else edens[i+j]=cov*eprobuf[i]+(1.0-cov)*botphase ;
     }
    }


 if(pz[y+j]>=(-tail))
   {dlay[y+j+1]=pz[y+j]+tail;pz[y+j+1]=-tail; edens[y+j+1]=rhotail ;
    dlay[y+j+2]=head ;pz[y+j+2]=-(tail+head) ;edens[y+j+2]=rhohead ;
    y=y+j+2 ;}
 else if(pz[y+j]==(-tail))
   {dlay[y+j+1]=head; pz[y+j+1]=-(tail+head) ; edens[y+j+1]=rhohead ;
    y=y+j+1 ;}
 else if(pz[y+j]<(-tail)&&pz[y+j]>-(tail+head))
   {dlay[y+j+1]=pz[y+j]+tail+head;pz[y+j+1]=-(tail+head);
    edens[y+j+1]=rhohead ;y=y+j+1 ;}
 else y=y+j ;
 return (y) ;
}


int ed2(int y,double pz[],const double epro[],
      const double eprobuf[],double dlay[],double edens[])
{ int i,j ;
 pp=-(tail+head+PEN);
 edens[1]=rhotail ;
 dlay[1]=tail ;
 pz[0]=0.0 ;
 pz[1]=-tail ;
 pz[2]=pp ;
 edens[2]=rhohead ;
 if(pp==(-tail)) j=1 ;
 else j=2 ;
 for(i=1;i<=y;i++)
   {pz[i+j]=pp-i*thickness ;
    dlay[i+j]=thickness ;

   if(pz[i+j-1]>-(tail+head)&&pz[i+j]<-(tail+head))
     {pz[i+j+1]=pz[i+j] ;
      pz[i+j]=-(tail+head) ;
      dlay[i+j]=pz[i+j-1]-pz[i+j] ;
```

```
        edens[i+j]=cov*epro[i]+rhohead ;
        dlay[i+j+1]=pz[i+j]-pz[i+j+1] ;
        edens[i+j+1]=cov*eprobuf[i]+(1.0-cov)*botphase ;
        j=j+1 ;}
      else
       {if(pz[i+j]>=(-tail-head))
         edens[i+j]=cov*epro[i]+rhohead ;
        else edens[i+j]=cov*eprobuf[i]+(1.0-cov)*botphase ;}


      }

   if(pz[y+j]>-(tail+head))
     {dlay[y+j+1]=pz[y+j]+tail+head ;pz[y+j+1]=-(tail+head) ;edens[y+j+1]=rhohead ;
      y=y+j+1 ;}

   else y=y+j ;
   return (y) ;
 }



 int ed3(int y,double pz[],const double epro[],
       const double eprobuf[],double dlay[],double edens[])
 { int i,j ;
   pp=-(tail+head+PEN);
 edens[1]=rhotail ;
   dlay[1]=tail ;
   pz[0]=0.0 ;
   pz[1]=-tail ;
   pz[2]=-(tail+head) ;
   edens[2]=rhohead ;
   dlay[2]=head ;
   edens[3]=botphase ;
   pz[3]=pp ;
   dlay[3]=-pp+pz[2] ;

   if(pp==-(tail+head)) j=2 ;
   else j=3 ;
   for(i=1;i<=y;i++)
    {pz[i+j]=pp-i*thickness ;
     dlay[i+j]=thickness ;
     edens[i+j]=cov*eprobuf[i]+(1.0-cov)*botphase ;}
   y=y+j ;
  return (y) ;
 }



 double eshape(const int totlay,double za,const double pz[],const double edens[])
 { int j;
  double chem,zmin,zmax ;
  if(roughness>0)
         {chem=0.0 ;
          chem=chem+(edens[0]/2.0)*erfc((pz[0]-za)/(roughness*sr2)) ;
          for(j=1;j<=totlay;j++)
              {zmin=pz[j]-za ; zmax=pz[j-1]-za ;
                 chem=chem+(edens[j]/2.0)*(erf(zmax/(roughness*sr2))-erf(zmin/(roughness*sr2))) ;}
```

```
                zmax=pz[totlay]-za ;
                chem=chem+(edens[totlay+1]/2.0)*(1.0+erf(zmax/(roughness*sr2))) ;
                    return(chem);
                    }
         else /*roughness=0*/
            {chem=0.0 ;
                if(za>=pz[totlay]&&za<pz[0])
                  {for(j=1;j<=totlay;j++)
                       {if(za>=pz[j]&&za<pz[j-1])
                        {chem=edens[j];
                              j=totlay+1 ;}
                     }
                     }

                else if(za>=pz[0])
                       chem=edens[0] ;

                else
                 chem=edens[totlay+1] ;

                return(chem) ;
            }
         }
         int deshape(const int totlay,const double pz[],const double edens[],
                 double ddlay[], double dedens[])
         {  int j,k,p ;
           double chem,za,dz,zmin,zmax ;
                k=(pz[0]-pz[totlay]+12.0*roughness)/esize ; /*adjust esize depedening on the roughness*/
                dz=(pz[0]-pz[totlay]+12.0*roughness)/(k+1) ;/*6 folds roughness extend 20 in each bulk total 12*/
                for(p=1;p<=(k+1);p++)
                      {ddlay[p]=dz ;
                       za=pz[0]+6.0*roughness-p*dz ;
                    chem=0.0 ;
                    zmin=pz[0]-za ;
                    chem=chem+(edens[0]/2.0)*erfc(zmin/(roughness*sr2)) ;

                    for(j=1 ;j<=totlay;j++)
                      {zmin=pz[j]-za; zmax=pz[j-1]-za ;
                              chem=chem+(edens[j]/2.0)*(erf(zmax/(roughness*sr2))-erf(zmin/(roughness*sr2))) ;}

                    zmax=pz[totlay]-za ;
                    chem=chem+(edens[totlay+1]/2.0)*(1.0+erf(zmax/(roughness*sr2))) ;

                    if(za==0&&roughness==0) chem=topphase ;

                        /* dedens[p]=chem ;*/
                        dedens[k+1-p+1]=chem ;  /*upside down*/
                        /* printf("p=%d,za=%f,th=%f,de=%f\n",p,za,ddlay[p],dedens[p]) ;*/
                    }
                      dedens[0]=botphase ;
                    dedens[k+1+1]=topphase ;
           return (k+1) ;
         }
```

```
fcomplex fresnel( q1, q2)
fcomplex q1,q2 ;

                {return (Cdiv(Csub(q1,q2),Cadd(q1,q2))) ;}


fcomplex qcor(double qz, double rho)
        {
                qz=qz+Qoffset;
        return (Csqrt(Complex(qz*qz-8.0*TWOPI*(rho-botphase)*Re,0.0))) ;}


fcomplex qcor1(double qz, double rho)
        {
        return (Csqrt(Complex(qz*qz-8.0*TWOPI*(rho-botphase)*Re,0.0))) ;}


/*fcomplex intface( q3, q4)
fcomplex q3,q4 ;
{return (Cexp(RCmul(-3.3*3.3/2.0,Cmul(q3,q4)))) ;}*/


double parratt(double qz,const int dj,const double dedens[],const double ddlay[])
{
 fcomplex R,n1,n2,d1,rone,phase,reff,qj,qjp1;
 fcomplex qa,qb,Rf ;
 double norm,RR ;
 int j ;

 rone=Complex(1.0,0.0) ;
 qa=qcor1(qz,dedens[0]) ;
 qb=qcor1(qz,dedens[dj+1]) ;
 Rf=fresnel(qa,qb) ;
 norm=Cabs(Rf) ;
 norm=norm*norm ;

 R=fresnel(qcor(qz,dedens[dj]),qcor(qz,dedens[dj+1])) ;
 qj=qcor(qz,dedens[dj]) ;
 for(j=dj;j>=1;j--)
   {
   qjp1=qcor(qz,dedens[j-1]) ;
   reff=fresnel(qjp1,qj) ;
   phase=Cexp(Cmul(qj,Complex(0.0,ddlay[j]))) ;
   n1=Cmul(R,phase) ;
   R=Cdiv(Cadd(reff,n1),Cadd(rone,Cmul(reff,n1)));
   qj=qjp1 ;
   /* RR=Cabs(R) ;
   RR=RR*RR ;
   printf("rp=%lf, ip=%lf, refl=%lf\n",dedens[j],dedens[j-1],RR);
   printf("fr=%lf,fi=%lf,phaser=%lf,phasei=%lf\n\n",reff.r,reff.i,phase.r,phase.i);*/
    }
```

```
  RR=Cabs(R) ;
  RR=RR*RR ;
  if(qz==0.0) RR=norm ;

  if(TYPE==1)  return(RR/norm) ;
  if(TYPE==2)  return(RR) ;
}


/*
 * model() returns the value of the model equation at the current
 * point using the current parameters.  If `deriv_flag' is nonzero,
 * model() must also calculate the analytic derivative of the model
 * equation with respect to each parameter that has the `fpar[i].p_fit'
 * flag set.
 */

double  model(deriv_flag)
int    deriv_flag;
 {   int totlay,j,k,dj ;
     double yfit  ;
     while(putindex==1)
       {setup();
        putindex=0;}
   if(cov==0)
     {edens[1]=rhotail ;
      dlay[1]=tail ;
      pz[0]=0.0 ;
      pz[1]=-tail ;
      pz[2]=-(tail+head) ;
      edens[2]=rhohead ;
      dlay[2]=head ;
      totlay=2 ;
       }
    else
      {
      if(pp<=0.0&&pp>(-tail))
        totlay=ed1(slicepro,pz,epro,eprobuf,dlay,edens) ;
      else  if(pp<=(-tail)&&pp>-(tail+head))
        totlay=ed2(slicepro,pz,epro,eprobuf,dlay,edens) ;
      else
        totlay=ed3(slicepro,pz,epro,eprobuf,dlay,edens) ;
       }

 edens[0]=topphase;
 dlay[0]=0.0 ;

 edens[totlay+1]=botphase;
 dlay[totlay+1]=0.0 ;

 for(j=1;j<=totlay;j++)
  dlay[j]=pz[j-1]-pz[j] ;

/*for(j=1;j<=totlay;j++)
  printf("%d , %f ,%f,%f\n",j,dlay[j],pz[j],edens[j]) ;*/
```

```
if(TYPE==0)
  {yfit=eshape(totlay,X,pz,edens) ; return(yfit) ;}

else
  { dj=deshape(totlay,pz,edens,ddlay,dedens) ;
    ddlay[0]=0.0 ;
    ddlay[dj+1]=0.0 ;
    yfit=parratt(X,dj,dedens,ddlay) ;return(yfit);}

}


int    prefilter(), postfilter();
int CreateCmdFile();
int ReadCh();
char swapPage=0;

struct  user_cmds {
        char    c_one;          /* The first letter of the command */
        char    c_two;          /* The second letter (or 0) */
        int     (*c_func)();     /* The name of the function */
} user_cmds[] = {
        { 'p', 'o', postfilter },
        { 'p', 'r', prefilter },
     {'e', '1', CreateCmdFile},
      {'e', '2', ReadCh},
        0,                      /* must be terminated with a zero */
};
prefilter() {
/**
*      (Here is how to loop through all the data)
*      register int   i;
*      register struct f_data    *d;
*
*      for (d = f_data, i = 0; i < npts; i++, INC(d)) {
*          d->d_xx[0] =    (independent variable)
*          d->d_xx[1] =    (optional 2nd independent variable)
*          d->d_xx[2] =    (and etc.)
*          d->d_y   =      (dependent variable)
*          d->d_w2  =      (square of weight for this point)
*      }
**/
}
postfilter() {
}
```

Appendix E   POTENTIAL CALCULATION FOR MD SIMULATION AND

PYTHON PROGRAM

In our simulation, z is the direction perpendicular to the membrane, therefore electrostatic potential in z direction across the simulation system is calculated with Poisson's equation as follow:

$$\frac{d^2\phi}{dz^2} = -\frac{1}{\epsilon_0}\sum_i q_i\rho_i(z) \tag{1}$$

were ϕ is the potential, ϵ_0 is vacuum diametric constant, q_i is the charge of atom i, $\rho_i(z)$ is the density of atoms of type i, $\sum_i q_i\rho_i(z)$ is the charge density. From Eq.(1) , the potential profile of the system can be derived by being integrated twice:

$$\phi(z) = -\frac{1}{\epsilon_0}\sum_i q_i \int_0^z \int_0^s \rho_i(u)du\,ds + C_1 z + C_2 \tag{2}$$

were C_1 and C_2 are constants of integration, and related to the boundary conditions. Eq.(2) can be transferred by switching the integration orders:

$$\phi(z) = -\frac{1}{\epsilon_0}\sum_i q_i \int_0^z (z - s)\rho_i(s)ds + C_1 z + C_2 \tag{3}$$

By slicing the system into slabs and summing up all the charges in the slabs, we can calculate the charge density term $\sum_i q_i\rho_i(z)$. C_1 and C_2 can be solved from boundary conditions shown below, and then the potential profile along the z direction can be derived from Eq.(3) by controlling the boundary conditions.

1.   Without External Electric Field ($\phi(0) = \phi(L) = 0$)

After applying the boundary condition $\phi(0) = \phi(L) = 0$ to Eq.(4), we can derived two equations as follow:

$$\phi(0) = C_2 = 0 \tag{4}$$

$$\phi(L) = \frac{1}{\epsilon_0}\sum_i q_i \int_0^L s\rho_i(s)ds - \frac{1}{\epsilon_0}\sum_i q_i \int_0^L L\rho_i(s)ds + C_1 L = 0 \tag{5}$$

where L is the length of the system. Because the system is neutral, $\sum_i q_i \int_0^L L\rho_i(s)ds$=0. From Eq.(6), we can solve $C_1 = -\frac{1}{\epsilon_0 L}\sum_i q_i \int_0^L s\rho_i(s)ds$. Therefore the potential profile of the system can be described by Eq.(4)

$$\phi(z) = \frac{1}{\epsilon_0}\sum_i q_i \int_0^z s\rho_i(s)ds - \frac{z}{\epsilon_0 L}\sum_i q_i \int_0^L s\rho_i(s)ds \tag{6}$$

2. With External Electric Field E ($\phi(0) = 0, \phi(L) = LE$)

     J. Gumbart *et al.*[126]describes the relationship of applied potential and reaction potential of the ionic system and it shows reaction potential of the ionic system is periodic, and the assumption $\phi(L) = LE$ is reasonable. E is the external electric field intensity applied through the system. Therefore, as shown before, two equations can be derived from Eq.(4) under boundary condition:

$$\phi(0) = C_2 = 0 \tag{8}$$

$$\phi(L) = \frac{1}{\epsilon_0} \sum_i q_i \int_0^L s\rho_i(s)ds + C_1 L = LE \tag{9}$$

From Eq. (8), $C_1 = E - \frac{1}{\epsilon_0} \sum_i q_i \int_0^L s\rho_i(s)ds$, and the potential profile of the system can be described by Eq.(4)

$$\phi(z) = \frac{1}{\epsilon_0} \sum_i q_i \int_0^z s\rho_i(s)ds - \frac{z}{\epsilon_0 L} \sum_i q_i \int_0^L s\rho_i(s)ds + Ez \tag{10}$$

```python
import pylab as pl
import numpy as np

data=np.loadtxt('E:\\research\\fitting\\lipid fitting\\from irena\\12162013\\elec_rho_ions.txt')
#data=np.loadtxt('E:/research/program/potential/interface_elec_rho2.txt')
#data2=np.loadtxt('E:/research/program/potential/wrap_E_V2.txt')
#pl.plot(data2[:,0],data2[:,1]*180.9)
#print data[:,-1]
#pl.plot(data[:,0],data[:,-1])
sum=np.sum(data[:,-1]*(data[1,0]-data[0,0]))
print sum
num=len(data)
off1=num/2+5/(data[1,0]-data[0,0])
off2=num/2-5/(data[1,0]-data[0,0])
center=np.average(data[:,0])
print center

#print Ed
#print sum

#dipole

L=data[-1,0]-data[0,0]
print L
#Unit of E (V/A)
externalE=0
print np.sum(data[:,-1]*(data[:,0]-data[0,0])*(data[1,0]-data[0,0]))
P=np.sum(data[:,-1]*(data[:,0]-data[0,0])*(data[1,0]-data[0,0]))*180.9/L-(sum)*180.9-externalE
polar=(data[:,0]-data[0,0])*P
#print P
#E

E=np.cumsum(data[:,-1]*(data[1,0]-data[0,0])*180.9)

#V
V=np.cumsum(E*(data[1,0]-data[0,0]))
Vf=-V-polar
pl.plot(data[:,0]-center,Vf)
np.savetxt('E:\\research\\fitting\\lipid fitting\\from irena\\12162013\\noelec.txt',np.vstack((data[:,0]-center,Vf)).transpose(),fmt='%0.3f\t%0.3e')

pl.show()
```

Appendix F   PROGRAM FOR REFLECTIVITY CALCULATION FROM

SIMULATION ELECTRON DENSITY

```python
import pylab as pl
import numpy as np

path='E:/research/fitting/lipid fitting/from irena/03142013/data/modified/'
#path1='E:/research/fitting/lipid fitting/from irena/03142013/data/modified/'
fname='sopc_elec00_rho115ns_moved'
#fname2='elec58_rho130ns'
ext='.txt'

data=np.loadtxt(path+fname+ext)
#data1=np.loadtxt(path1+fname2+ext)
#rx=data1[:,0]
#ry=data1[:,1]
#offset=0
#rx=rx+offset
start=60
end=115
o=data[:,0]
p=data[:,1]
L=len(o)
slab_thickness=(o[-1]-o[1])/L
print slab_thickness
x=[]
y=[]

roughness=7.6
#slab_thickness=0.02

z=len(data)
j=0
for i in range(0,z):
    if o[i]>start and o[i]<end:
        x.append(o[i])
        y.append(p[i])
f=pl.figure()
f.add_subplot(211)
pl.plot(x,y)
#f.add_subplot(211)
#pl.plot(o,p)

x1=np.arange(start-60,start,slab_thickness)
x2=np.arange(end,end+60,slab_thickness)
data1=np.ones_like(x1)*0.37
data2=np.ones_like(x2)*0.34
x=np.hstack((x1,x,x2)).flatten()
y=np.hstack((data1,y,data2)).flatten()
```

```
x1=np.arange(-3*roughness,3*roughness,slab_thickness)
rough_fun=np.exp(-x1**2/2/roughness**2)/np.sqrt(2.0*np.pi)/roughness

norm=np.sum(rough_fun)
conv_data=np.convolve(y,rough_fun,mode='same')/norm
np.savetxt(path+'ele00_11102013.txt',np.vstack((x,conv_data)).transpose(),fmt='%0.3f\t%0.3e')
f.add_subplot(212)
pl.plot(x,conv_data,'g-',x,y,'r-')
#pl.plot(x,conv_data,'g-',x,y,'r-',rx,ry,'b-')
pl.show()
```

VITA

Hao Yu

<u>Education</u>

B.S., Material Physics, 2005, University of Science and Technology of China, China
M.S., Physics, 2008, University of Illinois at Chicago
M.S., Mathematics, 2009, University of Illinois at Chicago

<u>Experience</u>

Research Assistant, Physics Department, University of Illinois at Chicago, 2007 to present
Teaching Assistant, Physics Department, University of Illinois at Chicago, 2005 to present

<u>Membership</u>

Biological Society, 2011

<u>Publication</u>

Laanait, N.; Mihaylov, M.; Hou, B.; Yu, H.; Vanysek, P.; Meron, M.; Lin, B.; Benjamin, I.; Schlossman, M. L., Tuning Ion correlations at an electrified soft interface *Proceedings of the National Academy of Sciences (USA)* **2012**, *109*, 20326.

Hou, B.; Laanait, N.; Yu, H.; Bu, W.; Yoon, J.; Lin, B.; Meron, M.; Luo, G.; Vanysek, P.; Schlossman, M. L., Ion Distributions at the Water/1,2-Dichloroethane Interface: Potential of Mean Force Approach to Analyzing X-ray Reflectivity and Interfacial Tension Measurements *Journal of Physical Chemistry B* **2013**, *117*, 5365

Hao Yu, Irena Yzeiri, Binyang Hou, Chiu-Hao Chen, Wei Bu, Petr Vanysek, Yu-Sheng Chen, Binhua Lin, Petr Král, and Mark L. Schlossman, Ordering of SOPC lipid monolayers at an electrified 1,2-dichloroethane/water interface, *Manustript in Prepareation,* 2013

Hao Yu, Zenmei Ohkubo, Chiuhao Chen, Shan Tao, Wei Bu, Binyang Hou, Mrinal Bera, Sabina Tatur, Binhua Lin, Mati Meron, Wonhua Cho, Emad Tajkhorshid, Mark Schlossman，Modulation of Protein-Lipid Binding by Electric Fields，*Manustript in Prepareation,* 2013

Bu, W.; Yu, H.; Luo, G.; Bera, M. K.; Hou, B.; Lin, B.; Meron, M.; Kuzmenko, I.; Soderholm, L.; Antonio, M.; Schlossman, M. L., Intermediate state in extractant-mediated transport of ions across oil/water interfaces, *Manustript in Prepareation,* 2013.

Bera, M. K.; Tatur, S.; Yu, H.; Bu, W.; Amoanu, D.; Moyano, D. F.; Rotello, V. M.; Lin, B.; Meron, M.; Vanysek, P.; Schlossman, M. L., Electric field driven transition in a monolayer of charged nanoparticles at a liquid/liquid interface, *Manustript in Prepareation,* 2013

American Chemical Society's Policy on Theses and Dissertations

If your university requires you to obtain permission, you must use the RightsLink permission system. See RightsLink instructions at http://pubs.acs.org/page/copyright/permissions.html.

This is regarding request for permission to include your paper(s) or portions of text from your paper(s) in your thesis. Permission is now automatically granted; please pay special attention to the implications paragraph below. The Copyright Subcommittee of the Joint Board/Council Committees on Publications approved the following:

Copyright permission for published and submitted material from theses and dissertations

ACS extends blanket permission to students to include in their theses and dissertations their own articles, or portions thereof, that have been published in ACS journals or submitted to ACS journals for publication, provided that the ACS copyright credit line is noted on the appropriate page(s).

Publishing implications of electronic publication of theses and dissertation material

Students and their mentors should be aware that posting of theses and dissertation material on the Web prior to submission of material from that thesis or dissertation to an ACS journal may affect publication in that journal. Whether Web posting is considered prior publication may be evaluated on a case-by-case basis by the journal's editor. If an ACS journal editor considers Web posting to be "prior publication", the paper will not be accepted for publication in that journal. If you intend to submit your unpublished paper to ACS for publication, check with the appropriate editor prior to posting your manuscript electronically.

Reuse/Republication of the Entire Work in Theses or Collections: Authors may reuse all or part of the Submitted, Accepted or Published Work in a thesis or dissertation that the author writes and is required to submit to satisfy the criteria of degree-granting institutions. Such reuse is permitted subject to the ACS' "Ethical Guidelines to Publication of Chemical Research" (http://pubs.acs.org/page/policy/ethics/index.html); the author should secure written confirmation (via letter or email) from the respective ACS journal editor(s) to avoid potential conflicts with journal prior publication*/embargo policies. Appropriate citation of the Published Work must be made. If the thesis or dissertation to be published is in electronic format, a direct link to the Published Work must also be included using the ACS Articles on Request author-directed link . see http://pubs.acs.org/page/policy/articlesonrequest/index.html

* Prior publication policies of ACS journals are posted on the ACS website at

http://pubs.acs.org/page/policy/prior/index.html

If your paper has not yet been published by ACS, please print the following credit line on the first page of your article: "Reproduced (or 'Reproduced in part') with permission from [JOURNAL NAME], in press (or 'submitted for publication'). Unpublished work copyright [CURRENT YEAR] American Chemical Society." Include appropriate information.

If your paper has already been published by ACS and you want to include the text or portions of the text in your thesis/dissertation, please print the ACS copyright credit line on the first page of your article: "Reproduced (or 'Reproduced in part') with permission from [FULL REFERENCE CITATION.] Copyright [YEAR] American Chemical Society." Include appropriate information.

Submission to a Dissertation Distributor: If you plan to submit your thesis to UMI or to another dissertation distributor, you should not include the unpublished ACS paper in your thesis if the thesis will be disseminated electronically, until ACS has published your paper. After publication of the paper by ACS, you may release the entire thesis (not the individual ACS article by itself) for electronic dissemination through the distributor; ACS's copyright credit line should be printed on the first page of the ACS paper.

CITED LITERATURE

(1)   Verkleij, A. J.; Post, J. A. Membrane phospholipid asymmetry and signal transduction. <u>J Membr Biol</u> **2000**, *178*, 1.

(2)   Daleke, D. L.; Huestis, W. H. Erythrocyte morphology reflects the transbilayer distribution of incorporated phospholipids. <u>J Cell Biol</u> **1989**, *108*, 1375.

(3)   Zwaal, R. F.; Schroit, A. J. Pathophysiologic implications of membrane phospholipid asymmetry in blood cells. <u>Blood</u> **1997**, *89*, 1121.

(4)   Henson, P. M.; Bratton, D. L.; Fadok, V. A. Apoptotic cell removal. <u>Curr Biol</u> **2001**, *11*, R795.

(5)   Mashaghi, A.; Partovi-Azar, P.; Jadidi, T.; Nafari, N.; Maass, P.; Tabar, M. R.; Bonn, M.; Bakker, H. J. Hydration strongly affects the molecular and electronic structure of membrane phospholipids. <u>Journal of Chemical Physics</u> **2012**, *136*, 114709.

(6)   Tieleman, D. P. The molecular basis of electroporation. <u>BMC Biochem</u> **2004**, *5*, 10.

(7)   Tieleman, D. P.; Leontiadou, H.; Mark, A. E.; Marrink, S. J. Simulation of pore formation in lipid bilayers by mechanical stress and electric fields. <u>Journal of the American Chemical Society</u> **2003**, *125*, 6382.

(8)   Malkova, S. <u>X-ray Reflectivity Studies of CPLA$_2$-C2 Domains Adsorbed onto Langmuir Monolayers of SOPC</u>, University of Illinois at Chicago, 2005.

(9)   Brändén, C.-I.; Tooze, J. <u>Introduction to protein structure</u>, 2nd ed.; Garland Pub.: New York, 1999.

(10)   Nalefski, E. A.; Wisner, M. A.; Chen, J. Z.; Sprang, S. R.; Fukuda, M.; Mikoshiba, K.; Falke, J. J. C2 domains from different Ca2+ signaling pathways display functional and mechanistic diversity. <u>Biochemistry</u> **2001**, *40*, 3089.

(11)   Murray, D.; Honig, B. Electrostatic control of the membrane targeting of C2 domains. <u>Mol Cell</u> **2002**, *9*, 145.

(12)   Chen, C. H.; Malkova, S.; Pingali, S. V.; Long, F.; Garde, S.; Cho, W.; Schlossman, M. L. Configuration of PKCalpha-C2 domain bound to mixed SOPC/SOPS lipid monolayers. <u>Biophys J</u> **2009**, *97*, 2794.

(13)   Bittova, L.; Sumandea, M.; Cho, W. A structure-function study of the C2 domain of cytosolic phospholipase A2. Identification of essential calcium ligands and hydrophobic membrane binding residues. <u>J Biol Chem</u> **1999**, *274*, 9665.

(14)   Malkova, S.; Long, F.; Stahelin, R. V.; Pingali, S. V.; Murray, D.; Cho, W.; Schlossman, M. L. X-ray reflectivity studies of cPLA$_2$a-C2 domains adsorbed onto Langmuir monolayers of SOPC. <u>Biophys. J.</u> **2005**, *89*, 1861.

(15)   Marecek, V.; Lhotsky, A.; Janchenova, H. Mechanism of lecithin adsorption at a liquid vertical bar liquid interface. <u>Journal of Physical Chemistry B</u> **2003**, *107*, 4573.

(16)   Girault, H. H.; Schiffrin, D. J. Charge effects on phospholipid monolayers in relation to cell motility. Biochim Biophys Acta **1986**, *857*, 251.

(17)   Samec, Z.; Trojanek, A.; Krtil, P. Dynamics of phospholipid monolayers on polarised liquid-liquid interfaces. Faraday Discus. **2005**, *129*, 301.

(18)   Franklin, B.; Bigelow, J.; Hall, H. B.; Benjamin Franklin Collection (Library of Congress) The complete works of Benjamin Franklin : including his private as well as his official and scientific correspondence, and numerous letters and documents now for the first time printed, with many others not included in any former collection : also the unmutilated and correct version of his autobiography; G.P. Putnam's Sons: New York ; London, 1887.

(19)   Gibbs, J. W. The collected works of J. Willard Gibbs; Yale Univ. Press: New Haven,, 1948.

(20)   Blank, M.; Feig, S. Electric Fields across Water-Nitrobenzene Interfaces. Science **1963**, *141*, 1173.

(21)   Koryta, J.; Vanysek, P.; Brezina, M. Electrolysis with an Electrolyte Dropping Electrode. Journal of Electroanalytical Chemistry **1976**, *67*, 263.

(22)   Matsumura, H.; Furusawa, K. Electrical phenomena at the surface of phospholipid membranes relevant to the sorption of ionic compounds. Adv Colloid Interface Sci **1989**, *30*, 71.

(23)   Watanabe, A.; Matsumoto, M.; Tamai, H.; Gotoh, R. Electrocapillary phenomena at oil-water interfaces. Kolloid-Zeitschrift und Zeitschrift für Polymere **1968**, *228*, 58.

(24)   Watanabe, A.; Fujii, A.; Sakamori, Y.; Higashitsuji, K.; Tamai, M. H. Studies on the behaviour of phospholipids at oil-water interfaces. Kolloid-Zeitschrift und Zeitschrift für Polymere **1971**, *243*, 42.

(25)   Kakiuchi, T.; Yamane, M.; Osakai, T.; Senda, M. Monolayer formation of dilauroylphosphatidylcholine at the polarized nitrobenzene-water interface. Bull. Chem. Soc. Jpn **1987**, *60*, 4223.

(26)   Friedrich, W.; Knipping, P.; Laue, M. Interferenzerscheinungen bei Röntgenstrahlen. Annalen der Physik **1913**, *346*, 971.

(27)   Als-Nielsen, J.; Kjaer, K. X-ray reflectivity and diffraction studies of liquid surfaces and surfactant monolayers. In *Phase Transitions in Soft Condensed Matter*; Riste, T., Sherrington, D., Eds.; Plenum Press, 1989; Vol. 211; pp 145.

(28)   Parratt, L. G. Surface studies of solids by total reflection of x-rays. Phys. Rev. **1954**, *95*, 359.

(29)   Pershan, P. S.; Schlossman, M. L. Liquid Surfaces and Interfaces: Synchrotron X-ray Methods; Cambridge University Press: Cambridge, 2012.

(30)   Bu, W. Ion distributions at charged aqueous surfaces: Synchrotron X-ray scattering studies, Iowa State University, 2009.

(31)   *X-Ray Scattering from Soft-Matter Thin Films: Materials Science and Basic Research*; Tolan., M., Ed.; Springer, 1999.

(32)   Fisk, S.; Widom, B. Structure and free energy of the interface between fluid phases in equilibrium near the critical point. The Journal of Chemical Physics **1969**, *50*, 3219.

(33)   Buff, F.; Lovett, R.; Stillinger Jr, F. Interfacial density profile for fluids in the critical region. Physical Review Letters **1965**, *15*, 621.

(34)   Fisher, M. P.; Fisher, D. S.; Weeks, J. D. Agreement of capillary-wave theory with exact results for the interface profile of the two-dimensional Ising model. Physical Review Letters **1982**, *48*, 368.

(35)   Lippe, G.; Sorgato, M. C.; Harris, D. A. The binding and release of the inhibitor protein are governed independently by ATP and membrane potential in ox-heart submitochondrial vesicles. Biochim Biophys Acta **1988**, *933*, 12.

(36)   Dimroth, P.; Kaim, G.; Matthey, U. Crucial role of the membrane potential for ATP synthesis by F1Fo ATP synthases. Journal of Experimental Biology **2000**, *203*, 51.

(37)   Armstrong, C. M.; Hille, B. Voltage-gated ion channels and electrical excitability. Neuron **1998**, *20*, 371.

(38)   Radhakrishnan, A.; McConnell, H. M. Electric field effect on cholesterol-phospholipid complexes. Proc Natl Acad Sci U S A **2000**, *97*, 1073.

(39)   Neumann, E.; Rosenheck, K. Permeability changes induced by electric impulses in vesicular membranes. J Membr Biol **1972**, *10*, 279.

(40)   Kinosita, K., Jr.; Tsong, T. Y. Formation and resealing of pores of controlled sizes in human erythrocyte membrane. Nature **1977**, *268*, 438.

(41)   Maeda, K.; Yoshida, Y.; Goto, T.; Marecek, V. Blocking effect of a phospholipid monolayer on ion transfer at a liquid/liquid interface and its electrochemical control. J. Electroanal. Chem. **2004**, *567*, 317.

(42)   Nagatani, H.; Samec, Z.; Brevet, P.-F.; Fermin, D. J.; Girault, H. H. Adsorption and Aggregation of meso-Tetrakis(4-carboxyphenyl)porphyrinato Zinc(II) at the Polarized Water|1,2-Dichloroethane Interface. J. Phys. Chem. B **2003**, *107*, 786.

(43)   Trojanek, A.; Lhotsky, A.; Marecek, V.; Samec, Z. Limited agreement between the interfacial tension and differential capacity data for the polarised water | 1,2-dichloroethane interface. Journal of Electroanalytical Chemistry **2004**, *565*, 243.

(44)   Samec, Z.; Trojanek, A.; Girault, H. H. Thermodynamic analysis of the cation binding to a phosphatidylcholine monolayer at a polarised interface between two immiscible electrolyte solutions. Electrochem. Comm. **2003**, *5*, 98.

(45)   Roux, B. Influence of the membrane potential on the free energy of an intrinsic protein. Biophys J **1997**, *73*, 2980.

(46)   Tarek, M. Membrane electroporation: a molecular dynamics simulation. Biophys J **2005**, *88*, 4045.

(47)   Zhang, Z.; Mitrinovic, D. M.; Williams, S. M.; Huang, Z.; Schlossman, M. L. X-ray Scattering from Monolayers of $F(CF_2)_{10}(CH_2)_2OH$ at the Water-(Hexane Solution) and Water-Vapor Interfaces. J. Chem. Phys. **1999**, *110*, 7421.

(48)   Small, D. M. Potpourri: effects of unsaturation on lipid structure; plasma cholesterol ester and lipid-transfer proteins; and cholesterol-sensing proteins and cellular cholesterol movement. Curr Opin Struct Biol **1998**, *8*, 413.

(49)   Schroeder, R.; London, E.; Brown, D. Interactions between saturated acyl chains confer detergent resistance on lipids and glycosylphosphatidylinositol (GPI)-anchored proteins: GPI-anchored proteins in liposomes and cells show similar behavior. Proc Natl Acad Sci U S A **1994**, *91*, 12130.

(50)   Megha; Sawatzki, P.; Kolter, T.; Bittman, R.; London, E. Effect of ceramide N-acyl chain and polar headgroup structure on the properties of ordered lipid domains (lipid rafts). Biochim Biophys Acta **2007**, *1768*, 2205.

(51)   Nagle, J. F.; Tristram-Nagle, S. Structure of lipid bilayers. Biochim Biophys Acta **2000**, *1469*, 159.

(52)   Hou, B.; Laanait, N.; Yu, H.; Bu, W.; Yoon, J.; Lin, B.; Meron, M.; Luo, G.; Vanysek, P.; Schlossman, M. L. Ion Distributions at the Water/1,2-Dichloroethane Interface: Potential of Mean Force Approach to Analyzing X-ray Reflectivity and Interfacial Tension Measurements. Journal of Physical Chemistry B **2013**, *117*, 5365.

(53)   Grahame, D. C. The Electrical Double Layer and the Theory of Electrocapillarity. Chemical Reviews **1947**, *41*, 441.

(54)   Samec, Z. Electrical double layer at the interface between two immiscible electrolyte solutions. Chem. Rev. **1988**, *88*, 617.

(55)   Laanait, N.; Yoon, J.; Hou, B.; Vanysek, P.; Meron, M.; Lin, B.; Luo, G.; Benjamin, I.; Schlossman, M. L. Monovalent ion condensation at the electrified liquid/liquid interface. J. Chem. Phys. **2010**, *132*, 171101.

(56)   Laanait, N.; Mihaylov, M.; Hou, B.; Yu, H.; Vanysek, P.; Meron, M.; Lin, B.; Benjamin, I.; Schlossman, M. L. Ion distributions at the electrified liquid/liquid interface II: Ion correlations, 2012.

(57)   Hard, S.; Hamnerius, Y.; Nilsson, O. Laser heterodyne apparatus for measurements of liquid surface properties - Theory and experiments. Journal of Applied Physics **1976**, *47*, 2433.

(58)   McQueen, D.; Lundström, I. Light scattering study of capillary waves on water covered by monomolecular films. J. Chem. Soc., Faraday Trans. 1 **1973**, *69*, 694.

(59)   Katyl, R. H.; Ingard, U. Scattering of light by thermal ripplons. Physical Review Letters **1968**, *20*, 248.

(60)   Langevin, D. Light-Scattering from Free-Surface of Water. Journal of the Chemical Society-Faraday Transactions I **1974**, *70*, 95.

(61)   Byrne, D.; Earnshaw, J. C. Photon Correlation Spectroscopy of Liquid Surfaces - Effect of Instrumental Broadening. Journal of Physics D-Applied Physics **1977**, *10*, L207.

(62)   Takahashi, S.; Harata, A.; Kitamori, T.; Suwada, T. Quasi-Elastic Laser Scattering Method for Monitoring Capillary Wave Frequency at a Water Nitrobenzene Interface. Analytical Sciences **1994**, *10*, 305.

(63)   Lofgren, H.; Neuman, R. D.; Scriven, L. E.; Davis, H. T. Laser Light-Scattering Measurements of Interfacial-Tension Using Optical Heterodyne Mixing Spectroscopy. Journal of Colloid and Interface Science **1984**, *98*, 175.

(64)   Takahashi, S.; Tsuyumoto, I.; Kitamori, T.; Sawada, T. Monitoring of molecular behavior of a chemical oscillation system at a liquid/liquid interface using a time-resolved quasi-elastic laser scattering method. Electrochimica Acta **1998**, *44*, 165.

(65)   Langevin, D. Light Scattering by Liquid Surfaces and Complementary Techniques; Marcel Dekker Inc.: New York, 1992.

(66)   Lamb, H. On waves in an elastic plate. Proceedings of the Royal Society of London. Series A **1917**, *93*, 114.

(67)   Agranovich, V. M.; Loudon, R. Surface excitations; North-Holland: Amsterdam ; New York, 1984.

(68)   Trojanek, A.; Krtil, P.; Samec, Z. Quasi-elastic laser light scattering from thermally excited capillary waves on polarised liquid vertical bar liquid interfaces Part 1: effects of adsorption of hexadecyltrimethylammonium chloride at the water vertical bar 1,2-dichloroethane interface. Journal of Electroanalytical Chemistry **2001**, *517*, 77.

(69)   Pecora, R. Doppler shifts in light scattering from pure liquids and polymer solutions. The Journal of Chemical Physics **1964**, *40*, 1604.

(70)   Compton, R., Banks, E. C. Understanding Voltammetry, 2nd ed.; World Scientific, 2010.

(71)   Hou, B. Ion distributions at electrified liquid-liquid interfaces: Microscopic and macroscopic measurements. Ph.D. Thesis, University of Illlinois at Chicago, 2011.

(72)   Phillips, J. C.; Braun, R.; Wang, W.; Gumbart, J.; Tajkhorshid, E.; Villa, E.; Chipot, C.; Skeel, R. D.; Kale, L.; Schulten, K. Scalable molecular dynamics with NAMD. Journal of Computational Chemistry **2005**, *26*, 1781.

(73)   Klauda, J. B.; Venable, R. M.; Freites, J. A.; O'Connor, J. W.; Tobias, D. J.; Mondragon-Ramirez, C.; Vorobyov, I.; MacKerell, A. D.; Pastor, R. W. Update of the CHARMM All-Atom Additive Force Field for Lipids: Validation on Six Lipid Types. Journal of Physical Chemistry B **2010**, *114*, 7830.

(74)   Servantie, J.; Gaspard, P. Methods of calculation of a friction coefficient: Application to nanotubes. Physical Review Letters **2003**, *91*.

(75)   Feller, S. E.; Zhang, Y. H.; Pastor, R. W. Computer-Simulation of Liquid/Liquid Interfaces .2. Surface-Tension Area Dependence of a Bilayer and Monolayer. Journal of Chemical Physics **1995**, *103*, 10267.

(76)   Humphrey, W.; Dalke, A.; Schulten, K. VMD: Visual molecular dynamics. Journal of Molecular Graphics & Modelling **1996**, *14*, 33.

(77)   Darden, T.; York, D.; Pedersen, L. Particle Mesh Ewald - an N.Log(N) Method for Ewald Sums in Large Systems. Journal of Chemical Physics **1993**, *98*, 10089.

(78)   Samec, Z. Electrochemistry at the interface between two immiscible electrolyte solutions. Pure Appl. Chem. **2004**, *76*, 2147.

(79)   Yoshida, Y.; Maeda, K.; Shirai, O. The complex formation of ions with a phospholipid monolayer adsorbed at an aqueous vertical bar 1,2-dichloroethane interface. Journal of Electroanalytical Chemistry **2005**, *578*, 17.

(80)   Lewis, B. A.; Engelman, D. M. Lipid bilayer thickness varies linearly with acyl chain length in fluid phosphatidylcholine vesicles. J Mol Biol **1983**, *166*, 211.

(81)   Luo, G.; Malkova, S.; Yoon, J.; Schultz, D. G.; Lin, B.; Meron, M.; Benjamin, I.; Vanysek, P.; Schlossman, M. L. Ion distributions near a liquid-liquid interface. Science **2006**, *311*, 216.

(82)   Marcus, Y. Ionic radii in aqueous solutions. Chem. Rev. **1988**, *88*, 1475.

(83)   Frisch, M. J. T., G. W.; Schlegel, H. B.; Scuseria, G. E.; Robb, M. A.; Cheeseman, J. R.; Montgomery, Jr., J. A.; Vreven, T.; Kudin, K. N.; Burant, J. C.; Millam, J. M.; Iyengar, S. S.; Tomasi, J.; Barone, V.; Mennucci, B.; Cossi, M.; Scalmani, G.; Rega, N.; Petersson, G. A.; Nakatsuji, H.; Hada, M.; Ehara, M.; Toyota, K.; Fukuda, R.; Hasegawa, J.; Ishida, M.; Nakajima, T.; Honda, Y.; Kitao, O.; Nakai, H.; Klene, M.; Li, X.; Knox, J. E.; Hratchian, H. P.; Cross, J. B.; Bakken, V.; Adamo, C.; Jaramillo, J.; Gomperts, R.; Stratmann, R. E.; Yazyev, O.; Austin, A. J.; Cammi, R.; Pomelli, C.; Ochterski, J. W.; Ayala, P. Y.; Morokuma, K.; Voth, G. A.; Salvador, P.; Dannenberg, J. J.; Zakrzewski, V. G.; Dapprich, S.; Daniels, A. D.; Strain, M. C.; Farkas, O.; Malick, D. K.; Rabuck, A. D.; Raghavachari, K.; Foresman, J. B.; Ortiz, J. V.; Cui, Q.; Baboul, A. G.; Clifford, S.; Cioslowski, J.; Stefanov, B. B.; Liu, G.; Liashenko, A.; Piskorz, P.; Komaromi, I.; Martin, R. L.; Fox, D. J.; Keith, T.; Al-Laham, M. A.; Peng, C. Y.; Nanayakkara, A.; Challacombe, M.; Gill, P. M. W.; Johnson, B.; Chen, W.; Wong, M. W.; Gonzalez, C.; and Pople, J. A.; Gaussian 03, Revision C.02 ed.; Gaussian, Inc., 2004.

(84)   Small, D. M. Phase equilibria and structure of dry and hydrated egg lecithin. J Lipid Res **1967**, *8*, 551.

(85)   Armen, R. S.; Uitto, O. D.; Feller, S. E. Phospholipid component volumes: determination and application to bilayer structure calculations. Biophys J **1998**, *75*, 734.

(86)   Gurtovenko, A. A.; Vattulainen, I. Calculation of the electrostatic potential of lipid bilayers from molecular dynamics simulations: Methodological issues. Journal of Chemical Physics **2009**, *130*.

(87)   Vermeer, L. S.; de Groot, B. L.; Reat, V.; Milon, A.; Czaplicki, J. Acyl chain order parameter profiles in phospholipid bilayers: computation from molecular dynamics simulations and comparison with 2H NMR experiments. Eur Biophys J **2007**, *36*, 919.

(88)   Small, D. M. The Physical Chemistry of Lipids; Plenum: New York, 1986.

(89)   Israelachvili, J. N. Intermolecular and surface forces : with applications to colloidal and biological systems; Academic Press: London ; Orlando, Fla . 1985.

(90)   Thoma, M.; Schwendler, M.; Baltes, H.; Helm, C. A.; Pfohl, T.; Riegler, H.; Mohwald, H. Ellipsometry and x-ray reflectivity studies on monolayers of phosphatidylethanolamine and phosphatidylcholine in contact with n-dodecane, n-hexadecane, and bicyclohexyl. Langmuir **1996**, *12*, 1722.

(91)   Sun, W.; Suter, R. M.; Knewtson, M. A.; Worthington, C. R.; Tristram-Nagle, S.; Zhang, R.; Nagle, J. F. Order and disorder in fully hydrated unoriented bilayers of gel-phase dipalmitoylphosphatidylcholine. Phys Rev E Stat Phys Plasmas Fluids Relat Interdiscip Topics **1994**, *49*, 4665.

(92)   Safran, S. A. Statistical Thermodynamics of Surfaces, Interfaces, and Membranes; Addison-Wesley Publishing Co.: Reading, MA, 1994.

(93)   Luo, G.; Malkova, S.; Yoon, J.; Schultz, D. G.; Lin, B.; Meron, M.; Benjamin, I.; Vanysek, P.; Schlossman, M. L. Ion distributions at the nitrobenzene-water interface electrified by a common ion. J. Electroanal. Chem. **2006**, *593*, 142.

(94)   Daillant, J.; Bosio, L.; Benattar, J. J.; Meunier, J. Capillary Waves and Bending Elasticity of Monolayers on Water Studied by X-Ray Reflectivity as a Function of Surface Pressure. Europhysics Letters **1989**, *8*, 453.

(95)   Cho, W. Membrane targeting by C1 and C2 domains. J Biol Chem **2001**, *276*, 32407.

(96)   Cho, W.; Stahelin, R. V. Membrane-protein interactions in cell signaling and membrane trafficking. Annu Rev Biophys Biomol Struct **2005**, *34*, 119.

(97)   Coussens, L.; Parker, P. J.; Rhee, L.; Yang-Feng, T. L.; Chen, E.; Waterfield, M. D.; Francke, U.; Ullrich, A. Multiple, distinct forms of bovine and human protein kinase C suggest diversity in cellular signaling pathways. Science **1986**, *233*, 859.

(98)   Knopf, J. L.; Lee, M. H.; Sultzman, L. A.; Kriz, R. W.; Loomis, C. R.; Hewick, R. M.; Bell, R. M. Cloning and expression of multiple protein kinase C cDNAs. Cell **1986**, *46*, 491.

(99)   Nalefski, E. A.; Falke, J. J. The C2 domain calcium-binding motif: structural and functional diversity. Protein Sci **1996**, *5*, 2375.

(100)   Rotin, D.; Staub, O.; Haguenauer-Tsapis, R. Ubiquitination and endocytosis of plasma membrane proteins: role of Nedd4/Rsp5p family of ubiquitin-protein ligases. J Membr Biol **2000**, *176*, 1.

(101)   Lin, L. L.; Lin, A. Y.; Knopf, J. L. Cytosolic phospholipase A2 is coupled to hormonally regulated release of arachidonic acid. Proc Natl Acad Sci U S A **1992**, *89*, 6147.

(102)   Malmberg, N. J.; Buskirk, D. R. V.; Falke, J. J. Membrane-docking loops of the cPLA2 C2 domain: Detailed structural analysis of hte protein-membrane interface via site-directed spin-labeling. Biochem. **2003**, *42*, 13227.

(103)   Perisic, O.; Fong, S.; Lynch, D. E.; Bycroft, M.; Williams, R. L. Crystal structure of a calcium-phospholipid binding domain from cytosolic phospholipase A2. J Biol Chem **1998**, *273*, 1596.

(104)   Ball, A.; Nielsen, R.; Gelb, M. H.; Robinson, B. H. Interfacial membrane docking of cytosolic phospholipase A2 C2 domain using electrostatic potential-modulated spin relaxation magnetic resonance. Proc Natl Acad Sci U S A **1999**, *96*, 6637.

(105)   Malkova, S.; Stahelin, R. V.; Pingali, S. V.; Cho, W.; Schlossman, M. L. Orientation and penetration depth of monolayer-bound p40phox-PX. Biochemistry **2006**, *45*, 13566.

(106)   Rizo, J.; Sudhof, T. C. C2-domains, structure and function of a universal Ca2+-binding domain. J Biol Chem **1998**, *273*, 15879.

(107)   Shao, X.; Li, C.; Fernandez, I.; Zhang, X.; Sudhof, T. C.; Rizo, J. Synaptotagmin-syntaxin interaction: the C2 domain as a Ca2+-dependent electrostatic switch. Neuron **1997**, *18*, 133.

(108)   Davletov, B.; Perisic, O.; Williams, R. L. Calcium-dependent membrane penetration is a hallmark of the C2 domain of cytosolic phospholipase A2 whereas the C2A domain of synaptotagmin binds membranes electrostatically. J Biol Chem **1998**, *273*, 19093.

(109)   Brockman, H. Lipid monolayers: why use half a membrane to characterize protein-membrane interactions? Curr Opin Struct Biol **1999**, *9*, 438.

(110)   Wieloch, T.; Borgstrom, B.; Pieroni, G.; Pattus, F.; Verger, R. Product activation of pancreatic lipase. Lipolytic enzymes as probes for lipid/water interfaces. J Biol Chem **1982**, *257*, 11523.

(111)   Cunningham, B. A.; Tsujita, T.; Brockman, H. L. Enzymatic and physical characterization of diacylglycerol-phosphatidylcholine interactions in bilayers and monolayers. Biochemistry **1989**, *28*, 32.

(112)   Ananthanarayanan, B.; Das, S.; Rhee, S. G.; Murray, D.; Cho, W. Membrane targeting of C2 domains of phospholipase C-delta isoforms. J Biol Chem **2002**, *277*, 3568.

(113)   Stahelin, R. V.; Rafter, J. D.; Das, S.; Cho, W. The molecular basis of differential subcellular localization of C2 domains of protein kinase C-alpha and group IVa cytosolic phospholipase A2. J Biol Chem **2003**, *278*, 12452.

(114)   Xu, G. Y.; McDonagh, T.; Yu, H. A.; Nalefski, E. A.; Clark, J. D.; Cumming, D. A. Solution structure and membrane interactions of the C2 domain of cytosolic phospholipase A2. J Mol Biol **1998**, *280*, 485.

(115)   Frazier, A. A.; Wisner, M. A.; Malmberg, N. J.; Victor, K. G.; Fanucci, G. E.; Nalefski, E. A.; Falke, J. J.; Cafiso, D. S. Membrane orientation and position of the C2 domain from cPLA2 by site-directed spin labeling. Biochemistry **2002**, *41*, 6282.

(116)   Chen, C.-H.; Malkova, S.; Pingali, S. V.; Long, F.; Garde, S.; Cho, W.; Schlossman, M. Configuration of PKCα-C2 Domain Bound to Mixed SOPC/SOPS Lipid Monolayers. Biophysical Journal **2009**, *97*, 2794.

(117)   McIntosh, T. J.; Simon, S. A. Contributions of hydration and steric (entropic) pressures to the interactions between phosphatidylcholine bilayers: Experiments with the subgel phase. Biochemistry **1993**, *32*, 8374.

(118)   Phillips, J. C.; Braun, R.; Wang, W.; Gumbart, J.; Tajkhorshid, E.; Villa, E.; Chipot, C.; Skeel, R. D.; Kale, L.; Schulten, K. Scalable molecular dynamics with NAMD. J Comput Chem **2005**, *26*, 1781.

(119)   MacKerell, A. D.; Bashford, D.; Bellott, M.; Dunbrack, R. L.; Evanseck, J. D.; Field, M. J.; Fischer, S.; Gao, J.; Guo, H.; Ha, S.; Joseph-McCarthy, D.; Kuchnir, L.; Kuczera, K.; Lau, F. T. K.; Mattos, C.; Michnick, S.; Ngo, T.; Nguyen, D. T.; Prodhom, B.; Reiher, W. E.; Roux, B.; Schlenkrich, M.; Smith, J. C.; Stote, R.; Straub, J.; Watanabe, M.; Wiorkiewicz-Kuczera, J.; Yin, D.; Karplus, M. All-atom empirical potential for molecular modeling and dynamics studies of proteins. Journal of Physical Chemistry B **1998**, *102*, 3586.

(120)   Mackerell, A. D., Jr.; Feig, M.; Brooks, C. L., 3rd. Extending the treatment of backbone energetics in protein force fields: limitations of gas-phase quantum mechanics in reproducing protein conformational distributions in molecular dynamics simulations. Journal of Computational Chemistry **2004**, *25*, 1400.

(121)   Ohkubo, Y. Z.; Pogorelov, T. V.; Arcario, M. J.; Christensen, G. A.; Tajkhorshid, E. Accelerating membrane insertion of peripheral proteins with a novel membrane mimetic model. Biophys J **2012**, *102*, 2130.

(122)   Wijkander, J.; Sundler, R. Macrophage arachidonate-mobilizing phospholipase A2: role of Ca2+ for membrane binding but not for catalytic activity. Biochem Biophys Res Commun **1992**, *184*, 118.

(123)   Wijkander, J.; Sundler, R. Regulation of arachidonate-mobilizing phospholipase A2 by phosphorylation via protein kinase C in macrophages. FEBS Lett **1992**, *311*, 299.

(124)   Bu, W.; Yu, H.; Luo, G.; Bera, M. K.; Hou, B.; Lin, B.; Meron, M.; Kuzmenko, I.; Soderholm, L.; Antonio, M.; Schlossman, M. L. Intermediate state in extractant-mediated transport of ions across oil/water interfaces, 2013.

(125)   Murray, D.; Arbuzova, A.; Honig, B.; McLaughlin, S. The role of electrostatic and nonpolar interactions in the association of peripheral proteins with membranes. Curr. Top. Membr. **2002**, *52*, 277.

(126)   Gumbart, J.; Khalili-Araghi, F.; Sotomayor, M.; Roux, B. Constant electric field simulations of the membrane potential illustrated with simple systems. Biochim Biophys Acta **2012**, *1818*, 294.